2015

The mechanism governing cutting of hard materials with hybrid Laser/Waterjet system through controlled fracture

Zhuoru Wu
Iowa State University

The mechanism governing cutting of hard materials with hybrid Laser/Waterjet system through controlled fracture

by

Zhuoru Wu

A dissertation submitted to the graduate faculty

in partial fulfillment of the requirements for the degree of

DOCTOR OF PHILOSOPHY

Major: Mechanical Engineering

Program of Study Committee:
Pranav Shrotriya, Major Professor
Baskar Ganapathysubramanian
Ganesh Balasubramanian
Thomas J. Rudolphi
Iris V. Rivero

Iowa State University

Ames, Iowa

2015

TABLE OF CONTENTS

ACKNOWLEDGMENTS

First and foremost, I am grateful to my major professor, Dr. Pranav Shrotriya, who is always thoughtful, insightful, and considerate to students. His supports in every single aspect in my research, patient guidance, broad knowledge, critical thinking as well as encouraging style of research set an example as a rigorous scientist. I truly cherish the opportunity to work with him and feel very lucky to be his student.

I would like to thank Dr. Thomas Rudolphi for his guidance in the courses I took. In addition, thank Dr.Baskar Ganapathysubramanian, Dr. Iris Rivero, and Dr. Frank Peters for their time being part of the committee, valuable discussion, and inspiring comments over the evaluation process.

Thank Ammar Melaibari, Yixian Wang, and Jingnan Zhao for conducting the marvelous experiments and providing some of the testing data and results. I also owe many thanks to Dr. Pal. Molian, the Co-PI of my project, for patiently guiding me in experimental aspect and training me of equipments. Also thank Diamond Innovations Inc. for donating the PCBN samples. The financial support from NSF is sincerely acknowledged for awarding the research grant.

Special thanks go to my friends, colleagues, the department faculty and staff for making my time at Iowa State University a wonderful experience.

If there were anybody deserving special awards, it would have to be my beloved parents, who are the most powerful faith in supporting my daily study and each piece of pursuit at ISU. I am indebted to them for their continuous encouragement, endless support, and everlasting love.

ABSTRACT

Ceramics are generally difficult to machine due to their inherent natures of high hardness and low toughness. The present dissertation investigated the mechanism governing cutting of hard ceramic materials with a novel hybrid CO_2-Laser/Waterjet (LWJ) system through controlled fracture propagation. It has been proved that the hybrid machining method is more efficient and is capable of providing high quality cutting that overcomes the major drawbacks with current machining techniques including EDM and Nd:YAG laser. The LWJ method implements a high power laser heating followed by low pressure waterjet quenching which subsequently dictates fracture initiation and propagation along the cutting path. The driving force of fracture can be categorized into two groups based on the specific material's thermal properties and phase transformation capabilities. For materials with low thermal conductivity such as Alumina and Zirconia, laser heating and waterjet quenching cooperatively induce large thermal stresses, which drive the crack and hence achieves material separation. For materials with high thermal conductivity such as Aluminum Nitride, Polycrystalline Cubic Boron Nitride and Polycrystalline Diamond, the stresses that drive the crack propagation result from phase transformation induced volume expansion, rather than thermal stresses. Based on the two mechanisms, the material merit indices governing thermal shock induced fracture and transformation induced fracture can be derived respectively for material selection.

The cutting mechanism of high-conductivity materials including PCBN and PCD was studied through combined experimental and numerical methods. Surface deformation, morphology, and phase compositions were characterized on the cut sample using profilometry, scanning electron microscopy, and Raman spectroscopy in order to identify the mechanistic

origin underlying the material separation. A finite element model was developed to predict the surface deformation, which was compared with surface profiling measurements by optical profilometry in order to estimate the expansion strain and dimensions of the phase transformed region. Fracture mechanics analysis based on the obtained expansion strain and transformed zone was performed to predict crack configurations and to validate experimental cutting results. Based on comparison between experimental observations and numerical predictions, a "score and snap" mechanism is identified: (1) The laser beam results in scoring the sample through localized laser heating and subsequent waterjet quenching transform PCBN near the top surface from sp3-bonded phases into sp2-bonded phases (cBN transforms to hBN, diamond transforms to graphite); (2) The phase transition leads to volumetric expansion that induces tensile stresses in the surrounding material and drives the crack through the specimen leading to material separation.

Cutting results indicate that as line energy of the laser was increased the sample response transitioned from scribing to through cutting. Good agreement between simulation and experimental observation was achieved. The results show that transformation induced crack propagation is the feasible mechanism for cutting during CO2-LWJ machining.

CHAPTER I

INTRODUCTION

1.1 Introduction to brittle ceramics

The past decades have witnessed a rapid development of ceramic materials since the first discovery or general usage of ceramics by human beings. In general, ceramic materials are a class of inorganic and non-metallic solids where the constituent elements that may include metals, nonmetals, or metalloids are ionically and/or covalently bonded. The nature of ionic or covalent bonding gives rise to some unique material properties that allow a wide range of applications for ceramics.

Ceramics are widely used as structural and tooling materials because of their desirable mechanical properties such as high hardness, high wear resistance, high specific strength, and ultra-fine finishing capability. The limited capability of plastic deformation endows them a high stability in maintaining their geometries or shapes. Ceramic materials generally have a lower thermal conductivity and a lower thermal expansion coefficient than metallic materials, which makes them particularly suitable for applications at high temperatures (e.g., thermal barrier coatings). Ceramics also robustly withstand chemical erosion that occurs in other materials subjected to acidic or caustic environments. Most ceramics exhibit superior electrical insulation properties and therefore have been extensively exploited in semiconductor industries[1].

The variety of ceramics' attractive features ironically bring a side effect of a high difficulty or expense in fast processing or producing actual components. The inherent characteristics such as high strength, high hardness, low ductility, and low electrical

conductivity impose a grand challenge in machining ceramics. Most traditional machining techniques are generally precluded, and the cost of producing component geometries is often extremely high as it usually requires the use of expensive and time consuming diamond grinding. On the pathway toward further commercialization of ceramics, it is therefore necessitated to develop a cost-effective machining method which exempts from significantly reducing the beneficial material properties of the processed surface.

1.2 Current machining techniques

1.2.1 Grinding

Grind machining takes place by using grinding wheels that are tightly bonded with abrasives. In the past decades, considerable efforts have been devoted into developing increasingly efficient grinding techniques for machining ceramics[2].Even though the needs for dimensional accuracy and surface finish are satisfying by conventional grinding, the remarkably long machining time and the high machining cost account for 60–90% of the final cost of the finished product. This poses a major challenge for the grinding process[3] and ground products also generate surface and subsurface cracks[4, 5], some permanent or irreversible plastic deformation[6] and significant residual stresses[7]. Previous studies have examined the possibility of the high speed grinding of advanced ceramics[8]. For instance, Hwang et al. [9, 10] systematically investigated the machining characteristics of silicon nitride under high speed grinding conditions. Their research focused on wheel wear mechanisms, again at low removal rates. Klocke et al.[11] studied various process strategies for the high speed grinding of aluminum oxide and silicon-infiltrated silicon carbide at high removal rates.

They found that the fracture strength of the machined ceramic components approximately retains without discernible degradation after the high speed grinding at high removal rates.

Conventionally, machining of ceramics is accomplished through processes such as diamond machining and grinding which suffer from: 1) difficulties in achieving complex contours; 2) low material removal rates; 3) excessive tool wear; and 4) high cost. Consequently non-traditional techniques such as waterjet and laser cutting have emerged as potential alternatives for these mechanical machining processes.

1.2.2 Ultrasonic machining

In principle, ultrasonic machining is operated through ultrasonically vibrated abrasive particles that remove material at generally low material removal rates during ultrasonic machining. With this technique, an induced vibration combined with the abrasive slurry is delivered to a designed tool piece and hence performs a microscopic grinding. Microscopically, ultrasonic machining is analogous to grinding. The abrasive employed is certainly a key factor that needs careful selection for different engineering ceramics. The surface finish, the cavity size on the tool itself, and the achieved cutting rate are closely related to the size of the abrasive particles in the suspension. The first of these 'rotary ultrasonic machining' has been investigated by Rolls Royce as a possible method for profile finish-machining turbine blade aerofoil sections[12]. The arrangement that formed the basis of their interest uses a 20 kHz axially-assisted tool rotating at speeds of up to 3750 rpm. It does not rely on an abrasive slurry for the cutting action, and thus gives rise to a longer tool life. A water coolant and flushing medium was used. The more complex arrangement of Ultrasonic Electrodischarge Grinding (USED-G) has been reported by Uematsu et al. [13]. They revealed appreciably improved stock removal rates by minimizing the grinding forces during machining

of TiB_2. It is worth noting that there is no direct demonstration of comparative surface finish or machining damage in the previous studies, but since these are generally improved by reducing the normal grinding forces, it is conceivable that the technique represents an improvement over conventional grinding in this respect.

1.2.3 Abrasive waterjet machining

Abrasive waterjet technologies have been utilized for cutting ceramic materials [14-16]. However, the use of high-pressure water (> 36,000 psi or 250 MPa) along with abrasives in water-jet requires special pressure intensifiers and sapphire nozzles that are costly and have limited flow capacity. In addition, ceramic parts cut by abrasive water-jet exhibit large kerf width and poor surface roughness. Recently, Xu and Wang[16] have proposed controlled nozzle oscillation to improve the cut quality. However, the resulting improvements are only marginal and the cut quality is still inferior to that obtained by conventional diamond machining. Axinte, D. A., et al.[17] investigated cutting of PCD with abrasive waterjet. Their result shown that diamond abrasives can achieve a material removal rate of 249.9 mm3/min. However, drawbacks like high nozzle wear, high cost of abrasives and large kerf taper need to be addressed for implement in industry.

1.2.4 Electrical machining

EDM is a technique exclusively for machining electrically conductive, and semi-conductive materials. The general mechanism is the melting and evaporation of the electrodes for illustrating how the high energy plasma produced by the electrical discharge affects the removal of material. As the current flow ceases, the resulting violent collapse of the plasma and the associated vapor causes superheated molten liquid on the surface of each electrode to explode into the gap, where it resolidifies in the liquid dielectric and leave melted material on

the sample. Y.K. Lok and T. C. Lee[18] reported wire-EDM cutting of AL2O3-TiC advanced ceramics with low material removal rate of 2-8mm/min and produced thermal defects on the surface of the machined sample. The advantages of EDM are not inconsiderable: the ability to machine complex shapes; it places no mechanical stress on the workpiece; and its relatively high material removal rates ensure that it certainly has a valid area of application. The overwhelming disadvantage is that it is limited to conductive materials and produced thermal affected zone. Generally, EDM techniques are not affected by material hardness, but do require an electrical resistivity less than 100 Ωcm. A number of researchers have investigated the feasibility of making additions to insulating ceramic compositions that render them sufficiently conductive to allow EDM to be used.

1.2.5 Laser machining

In the past few decades, laser technology has also been successfully applied for cutting hard ceramic materials [19-21]. During laser machining, the material separation may be accomplished through four different modes: vaporization; melt and blow; scribing; or thermal fracture[22]. The first two modes are energy intensive processes requiring power density in excess of 1000 W/m^2. These high-energy processes also induce residual stresses in the material (because of excessive thermal heating) that may subsequently affect the strength of the finished product. Laser scribing followed by mechanical breaking is energy efficient but does not yield good finishing due to melting and resolidification of surface material. Lumley[21] is one of the early researchers who proposed the thermal fracture mode due to its low energy requirement. Thermal gradients resulting from the absorption of light energy cause thermo-mechanical stresses sufficiently high to fracture the material. Tsai and Liou[20] have performed a number of experiments in thermal fracture mode of cutting alumina using the CO_2

laser. Elperin et al.[23] proposed a thermal fracture model for scoring glass and silicon wafers, wherein the wafer is heated by a laser beam and is immediately cooled by an air/water spray. Kondratenko[24] has patented the idea of cutting non-metallic materials by heating the substrate to temperatures below its softening point and cooling the heated zone subsequently to induce a blind crack. The blind crack then propagates to split the material apart. The effectiveness of this approach was demonstrated through experiments on a Na-K glass. Contemporary non-traditional processes such as laser and waterjet which offer benefits over traditional processes for cutting brittle materials suffer from: high-power requirements (lasers ~ 2-10 kW, waterjet ~ 1 kbar pressure), energy inefficiency, hazardous environment (laser and waterjet), abrasive requirements (waterjet), slow machining rates (waterjet), wear of machinery components (waterjet), etc.

1.2.6 Hybrid machining

Hybrid machining uses a combination of two or more of the above techniques for machining ceramics, such as laser-assisted chemical etching/machining[25], cutting tool/laser assisted machining(LAM)[26] and Synova microjet®[27]. In laser-assisted chemical etching, material removal is carried out by using suitable etchant in combination with selective laser irradiation. The laser radiation influences the reaction between the material and the etchant by exciting the etchant molecules and/or the material surface and the etch rate is significantly affected by the laser fluency. In laser assisted machining (LAM), the material is locally heated by an intense laser source prior to material removal, without melting or sublimation of the ceramic. This technique has been successfully used for machining silicon nitride and the corresponding work piece temperature, tool wear, and surface integrity have been measured [28-30]. In LAM, after the laser is used to change the ceramic deformation behavior from

brittle to ductile, material removal takes place with a conventional cutting tool. It effectively reduces the cutting force and improves the surface finish of the finished products made from Al_2O_3[26]. Laser-microjet® [31] developed by Swiss Federal Institute of Technology allows precise cutting of PCD materials by employing a Q-switched pulsed laser at an average power of 300 W at 532 nm wavelength and water pressure of 2-10 MPa. However, the process suffers from slow cutting speeds (e.g., 72 mm/min for a 0.5 mm thick PCD substrate).

1.3 Innovative Laser/Waterjet(LWJ) technique

Given the limitations of the existing machining methods of ceramics, a novel process of combining continuous wave CO_2 laser and water-jet (LWJ) was developed by our group to improve the machining efficiency and quality[32-35]. The CO_2-LWJ machining system (schematically shown in Figure 1.1) implements a high power laser heating followed by low pressure waterjet quenching, which altogether achieve fracture initiation and controlled propagation along the cutting path.

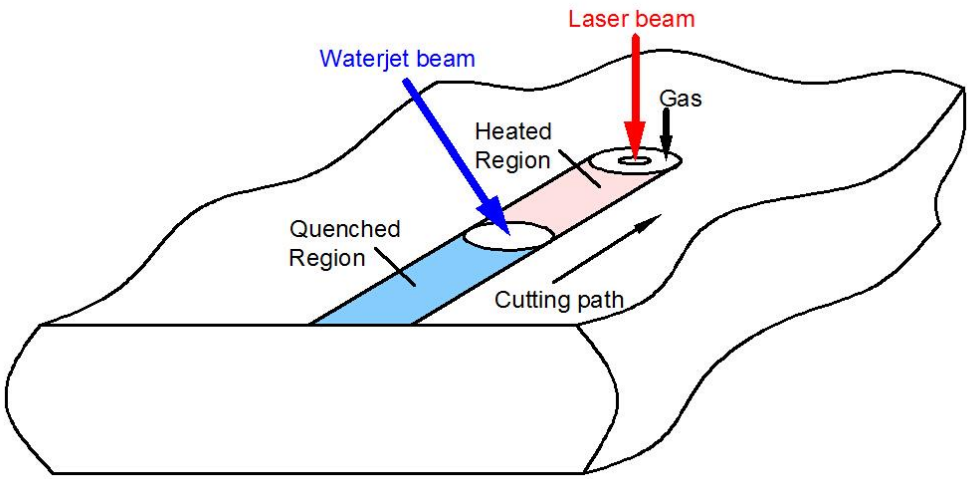

Figure 1.1. *Schematic representation of CO2-LWJ machining system*

Figure 1.2 shows a model diagram of the laser/water-jet machining head. This LWJ head assembly is designed in order to be mounted on the existing laser focusing hardware. The laser beam and assist gas are directed to workpiece surface through the central hole while the water is pumped from the inlet port to the exit port through an adjacent passage as shown in Figure 1.2 . The distance between the laser spot and the water-jet on the surface of the material can be varied by changing the orifice angle. In addition, a belt system is provided to allow the rotation of head to fulfill 2-dimensional contour cutting. The head design allows the gas-assisted laser beam to focus as well as permit water-jet flow and its commutation. The fractured debris is removed through the kinetic energy of water jet. In this way, the formation of liquid and gaseous phases can be avoid, making the process energy efficient as well as free from hazardous emission. It also meets several challenges, such as space constraint, sealing, and water control around sensitive laser components.

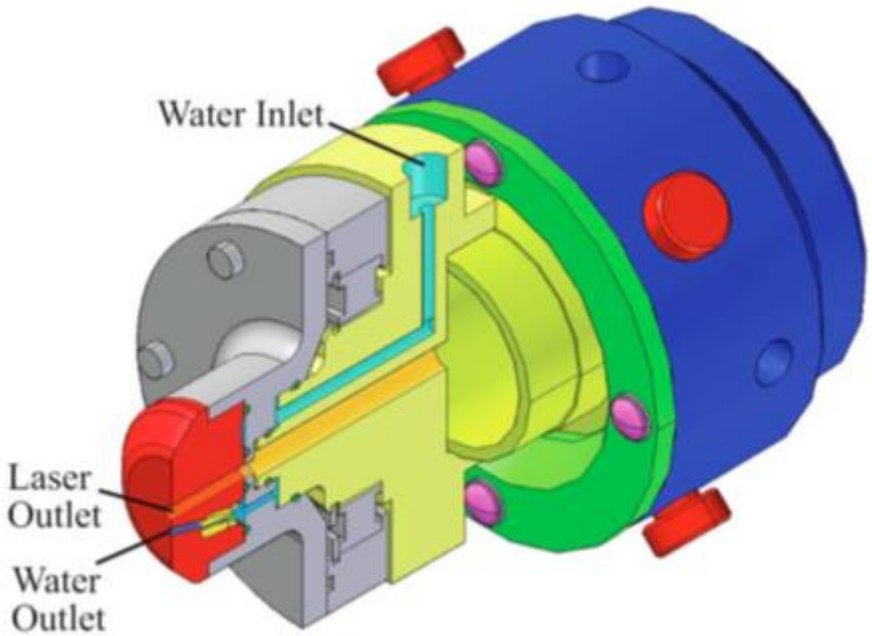

Figure 1.2. *Solid model of the Laser/Waterjet cutting head*

The experimental setup of the LWJ system is represented in Figure 1.3. A continuous wave CO2 Laser (Model 820 Spectra Physics) of 10.6 μm wavelength and 1.5 kW rated power was used in the LWJ system. The laser head has been modified to accommodate the low-pressure waterjet (< 1000psi or < 8MPa) to realize CO2-LWJ machining. A CNC table with freedom in horizontal plane was implemented to control the movement of sample mounted on it. The beam from the laser was sent through a focusing lens and irradiated on the sample surface. A 127 mm focal length lens was used to produce the focal spot diameter of 0.2 mm. A defocused spot with diameter larger than 0.2mm can be achieved through adjusting the distance between laser head and sample surface. The distance between waterjet and laser beam was determined from the location of spray hole for water on the laser nozzles. Three nozzles with spacing of 2 mm, 4mm and 6mm between water and laser was manufactured. Laser beam was surrounded by gases with a designed pressure in order to prevent direct interaction of laser and water jet.

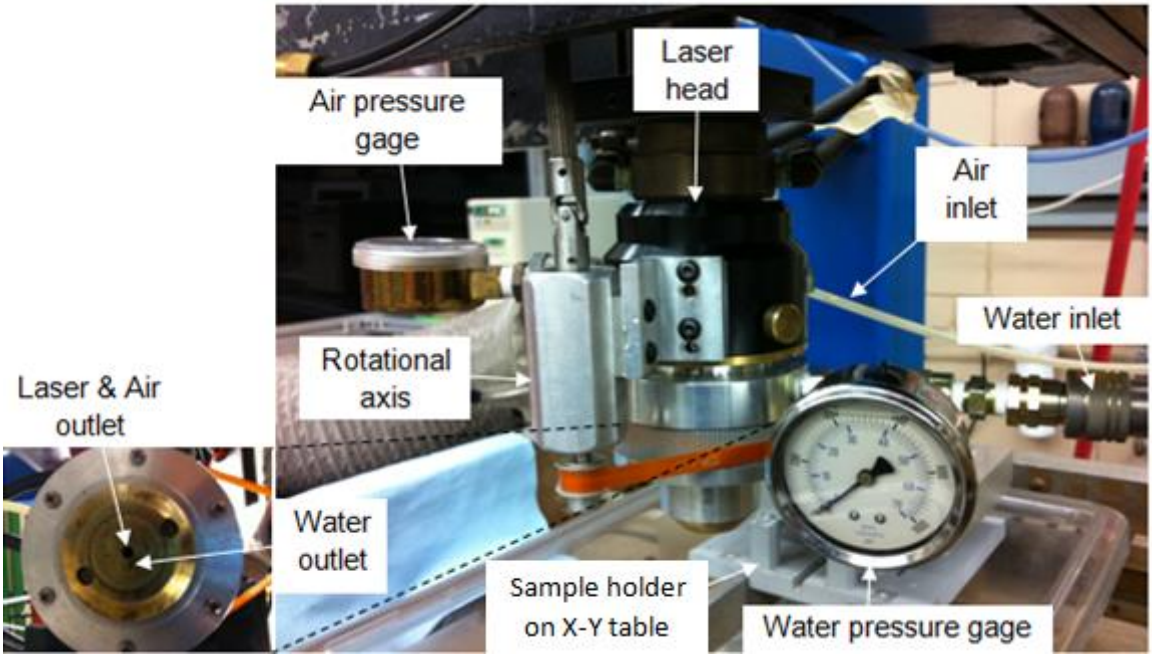

Figure 1.3. *Experimental setup of CO2-LWJ machining system*

1.4 Motivation

The LWJ machining method uses an entirely different mechanism than conventional laser machining of material removal through melting and ablation. It achieved the material separation through controlled crack propagation which will be much faster and free of heat affected zone.

The "Controlled fracture propagation mechanism" is an energy efficient process as low-powered lasers, operating below the melt/ablation threshold, are utilized for localized heating of workpiece and a gas stream is added for cooling the heated zone, leading to fracture of sample. The main feature that differentiate the proposed LWJ machining process is that elements of laser and waterjet machining can be synergistically combined such that material removal is accomplished by fracture propagation of material into fine fragments rather than energy intensive erosive wear or melting and subsequent evaporation. The advantages of the fracture separation process by LWJ process are: 1) the maximum temperature is significantly below the melting point; 2) cut surfaces are free of large visible defects; and 3) the process is environmentally friendly as there is near zero amount of material removal; 4) Small chips formed, if any, are washed away by the waterjet. Thus, controlled thermal fracturing obtainable through hybrid LWJ machining can meet the challenges of higher feed rate, reduced energy and improved environment in the shaping of ceramics. In addition, the LWJ hybrid process is exempt from forming liquid or gaseous phases, and such feature allows it more energy efficient and free from hazardous emission.

1.5 Thesis organization

Chapter 1 provides the background information of the ceramic properties, the existing manufacturing techniques, the design and principle of Laser/Waterjet (LWJ) machining system and the motivation for this study.

Chapter 2 categorizes the fracture propagation mechanism in two groups based on the specific material's thermal properties and phase transformation capabilities. Merit indices for the two mechanisms are developed to rank material selection.

Chapter 3 investigates the single-pass LWJ cutting experiments of Polycrystalline Cubic Boron Nitride (PCBN) and identifies the mechanism governing the material separation through phase transformation induced fracture propagation.

Chapter 4 analyzes the cutting of double-layer composite PCBN supported by tungsten carbide. A new method that combining single-pass focused beam and multi-passes defocused beam was applied that successfully achieved separation of the specimen.

Chapter 5 discusses LWJ machining of PCBN specimen under different assist gases/media including Argon, Nitrogen and Waterjet. Experimental and modeling approaches are both performed to rank the assist media.

Chapter 6 investigates the single-pass LWJ cutting experiments of tungsten carbide supported Polycrystalline Diamond (PCD). The same modeling and measuring approach are used to understanding the material separation mechanism through phase transformation induced fracture propagation.

Chapter 7 reports the hardness improvement of PCBN (50% cubic phase and 50% wurtzite phase) under Laser/Waterjet Heat Treatment (LWHT). The atomic model of nano-twinned cBN microstructures, lamella microstructures of cBN/wBN with coherent twin grain

boundaries are developed. Atomic simulations of indentation shearing are performed in LAMMPS to analyze strength change as a function of grain size for these microstructures.

Chapter 8 presents the general conclusions and proposes future works.

1.6 References

[1] C. A. Harper, *Handbook of Ceramics, Glasses and Diamonds*: Mc Graw Hill, 2001.

[2] A. N. Samant and N. B. Dahotre, "Laser machining of structural ceramics-A review," *Journal of the European Ceramic Society*, vol. 29, pp. 969-993, Apr 2009.

[3] G. Chryssolouris, N. Anifantis, and S. Karagiannis, "Laser assisted machining: An overview," *Journal of Manufacturing Science and Engineering-Transactions of the Asme*, vol. 119, pp. 766-769, Nov 1997.

[4] B. G. Koepke and R. J. Stokes, "A Study of Grinding Damage in Magnesium Oxide Single Crystals," *Journal of Materials Science*, vol. 5, pp. 240-&, 1970.

[5] H. P. Kirchner, "Damage Penetration at Elongated Machining Grooves in Hot-Pressed Si3n4," *Journal of the American Ceramic Society*, vol. 67, pp. 127-132, 1984.

[6] H. H. K. Xu and S. Jahanmir, "Microfracture and Material Removal in Scratching of Alumina," *Journal of Materials Science*, vol. 30, pp. 2235-2247, May 1 1995.

[7] B. Zhang, X. L. Zheng, H. Tokura, and M. Yoshikawa, "Grinding induced damage in ceramics," *Journal of Materials Processing Technology*, vol. 132, pp. 353-364, Jan 10 2003.

[8] T. W. Hwang, C. J. Evans, and S. Malkin, "An investigation of high speed grinding with electroplated diamond wheels," *Cirp Annals 2000: Manufacturing Technology*, pp. 245-248, 2000.

[9] T. W. Hwang, C. J. Evans, E. P. Whitenton, and S. Malkin, "High speed grinding of silicon nitride with electroplated diamond wheels, part 1: Wear and wheel life," *Journal of Manufacturing Science and Engineering-Transactions of the Asme*, vol. 122, pp. 32-41, Feb 2000.

[10] T. W. Hwang, C. J. Evans, and S. Malkin, "High speed grinding of silicon nitride with electroplated diamond wheels, part 2: Wheel topography and grinding mechanisms," *Journal of Manufacturing Science and Engineering-Transactions of the Asme*, vol. 122, pp. 42-50, Feb 2000.

[11] S. Jahanmir, M. Ramulu, and P. K. (Ed.), *Machining of Ceramics and Composites*: Marcel Dekker, 1999.

[12] I. P. Tuersley, A. Jawaid, and I. R. Pashby, "Various Methods of Machining Advanced Ceramic Materials - Review," *Journal of Materials Processing Technology*, vol. 42, pp. 377-390, May 1994.

[13] T. Uematsu, K. Suzuki, T. Yanese, and T. Nakagawa, *Machining of Ceramics and Composites*: CRC Press, 1999.

[14] J. Wang, "Abrasive waterjet machining of polymer matrix composites - Cutting performance, erosive process and predictive models," *International Journal of Advanced Manufacturing Technology*, vol. 15, pp. 757-768, 1999.

[15] J. Wang and D. M. Guo, "The cutting performance in multipass abrasive waterjet machining of industrial ceramics," *Journal of Materials Processing Technology*, vol. 133, pp. 371-377, Feb 20 2003.

[16] S. Xu and J. Wang, "A study of abrasive waterjet cutting of alumina ceramics with controlled nozzle oscillation," *International Journal of Advanced Manufacturing Technology*, vol. 27, pp. 693-702, Jan 2006.

[17] D. A. Axinte, D. S. Srinivasu, M. C. Kong, and P. W. Butler-Smith, "Abrasive waterjet cutting of polycrystalline diamond: A preliminary investigation," *International Journal of Machine Tools & Manufacture*, vol. 49, pp. 797-803, Aug 2009.

[18] Y. K. Lok and T. C. Lee, "Processing of advanced ceramics using the Wire-Cut EDM process," *Journal of materials processing technology*, vol. 63, pp. 839-843, 1997.

[19] J. C. Rozzi, F. E. Pfefferkorn, Y. C. Shin, and F. P. Incropera, "Experimental evaluation of the laser assisted machining of silicon nitride ceramics," *Journal of Manufacturing Science and Engineering-Transactions of the Asme*, vol. 122, pp. 666-670, Nov 2000.

[20] C. H. Tsai and C. S. Liou, "Fracture mechanism of laser cutting with controlled fracture," *Journal of Manufacturing Science and Engineering-Transactions of the Asme*, vol. 125, pp. 519-528, Aug 2003.

[21] R. M. Lumley, "Controlled Separation of Brittle Materials Using a Laser," *American Ceramic Society Bulletin*, vol. 48, pp. 850-&, 1969.

[22] W. Steen, *Laser Materials Processing, 3rd Edition*: Springer, 2003.

[23] T. Elperin and G. Rudin, "Controlled fracture of nonmetallic thin wafers using a laser thermal shock method," *Journal of Electronic Packaging*, vol. 126, pp. 142-147, Mar 2004.

[24] V. S. Kondratenko, "Method of splitting Non-metallic materials," US Patent, 1977.

[25] H. Horisawa, N. Akimoto, H. Ashizawa, and N. Yasunaga, "Effects of a quartz beam-guide on high-precision laser-assisted etching of Al2O3 ceramics," *Surface & Coatings Technology,* vol. 112, pp. 389-393, Feb 1999.

[26] C. W. Chang and C. P. Kuo, "An investigation of laser-assisted machining of Al2O3 ceramics planing," *International Journal of Machine Tools & Manufacture,* vol. 47, pp. 452-461, Mar 2007.

[27] A. Pauchard, M. D. Marco, B. Carron, G. Suruceanu, B. Richerzhagen, A. Brulé, *et al.*, "Recent Developments in the Cutting of Ultra Hard Materials Using Water Jet-Guided Laser Technology," presented at the ALAC, 2008.

[28] S. Lei, Y. C. Shin, and F. P. Incropera, "Experimental investigation of thermo-mechanical characteristics in laser-assisted machining of silicon nitride ceramics," *Journal of Manufacturing Science and Engineering-Transactions of the Asme,* vol. 123, pp. 639-646, Nov 2001.

[29] J. C. Rozzi, F. P. Incropera, and Y. C. Shin, "Transient, three-dimensional heat transfer model for the laser assisted machining of silicon nitride: II. Assessment of parametric effects," *International Journal of Heat and Mass Transfer,* vol. 43, pp. 1425-1437, Apr 2000.

[30] S. T. Lei, Y. C. Shin, and F. P. Incropera, "Deformation mechanisms and constitutive modeling for silicon nitride undergoing laser-assisted machining," *International Journal of Machine Tools & Manufacture,* vol. 40, pp. 2213-2233, Dec 2000.

[31] O. Sibailly, F. Wagner, L. Mayor, and B. Richerzhagen, "High precision laser processing of sensitive materials by Microjet (R)," *Fourth International Symposium on Laser Precision Microfabrication,* vol. 5063, pp. 501-504, 2003.

[32] R. Molian, P. Shrotriya, and P. Molian, "Thermal stress fracture mode of CO2 laser cutting of aluminum nitride," *International Journal of Advanced Manufacturing Technology*, vol. 39, pp. 725-733, Nov 2008.

[33] D. Kalyanasundaram, P. Shrotriya, and P. Molian, "Obtaining a Relationship Between Process Parameters and Fracture Characteristics for Hybrid CO2 Laser / Waterjet Machining of Ceramics," *Journal of Engineering Materials and Technology*, vol. 131, 2009.

[34] D. Kalyanasundaram, P. Shrotriya, and P. Molian, "Fracture mechanics-based analysis for hybrid laser/waterjet (LWJ) machining of yttria-partially stabilized zirconia (Y-PSZ)," *International Journal of Machine Tools & Manufacture*, vol. 50, pp. 97-105, Jan 2010.

[35] D. Kalyanasundaram, G. Shehata, C. Neumann, P. Shrotriya, and P. Molian, "Design and validation of a hybrid laser/water-jet machining system for brittle materials," *Journal of Laser Applications*, vol. 20, pp. 127-134, May 2008.

CHAPTER II

THE MECHANISM GOVERNING CUTTING OF CERAMICS THROUGH THERMAL AND TRANSFORMATION STRESSES

Abstract

Material separation in Laser/Waterjet machining is achieved through controlled fracture propagation. The driving force of fracture can be categorized into two groups based on the specific material's thermal properties and phase transformation capabilities. For materials with low thermal conductivity (Alumina, zirconia), laser heating and waterjet quenching cooperatively induce a precipitous temperature gradient inside the specimen, analogous to the so-called "thermal shock" effect. Thermal stresses are developed accordingly to propagate the crack and to achieve material separation. For materials with high thermal conductivity (AlN, PCBN, PCD), the heat is dissipated rapidly through conduction during machining and hence the thermal stresses are negligible and insufficient to propagate the crack. However, the existence of phase transformation during machining often expands the initial volume and leads to the formation of residual tensile stresses within the sample that promotes the crack propagation. The cracking in machining this type of materials is often driven by the highly constrained thermal expansion that originates from phase transformation. Based on the two mechanisms, the material merit indices governing thermal shock induced fracture and transformation induced fracture can be derived for material selection.

KEYWORDS: controlled crack propagation, thermal shock, phase transformation

2.1 Thermal shock induced fracture

For low thermal conductive materials, material separation is achieved by thermal shock induced fracture propagation. Laser heating followed by waterjet cooling creates a thermal shock on the material's surface. The heated area tends to expand, but is constrained by the surrounding material and thereby compressive stresses form in the heated area. Subsequent rapid quenching of this zone by a low-pressure water-jet causes the alteration in the stress state from compressive to tensile. Depending on the magnitude of the tensile stresses created and the fracture toughness of the material, these micro-cracks may extend and even penetrate throughout the thickness of the material. The cracks generally follow the laser waterjet moving path as the tensile stresses are maximum along the path. Consequently, material separation is accomplished through a controlled propagation of cracks along the LWJ beam and the resulting cut surfaces are expected to be free of thermal damage or residual stresses.

A measure of fracture under thermal shock is taken to be the temperature jump ΔT inside a brittle material [1]. The value of ΔT is sensitive to Biot number ($Bi = \frac{hH}{k}$), the dimensionless quantity used to measure the ratio of the heat transfer inside of and at the surface of a body. This ratio determines whether or not the temperatures inside a body will vary significantly in space, while the body heats or over time, from a thermal gradient applied to its surface.

In order to evaluate the thermal stress distribution over a range of Biot numbers, a numerical model is developed in commercial finite element analysis package ABAQUS (Simulia, Providence, RI) as shown in Figure 2.1. Simulation of a movable heat source in ABAQUS requires the implementation of DFLUX subroutines written in FORTRAN programming language, where the heat source intensity can be determined with desired

distribution. The model is composed of 4-noded linear elements of coupled thermal-displacement type. Meshes are refined at the location closed to laser path and a section of fine meshes in the middle of the path is assigned in order to save calculation time. Due to the symmetric distribution of laser beam, only half of the specimen is modeled with boundary conditions of thermal isolation and zero displacement in the plane of symmetry. The laser beam is modeled using a surface heat source with Gaussian energy distribution. The intensity profile of the Gaussian laser beam is described by following equation[2]:

$$I(x,y) = I_h(1 - r_f)\exp\left[-\left(\frac{x}{r}\right)^2 - \left(\frac{y}{r}\right)^2\right]$$

$$I_h = \frac{P}{\pi r^2} \quad (2.1)$$

Where P is the laser power, r is the radius of laser spotsize and r_f is the reflectivity of material. Speed of moving heat source is keeping constant at 42 mm/s (100in/min), which is one of the actual machining condition. Laser power and laser spotsize are also constant based on the actual cutting condition of P=500W and r=0.1mm. Reflectivity was assumed to be 30% in the current work. This value can be determined from inferred spectrum for different materials. The boundary conditions applied on the top surface for waterjet quenching was modeled using a convective heat transfer coefficient of h=10000W/($m^2 \cdot K$) reported for forced convection of water flow. The convective coefficient of bottom surface was chosen to be h=50W/($m^2 \cdot K$) for natural air convection.

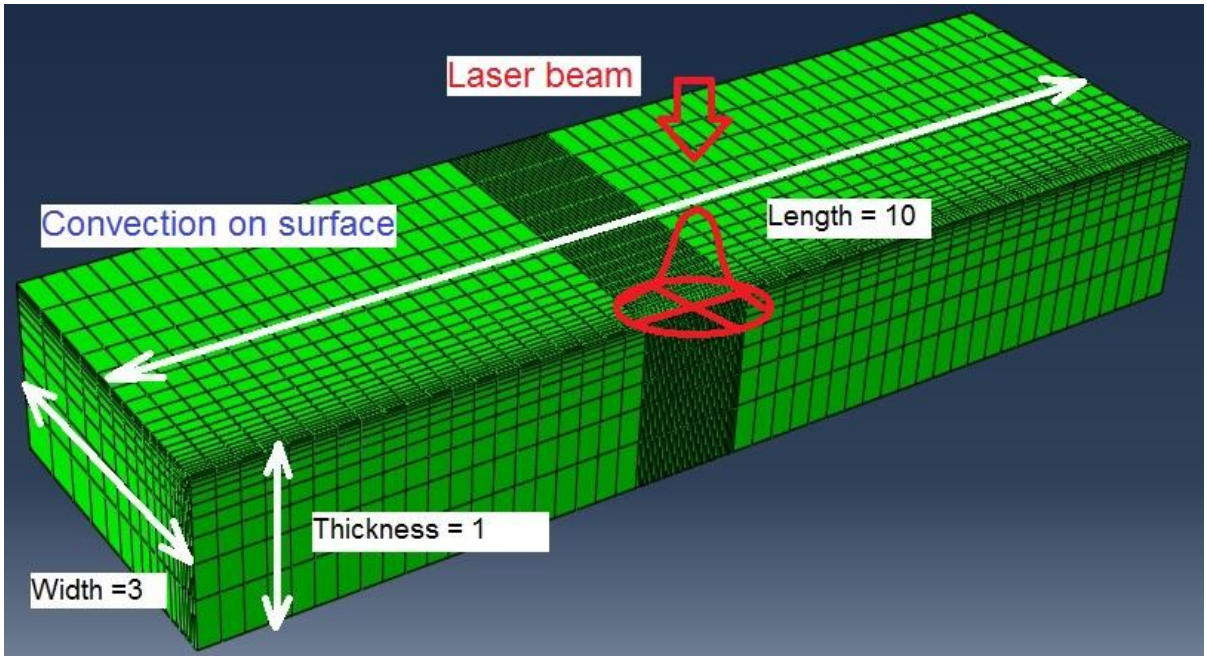

Figure 2.1. *Finite element model for thermal analysis stress*

The value of Biot number (Bi $= \frac{\mathrm{hH}}{\mathrm{k}}$) is varied by changing thermal conductivity while keeping the same value of convective coefficient on top surface. All the other material properties and processing conditions are assumed to be the same in order to explore the effect of thermal conductivity for different materials. Figure 2.2 and Figure 2.3 plotted the temperature distribution and thermal stress σ_{zz} on the plane of symmetry for selected Biot number. For comparison purposes, the results are scaled based on the maximum and minimum value of temperature and σ_{zz} for each selected Biot number. The maximum temperature is attained at the center of the heat flux and drops rapidly due to surface convection. Compressive stress is developed at the center of the heating source, while tensile stress is induced adjacent to the heat source due to large temperature jump.

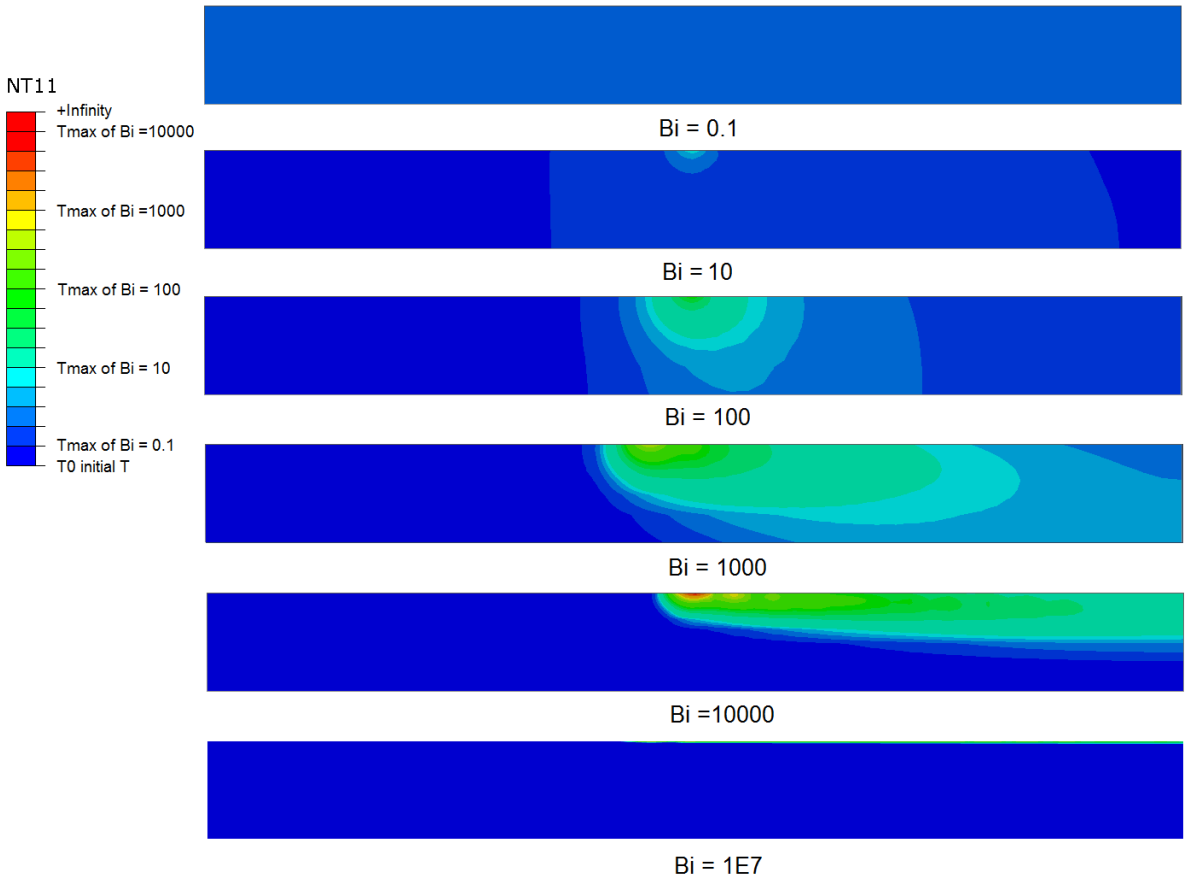

Figure 2.2. *Temperature distribution on the plane of symmetry for selected Biot number*

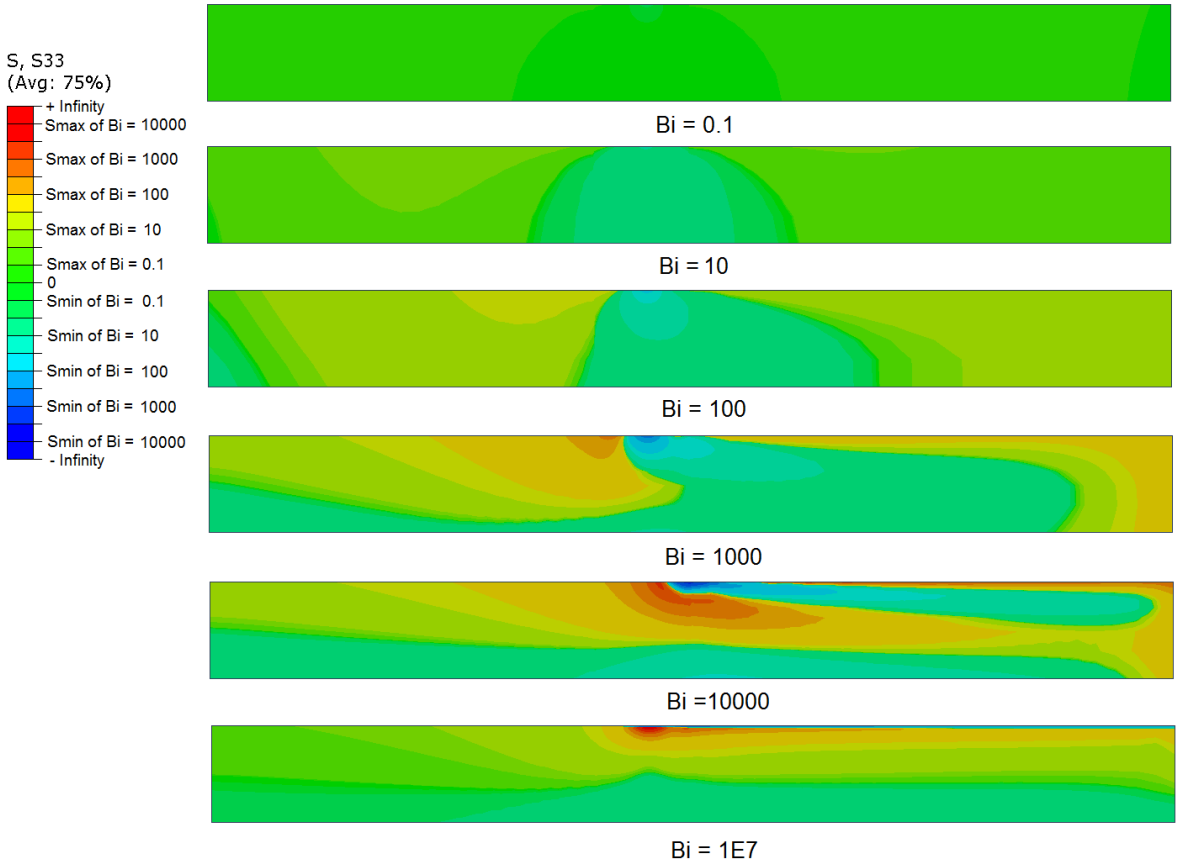

Figure 2.3. *Thermal stress σ_{zz} distribution on the plane of symmetry for selected Biot number*

The overall magnitude of temperature and stresses increase significantly with increasing Bi. When Bi is small (Bi = 0.1), temperature is almost uniformly distributed and stress is negligible. As Bi increasing to a larger value, both temperature and thermal stresses increase accordingly. In the situation with extremely large Bi, material is almost insulate that can hardly transfer heat. Heat accumulates on a very thin layer near top surface without dissipation. Therefore only compressive σ_{zz} is developed on the surface in this case. Figure 2.4 represents the reduced stress distribution along the model thickness at the location of

cooling zone (1mm away from the heat flux). This gives a rough estimate of the thermal stress magnitude.

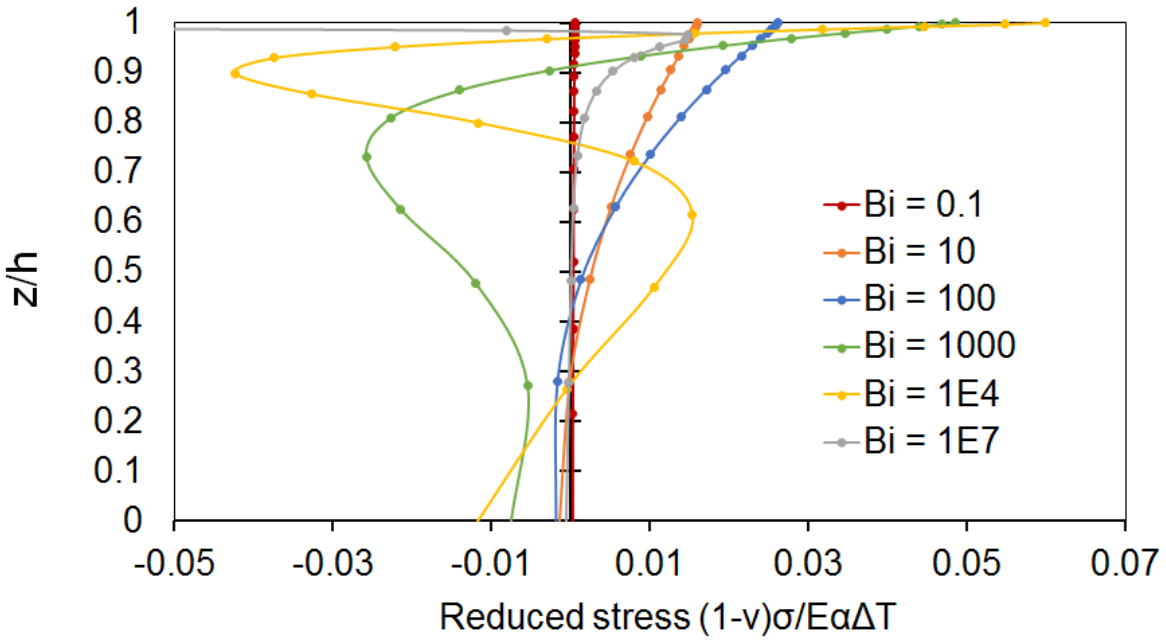

Figure 2.4. *Reduced thermal stress σ_{zz} distribution along thickness at the center of cold shock for selected Biot number*

Detailed analytical solution of the thermal stress and fracture mechanics analysis under LWJ machining of ceramics with low thermal conductivities have been reported in previous publications (Y2O3 stabilized Zirconia[3] and Alumina[4]). Temperature distributions were determined from the heat transfer differential equation: $c_p \rho \frac{\partial T}{\partial t} = k\nabla^2 T + q$. Stresses normal to crack opening direction was determined from temperature gradient. The stress intensity factors were calculated using the weight function method and the crack energy release rates for channeling along the laser path were obtained by integration of the plane strain energy. The calculated channeling energy release rate was compared with material's specific fracture toughness to predict crack behaviors. Close agreement was obtained between modeling results

and experimental observations for LWJ cutting at different processing parameters. The result proved that the thermal shock mechanism is an effective one in understanding LWJ machining of low thermal conductive materials.

2.2 Transformation expansion induced fracture

Based on the thermal stress investigation discussed above, materials with high thermal conductivities may not fracture due to thermal shock because of the rapid heat dissipation. However, for materials that can change phase under high temperature condition, fracture propagation can be achieved through transformation induced stress. For example, Diamond could convert to graphite at zero pressure as temperature approaches 1500 ℃ and such a phase transformation can be accelerated above 2100 ℃[5]; Boron Nitride exhibits in the form both diamond-like sp3-bonded phases – cubic (cBN) or wurtzite (wBN) phases -- and graphite-like sp2 phases – hexagonal (hBN). Transformation of sp3-bonded tetrahedral structure(PCBN, PCD) to sp2-bonded structure(hBN, graphite) is associated with a large volumetric expansion[6] [7]. During the LWJ cutting experiments, the laser irradiated sample surface may undergo a phase transformation and induce a volumetric expansion that may lead to deformation and development of a stress field in the surrounding material. The stresses helped propagate the crack formed during laser beam passing and achieved material separation throughout the thickness.

The transformed material can be modeled as an elastic plate with a region of expansion. For an axis-symmetric problem of an infinite body, Galerkin[8] introduced a stress function φ satisfying $\nabla^4\varphi = 0$ applied to a point in three dimensions of a certain coordinate system such that displacement components can be written as

$$u_r = -\frac{1}{2G}\frac{\partial^2\varphi}{\partial r\,\partial z}, \qquad u_z = \frac{1}{2G}\left[2(1-\nu)\nabla^2\varphi - \frac{\partial^2\varphi}{\partial z^2}\right] \quad (2.2)$$

And stress components are

$$\sigma_r = \frac{\partial}{\partial z}\left[\nu\nabla^2\varphi - \frac{\partial^2\varphi}{\partial r^2}\right],$$

$$\sigma_\theta = \frac{\partial}{\partial z}\left[\nu\nabla^2\varphi - \frac{1}{r}\frac{\partial\varphi}{\partial r}\right],$$

$$\sigma_z = \frac{\partial}{\partial z}\left[(2-\nu)\nabla^2\varphi - \frac{\partial^2\varphi}{\partial z^2}\right],$$

$$\sigma_{r\theta} = \frac{\partial}{\partial z}\left[(1-\nu)\nabla^2\varphi - \frac{\partial^2\varphi}{\partial z^2}\right] \quad (2.3)$$

Where ∇^2 is Laplace operator, G is the shear modulus and ν is the poison ratio.

For an infinite solid, assuming the expanding point is located at (x_0, y_0, z_0), the Galerkin function φ at point (x, y, z) due to the elastic effect of expansion ε_T is (Mindlin & Cheng 1950)

$$\varphi_0 = \frac{G\varepsilon_T(1+\nu)}{2\pi(1-\nu)}\ln(R+z) \quad (2.4)$$

Where $R = |(x-x_0)^2 + (y-y_0)^2 + (z-z_0)^2|$ is the distance from the desired point to the center of dilatation. Yu and Sanday [9] developed a method of integrating infinite virtual images to solve the boundary value problem of a finite plate of thickness h. Boundary conditions $\sigma_z = \sigma_{rz} = 0$ on both plane z=0 and z=h are satisfied. Exact analytical solutions can be obtained for a model with a spherical region of dilatation located inside an elastic plate as shown in Figure 2.5. The stress distribution along the thickness of specimen is reduced by a factor of $(1-\nu)/E\varepsilon_T$ and can be compared with the reduced thermal stress shown in Figure 2.5. It can be observed from Figure 2.4 and Figure 2.5 that transformation expansion induces a larger magnitude of stress compared with thermal shock induced stress.

In addition, the finite element method was also utilized to compute the same case. A comparison of the FEM solution with the analytical solution of reduced σ_r along z axis is also

presented in Figure 2.5. Mesh of the finite element model was refined till the computed stress became independent of the mesh size. The analytical and the numerically computed stress distributions follow each other. This suggests that the finite element model can accurately determine the stresses induced due to the expansion of the transformed zone.

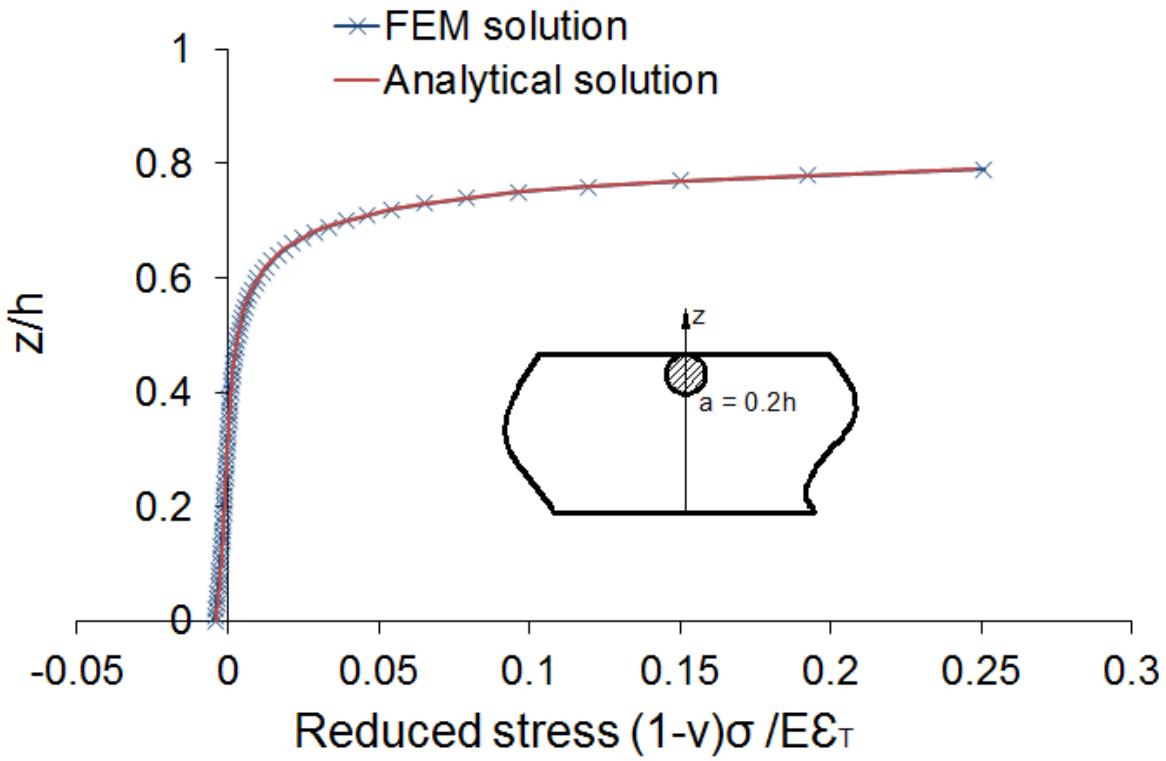

Figure 2.5. *Comparison of FEM with theoretical solution*

Finite element model can be used for solving complex shape of expanding region. The LWJ beam induced transformation zone can be approximated by a semi-elliptical shape. Detailed analysis procedure will be discussed in the following chapters of 3 - 6. Fracture mechanics analysis was performed in three steps: (1) finite element model of 2D plane strain state was developed to evaluate fracture energy release rate by J-integral method at different crack depths; (2) crack channeling was analyzed by integrating and averaging plain strain

energy release rates over all the crack depths; (3) computed channeling fracture energy was compared to critical energy release rate of specific materials to predict fracture behaviors.

2.3 Processing map that determine the cutting mechanism

Based on the analysis above, the material merit indices governing thermal shock induced fracture and transformation induced fracture can be derived for material selection. Temperature gradient within the specimen can be expressed by Fourier's law of thermal conduction as:

$$\Delta T = \frac{\vec{q}\, H}{k}$$

Stress intensity factor K can be expressed by:

$$K = E\alpha\Delta T\sqrt{\pi a} = \frac{\vec{q}\, H}{k}\, E\alpha\sqrt{\pi a}$$

The fracture criterion is taken to be that the stress intensity factor K attains the fracture toughness (or critical stress intensity factor) of the solid, K_{IC}. Materials that are easy for machining would have K much larger than K_{IC}:

$$\frac{\vec{q}\, H}{k}\, E\alpha\sqrt{\pi a} > K_{IC}$$

$$\vec{q}\, H\sqrt{\pi a} > \frac{kK_{IC}}{E\alpha}$$

The left side of the equation refers to the cooling intensity, the thickness of specimen, and the initial crack depth produced by LWJ beam, respectively. The right side of the equation represents material properties that need to be minimized to facilitate thermal shock machining. Therefore, the best materials would have the largest value of the material property indice $\frac{E\alpha}{kK_{IC}}$.

A similar strategy can be formulated to rank materials' processability on the basis of phase transformation induced fracture. The stress intensity factor K associated with transformation stain ε_T can be expressed by:

$$K = E\varepsilon_T\sqrt{\pi a}$$

Materials that are easy to be cut would have K much larger than K_{IC} :

$$E\varepsilon_T\sqrt{\pi a} > K_{IC}$$

$$\varepsilon_T\sqrt{\pi a} > \frac{K_{IC}}{E}$$

It can be well understood that, for phase transition induced fracture, the lower value of $\frac{K_{IC}}{E}$ will be beneficial for machining. Hence the best candidate materials would have the largest value of $\frac{E}{K_{IC}}$.

It is not a well-defined task in mechanistically clarifying whether a specific material is cut through the mechanism of thermal shock or phase transformation. An instructive route is to plot data of engineering ceramics on a map for both of the cases, with axes $\frac{E\alpha}{kK_{IC}}$ and $\frac{E}{K_{IC}}$. The Ashby's chart for material selection[10] and Cambridge Materials Selector software is particularly useful in this regard. Figure 2.6 demonstrates the material selection map for machining most commonly used ceramics (yellow) and glasses (pink) within the framework of the two distinct mechanisms. Materials that are cut by phase transformation induced fracture lie to the right of the diagram, whereas materials that readily fracture by thermal shock lie to the top of the diagram. For instance, Y_2O_3 stabilized Zirconia lie at the left and top portion of the diagram and hence are suitable to be cut by thermal shock. This prediction agrees with the experiment observation that Y-PSZ has been successfully cut by thermal shock induced fracture. A similar case happened with Alumina, another material suitable to be cut by thermal

shock. The location of Alumina, as shown in the diagram, is on the top and left part. Diamond and PCBN are located at the right and bottom portion of the diagram, which indicates that it is almost impossible to be cut by thermal shock but may be successfully cut by phase transformation mediated fracture.

A series of cutting experiments regarding different materials are performed and circled in Figure 2.6. Detailed results and analyses have been reported in publications [3, 4, 11-13]. Alumina, Zirconia and glasses are subjected to the group of thermal shock induced fracture, while PCBN, PCD and AlN are cut due to phase transition. The experiment results are consistent with the indices and processing map.

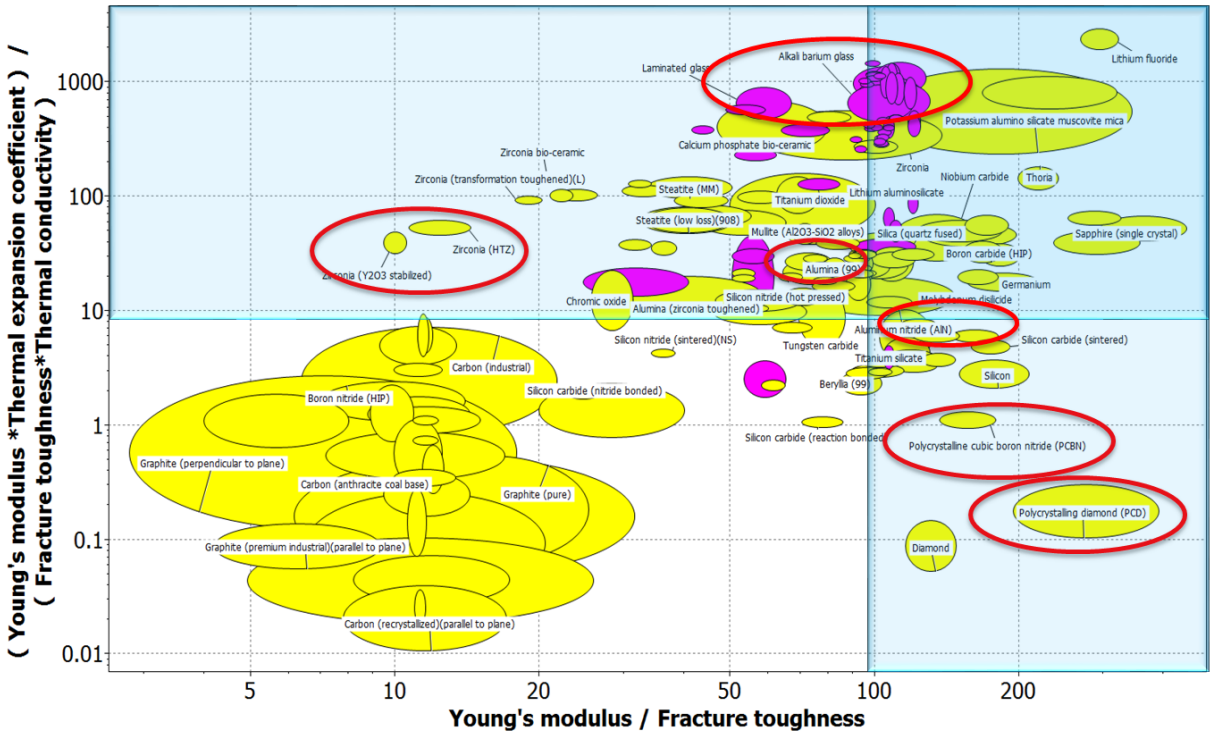

Figure 2.6. *Material selection map for cutting with thermal shock induced fracture and cutting with transformation expansion induced fracture*

From the process map and the cutting experimental results discussed above, we can essentially categorize materials into two groups. Materials with indice $\frac{E\alpha}{kK_{IC}} > 10$ are suitable

for machining by thermal shock, while materials with indice $\frac{E}{K_{IC}} > 100$ are suitable for machining by phase transformation. The materials lie at left and bottom part are not suitable to be cut by the LWJ machining method, while the materials lie at right and top may suitable for both mechanism.

2.4 Reference

[1] T. J. Lu and N. A. Fleck, "The thermal shock resistance of solids," *Acta Materialia*, vol. 46, pp. 4755-4768, Aug 10 1998.

[2] J. E. Moody and R. H. Hendel, "Temperature Profiles Induced by a Scanning Cw Laser-Beam," *Journal of Applied Physics*, vol. 53, pp. 4364-4371, 1982.

[3] D. Kalyanasundaram, P. Shrotriya, and P. Molian, "Fracture mechanics-based analysis for hybrid laser/waterjet (LWJ) machining of yttria-partially stabilized zirconia (Y-PSZ)," *International Journal of Machine Tools & Manufacture*, vol. 50, pp. 97-105, Jan 2010.

[4] D. Kalyanasundaram, P. Shrotriya, and P. Molian, "Obtaining a Relationship Between Process Parameters and Fracture Characteristics for Hybrid CO2 Laser⁄ Waterjet Machining of Ceramics," *Journal of Engineering Materials and Technology*, vol. 131, 2009.

[5] G. Davies and T. Evans, "Graphitization of Diamond at Zero Pressure and at a High-Pressure," *Proceedings of the Royal Society of London Series a-Mathematical and Physical Sciences*, vol. 328, pp. 413-&, 1972.

[6] F. P. Bundy, H. M. Strong, H. P. Bovenkerk, and R. H. Wentorf, "Diamond-Graphite Equilibrium Line from Growth and Graphitization of Diamond," *Journal of Chemical Physics,* vol. 35, pp. 383-&, 1961.

[7] J. Robertson, "Diamond-like amorphous carbon," *Materials Science & Engineering R-Reports,* vol. 37, pp. 129-281, May 24 2002.

[8] B. Galerkin, "Contribution to the general solution to the problem of the elasticity theory in the case of three dimensions.," *Comptes Rendus Hebdomadaires Des Seances De L Academie Des Sciences,* vol. 190, pp. 1047-1048, 1930.

[9] H. Y. Yu and S. C. Sanday, "Center of Dilatation and Thermal-Stresses in an Elastic Plate," *Proceedings of the Royal Society of London Series a-Mathematical Physical and Engineering Sciences,* vol. 438, pp. 103-112, Jul 8 1992.

[10] M. F. Ashby, *Materials Selection and Process in Mechanical Design, Fourth Edition*: Elsevier, 2010.

[11] Z. Wu, A. A. Melaibari, P. Molian, and P. Shrotriya, "The Mechanism Governing Cutting of Polycrystalline Cubic Boron Nitride (PCBN) with Transformation Induced Fracture," presented at the MSEC/NAMRC41 Madison, WI, 2013.

[12] D. Kalyanasundaram, G. Shehata, C. Neumann, P. Shrotriya, and P. Molian, "Design and validation of a hybrid laser/water-jet machining system for brittle materials," *Journal of Laser Applications,* vol. 20, pp. 127-134, May 2008.

[13] C. Barnes, P. Shrotriya, and P. Molian, "A HYBRID LASER/WATER-JET CUTTING PROCESS FOR BRITTLE MATERIALS," presented at the NAMRC 34, Milwaukee, Wisconsin, 2006.

CHAPTER III

HYBRID CO2 LASER/WATERJET (CO2-LWJ) CUTTING OF POLYCRYSTALLINE CUBIC BORON NITRIDE (PCBN) BLANKS WITH PHASE TRANSFORMATION INDUCED FRACTURE

Published in Optic & Laser Technology, Volume 70, 39-44, July 2015

Zhuoru Wu, Ammar Melaibari, Pal Molian and Pranav Shrotriya

Abstract

The present paper investigates a transformation induced fracture mechanism for the cutting of Polycrystalline Cubic Boron Nitride (PCBN) sample by a hybrid CO2 laser/waterjet (CO2-LWJ) manufacturing process. In CO2-LWJ machining, a laser was used for local heating followed by waterjet quenching leading to fracture propagation along the sample surface. Cutting results indicate that as line energy of the laser was increased the sample response transitioned from scribing to through cutting. Raman spectroscopy analysis of the cut surface indicates that laser heated PCBN undergoes chemical phase transformation from sp3-bonded cubic Boron Nitride (cBN) into hexagonal Boron Nitride (hBN) and other sp2-bonded phases. The sp2-bonded structure occupies more volume than sp3-bonded structure such that the transformed material has a tendency to expand the original material and leads to surface deformation around the cutting path. Surface profile of the cut samples were experimentally measured using profilometry and compared with numerical predictions in order to estimate the expansion strain and dimensions of transformation region. Based on the obtained expansion strain and transformation zone, stress fields and crack driving forces were computed for channeling cracks that result in material separation. Comparison of the crack driving forces

with fracture toughness of PCBN shows that transformation induced crack propagation is the feasible mechanism for cutting during CO2-LWJ machining.

KEYWORDS: Laser/waterjet machining (LWJ), cubic boron nitride, phase transformation, crack propagation.

3.1 Introduction

Cubic Boron Nitride (CBN) is the second hardest material on earth, inferior only to diamond. It is not found in nature but can be synthesized by application of high temperature and pressure [1]. Polycrystalline cubic boron nitride (PCBN) blank are produced through sintering of CBN powders with ceramic matrix such as titanium nitride (TiN) or aluminum nitride (AlN). Since its discovery, PCBN has been used in industry as a substitute for diamond due to the superior thermal and chemical stability. The advantages that PCBN does not react with ferrous metals and has a high resistance to oxidation[2] make it ideal tool material for machining hard cast iron, high chrome alloy steels, high-strength nickel super alloys, powder metal alloys and metal matrix composites [3].

CBN Tool inserts are traditionally cut from the compact blanks by either diamond sawing or electric discharge machining (EDM) or Nd:YAG laser cutting and finished by diamond grinding, lapping, and polishing. However, traditional manufacturing methods for producing tool inserts are slow and cost-inefficient due to the extreme hardness of PCBN materials. Given the limitations of conventional material removal mechanisms, a number of recent reports have focused on non-conventional mechanisms for machining of PCBN. Hidai and Tokura [4] investigated the hydrothermal-reaction assisted laser drilling of PCBN in steam

environment based on measurements of mass loss at high temperatures. Swiss Federal Institute of Technology in Lausanne, Switzerland has developed Laser-Microjet® [5], a hybrid technology based on waterjet-guided Nd:YAG laser for machining of PCBN. The Laser-Microjet® allows precise cutting of PCBN materials with smaller kerf and better surface finish but the process suffers from very slow cutting speeds as it reports 70 passes with each pass at a speed of 7 mm/min to cut 3.25 mm thick PCBN sample.

Crack propagation provides an energy and cost efficient method for cutting of ceramics because hardness and brittleness of ceramics lead to low material removal rates and slow cutting speeds during conventional machining processes. In low thermal conductivity ceramics such as alumina thermal shock induced fracture has been successfully utilized for energy efficient cutting [6, 7]. However in high thermal conductivity ceramics such as polycrystalline cubic boron nitride (PCBN), thermal shock may not be feasible. In this paper, we investigate fracture based material separation of PCBN due to synergistic interactions between laser heating and subsequent waterjet quenching. Cut surfaces were analyzed to identify chemical and phase changes of the PCBN due to LWJ machining. Height profiles of the machined PCBN samples were measured to determine the phase transformation induced deformation. Finite element analysis was used to estimate the stress fields associated with the deformation and predict the crack driving forces for channeling cracks that result in material separation in order to determine the mechanism governing material separation.

3.2 Experimental procedure

A continuous wave CO2 Laser (Model 820 Spectra Physics) of 10.6 μm wavelength and 1.5 kW rated power was used for all the cutting experiments. The laser head has been modified to accommodate the low-pressure waterjet (< 8 MPa (1000 Psi)) to realize CO2-LWJ machining. The modified laser head of the CO2-LWJ system is shown in Figure 3.1 and details of its design have been previously reported [6-8]. The laser head that incorporates the waterjet ensures that the workpiece is first irradiated with a CO2 laser beam for localized heating and subsequently, the heated spot is rapidly quenched with the trailing waterjet.

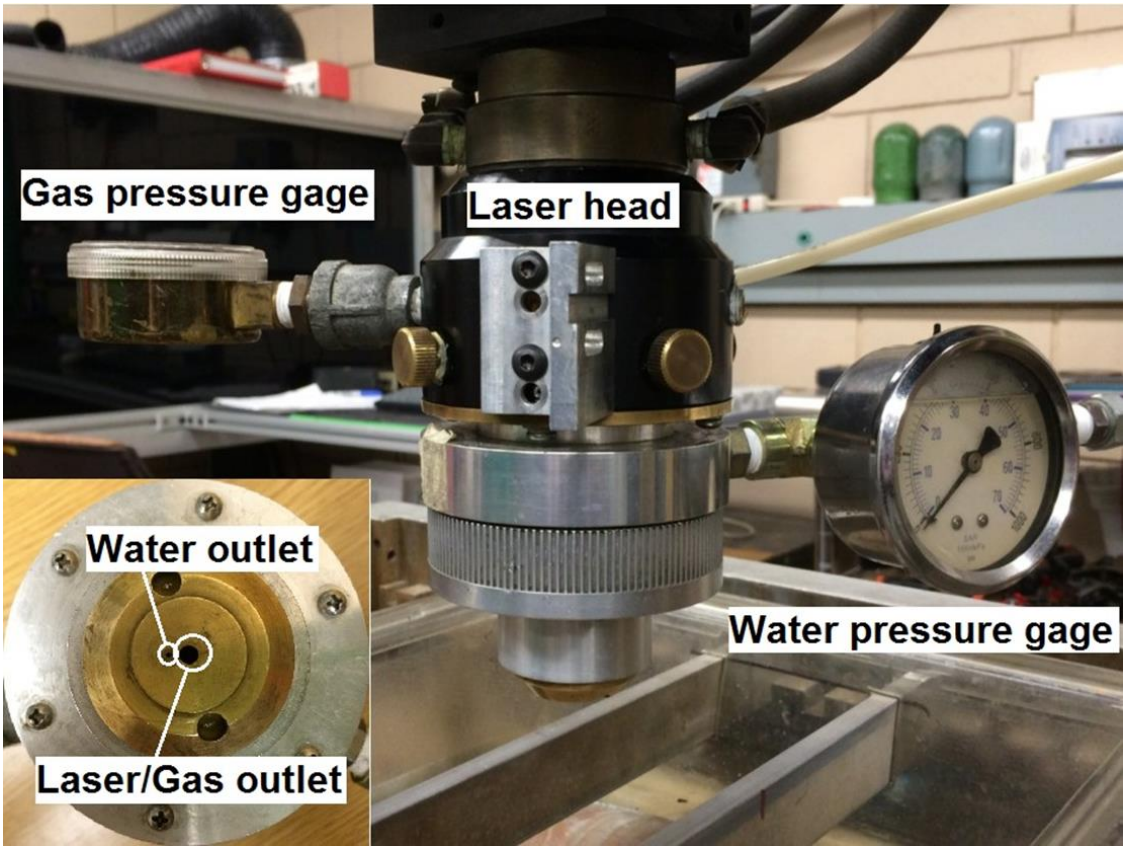

Figure 3.1. *Experiment setup of CO2-LWJ machining system*

Two different sets of experiments were carried out on the commercial Polycrystalline Cubic Boron Nitride (PCBN) tool samples (Diamond Innovations, Inc. (Worthington, Ohio)) that have a composition of 82% CBN (average particle size of 15 μm). The first set was

conducted to determine the effect of the laser line energy (ratio of laser power to cutting velocity) on fracture characteristics of PCBN samples; and the second set of experiments was conducted to characterize the surface deformation of samples associated with Laser/waterjet machining.

Triangular PCBN inserts (BZN 7000 series) with dimensions of 7mm side length and 1.6 mm thickness were used for the first set of experiments. The inserts had a surface roughness (Ra) of 0.3 μm on the polished faces and 3 μm on the side. Single-pass straight-line cutting experiments were carried out at the same laser power (P) of 500W but with three different cutting speeds (v) of 21.2 (50), 42.4 (100) and 63.5 (200) mm/sec (in/min) in order to investigate PCBN machining at line energies (P/v) of 23.6, 11.8, and 5.9 J/mm, respectively.

The second set of experiments was carried out on thick PCBN circular blanks (50 mm in diameter and 4.8mm in thickness) with same composition as the triangular inserts. Single-pass straight cutting experiments were carried out at a fixed laser power (P) of 800W with different cutting speeds to achieve line energies from 5.9 to 37.8 J/mm. The reason for using thick specimens was to ensure that samples does not undergo material separation and thus enable characterization of the surface deformation over the similar range of line energies as the first set of experiments.

In all the experiments, laser beam was focused on the sample surface to a spot size of 0.2 mm using a 127mm (5 in.) focal length lens. Pressure of water-jet was maintained at 5.5 MPa (800 psi) to apply rapid quenching on the heated region. Assist gas flow at a pressure of 69 kPa (10 psi) surrounding the laser beam was maintained during experiments to protect the lens from damage due to spatter. Payne et al. [9] have reported that water has very high absorption for CO2 laser energy and therefore , the laser/water-jet was designed such that the

water-jet trailed the laser beam with a spacing of approximately 2 mm in order to minimize absorption of laser power by direct contact with water.

Machined surfaces of the PCBN specimens were imaged by JEOL JSM-606LV Scanning Electron Microscope (SEM) at an acceleration voltage of 20 kV. Raman spectroscopy (Renishaw InVia Raman Microscope) with Ar-ion laser at a wavelength of 488nm was utilized to determine the PCBN phases in different regions of the transverse surfaces and the as-received samples. For the scribed thicker samples in the second set of experiment, surface profiles around each scribing line were measured using optical profilometer (Zygo NewView 7100) to characterize the surface deformation.

3.3 Numerical modeling

3.3.1 Finite element analysis for determination of transformation induced surface deformation

Boron nitride exits both in diamond-like sp3-bonded phases – cubic (cBN) or wurtzite (wBN) phases -- and graphite-like sp2 phases – hexagonal (hBN). The transformation between these phases may take place under high temperature or high pressure conditions [10] and is associated with volumetric changes [11]. During the cutting experiments, the laser irradiated sample surface may undergo a phase transformation from sp3 to sp2 bonded phases and induce volumetric expansion that may lead to deformation and development of stress field in the surrounding material. Finite element analysis was utilized to predict the stress fields and surface deformation of the sample due to the expansion of the transformed material.

The PCBN workpiece was modeled in finite element analysis package ABAQUS (Simulia, Providence, RI). A transformation zone undergoing uniform expansion was utilized

to model the influence of material transformation along the cutting path. Material properties of hBN were assigned to the transformation zone while material outside was modeled as PCBN. Cross-section of the transformation region was modeled as a semi-ellipse since laser intensity follows a Gaussian distribution. A schematic diagram of the workpiece indicating the transformed zone and cutting path is presented in Figure 3.2(a). The dimensions of the transformation zone in XZ plane (comparable to laser spot size ~ 0.1mm) are significantly smaller than the length along laser path (comparable to sample size ~ cm). Therefore plane strain state was applied to this model as shown in Figure 3.2(b) to obtain stress field in XZ plane. Given the symmetry of the sample, one half of the workpiece was analyzed with zero displacement in x direction (Ux=0) along the axis of symmetry. On outer edge of model, zero displacement in z direction (Uz=0) was applied to simulate the support of table during cutting. Mesh was refined to ensure that numerical results are independent of element size. Final refined mesh was composed of about 15000 quadratic elements with 8 nodes. Finally, the numerical predictions of surface deformation were compared to experimental measurements in order to estimate the transformation strain and dimensions of the transformed zone corresponding to the different line energies used in the CO2-LWJ cutting.

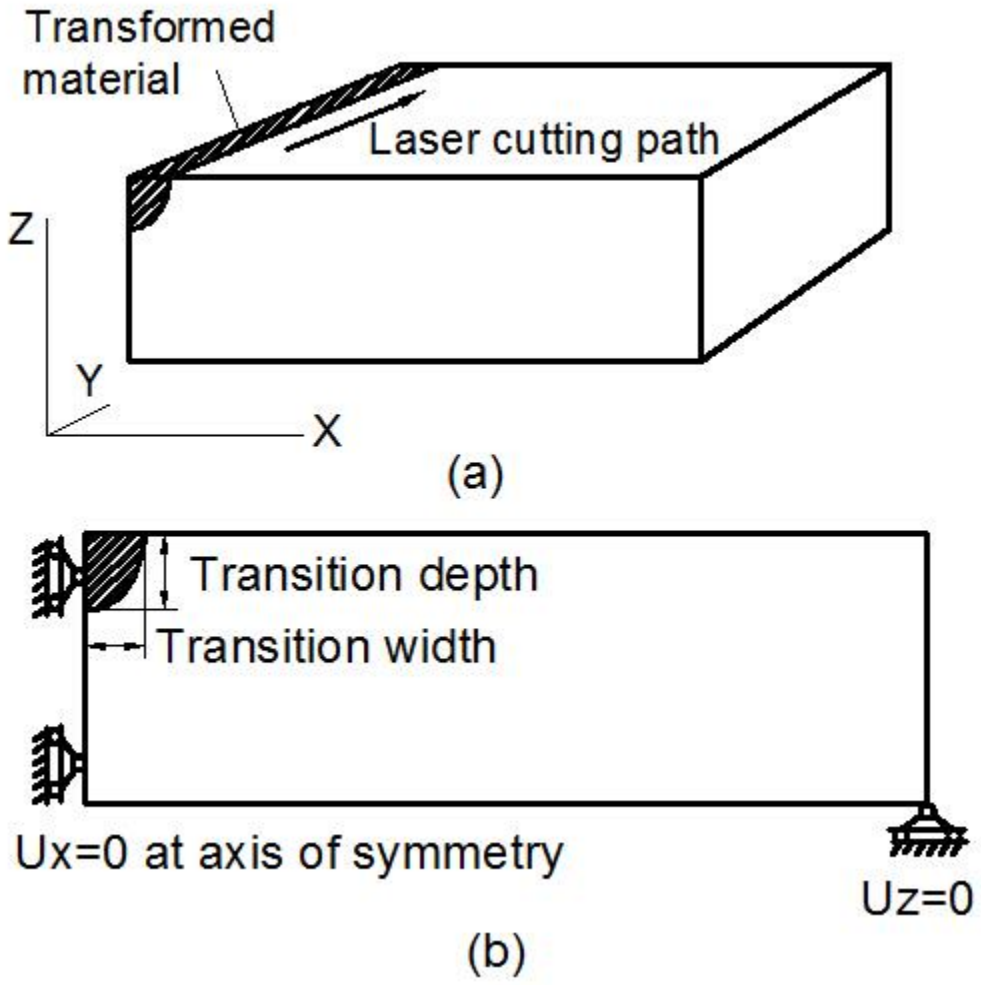

Figure 3.2. *(a) Schematic diagram of the workpiece machined by LWJ beam (b) Plane strain finite element model and boundary conditions for predicting sample deformation*

3.3.2 Fracture mechanics analysis of crack

Energy release rates for two different crack configurations – a plane strain crack along the thickness of the sample and channeling cracks along laser path, schematically shown in Figure 3.3 (a) and (b), respectively – were determined using the finite element analysis. The path independent J-integral [12-14] was computed to determine the energy release rate to characterize the crack propagation. Due to the extremely brittle nature of PCBN, the material response can be regarded as linear elastic such that J-integral equals energy release rate. Figure

3.4 shown the plane strain finite element model used to determine the J-integral values. The transformation zone size and expansion strain estimated from the deformation model were utilized to determine the energy release rate for crack propagation at different line energies. J-integral values were calculated for 10 contour layers around crack tip and achieved path-independence at out layers of elements. Energy release rates for plain strain cracks as a function of depths was obtained by modeling cracks of different depths starting below the transformation zone to the rest of whole thickness.

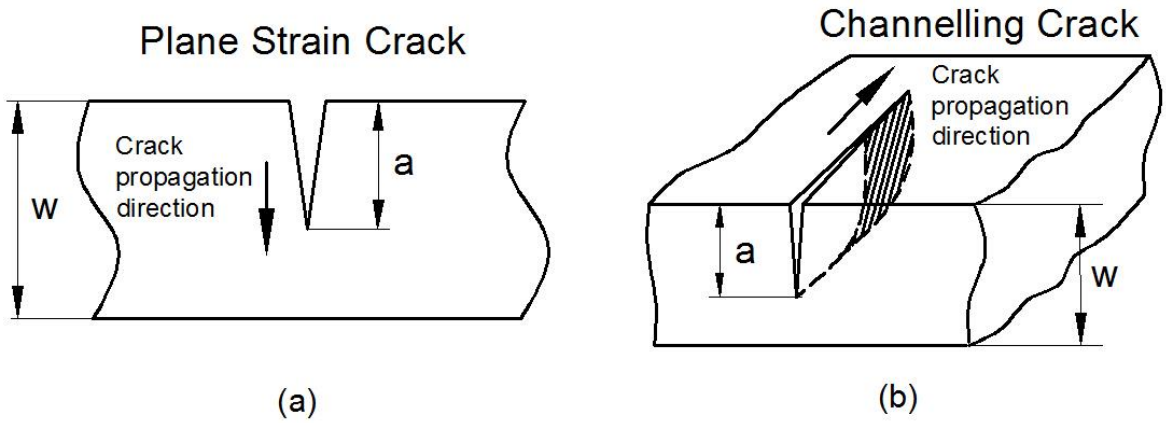

Figure 3.3. *Crack configurations: (a) Plain strain crack (b) Crack channeling*

Material separation along the cutting path can be treated as steady-state propagation of a channeling crack. Following Ho and Suo [15], energy release rate of channeling crack propagating with a constant tip shape at fixed depth (indicated by the shaded area in Fig 3.3(b)) was computed from the difference of energy stored in the configurations before and after crack advance. Consequently, the energy release rate for channeling cracks, $G_{\text{channeling}}$, for crack depth, a, was computed by integrating and averaging plain strain energy release rates, G_{plain}, over the crack depth:

$$G_{\text{channeling}} = \frac{1}{\text{a}} \int_0^{\text{a}} G_{\text{plain}}(\text{a}')\, \text{da}' \quad (3.1)$$

The channeling energy release rates were compared to the fracture toughness of PCBN to determine the feasibility of crack propagation along the cutting path due to CO2-LWJ induced transformation.

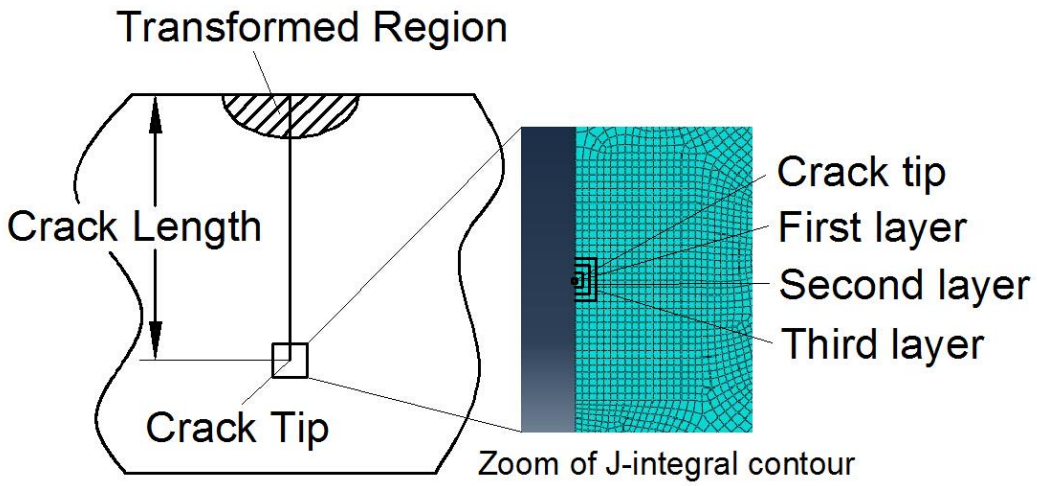

Figure 3.4. *Finite element model and crack tip mesh configuration for calculating energy release rate*

3.4 Result and discussion

3.4.1 Experimental results

For the first set of cutting experiments, observed fracture characteristics of the PCBN samples are summarized in Table 3.1. At the highest line energy (23.6J/mm), PCBN samples were separated with a through cut, indicating that the energy input was above the threshold value for through cutting. At the middle line energy (11.8J/mm), a straight groove was found along the cutting path. Subsequently, the cracked samples could be snapped by hand pressure with clean fracture surface and straight crack interface. The energy input at this level was at the threshold of through cutting over the thickness. At the lowest line energy (5.9J/mm), only

groove was observed on the sample surface. The grooved sample could not be separated on application of hand pressure after experiments.

Table 3.1. *Experimental cutting results of fracture behaviors at different line energies*

Line energy (J/mm)	5.9	11.8	23.6
Fracture characteristics	Groove only	Deep groove snapped by hand pressure	Cut through

The scribed sample was cut at line energy of 5.9 J/mm and the SEM image of the sample top surface is shown in Figure 3.5(a). Because of the rapid heat dissipation by water, narrow kerfs were produced and kerfs depth was found to be quite shallow. Recast layer inside the groove can be observed. No visible lateral cracks were generated during LWJ cutting and sputtered particles around the groove were insignificant. The transverse cross-section of the sample cut at line energy of 23.6 J/mm is shown in Figure 3.5(b). As shown in Figure 3.5(b), the cross-section of through-cut sample is divided into two different zones with different surface morphologies. Raman spectroscopy results of the two different zones are shown in Figure 3.6. The Raman spectrum of the top zone shows no cBN peak but two other peaks corresponding to different BN phases. The peak around 1370 cm-1 corresponds to hBN phases [16] while the peak around 1580-1590 cm-1 is reported to be a graphite-like sp2 B-C-N phases [17]. While the Raman spectrum of the lower zone away from laser irradiated surface was found to be similar to the as-received material with a peak at 1302 cm-1[18] corresponding to cBN phases. The SEM and Raman spectroscopy results showed that the top region near surface has undergone phase transformation as well as material ablation. This zone is labeled as the

transformation zone in the SEM image in Figure 3.5(b). While the bottom region has the same composition with the original material is labeled as the fracture zone.

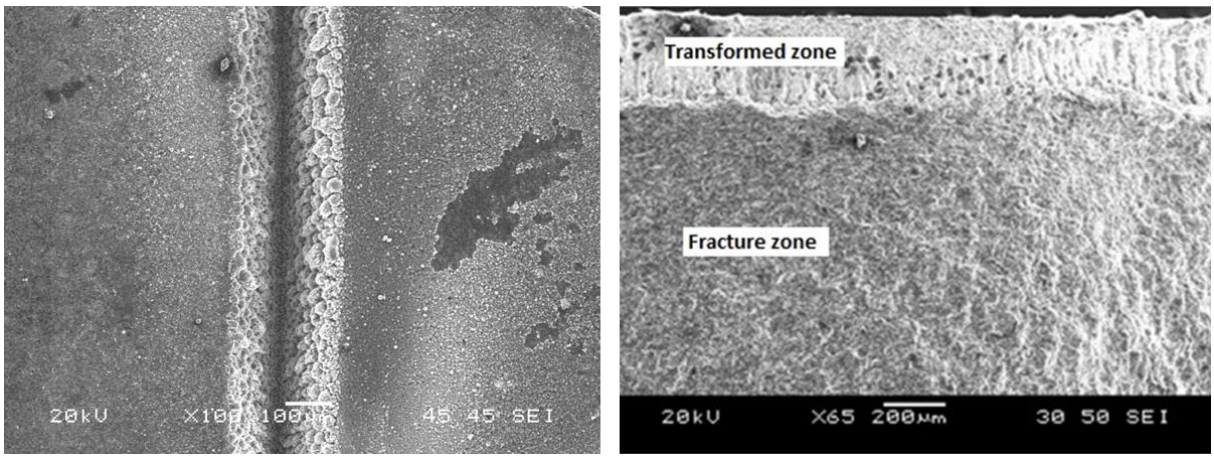

Figure 3.5. *SEM images of (a) Top view of scribed sample at line energy of 5.9kJ/m. (b) Fracture cross-section at line energy of 23.6kJ/m*

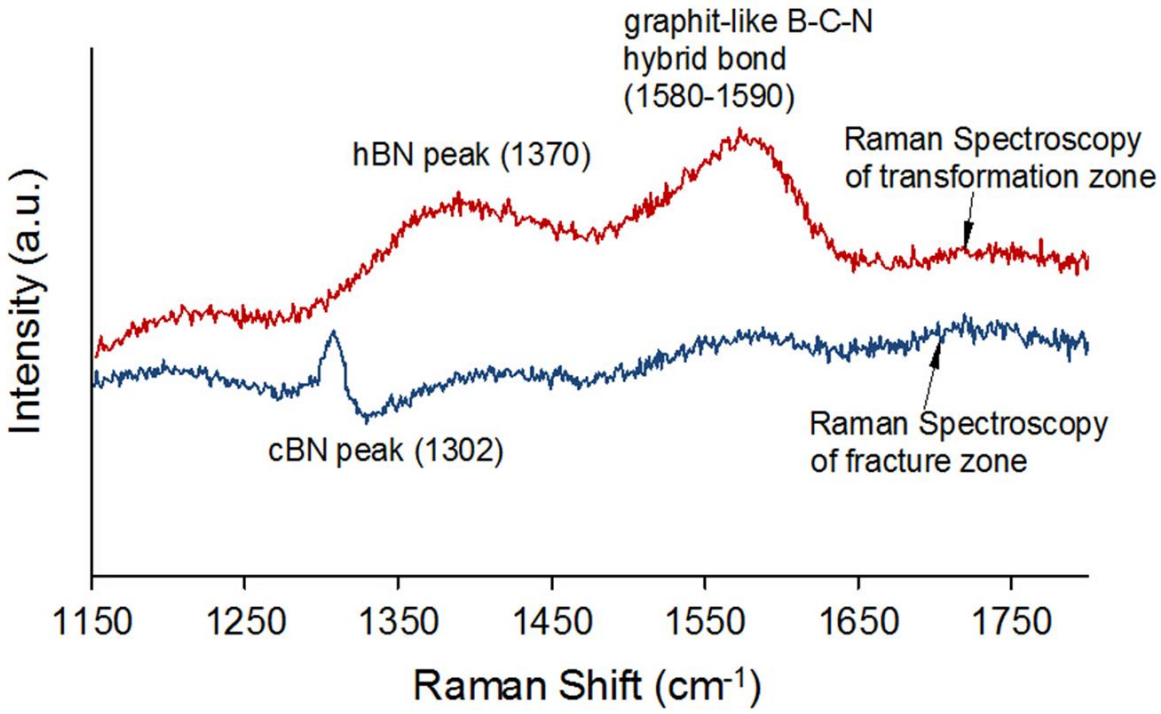

Figure 3.6. *Raman spectrum of transformed zone and fracture zone*

3.4.2 Surface deformation

In the second set of cutting experiments performed on the thicker cBN samples, only scribing was observed for all the three cutting parameters. Surface profile of the specimens adjacent to the kerf of each scribed cut were measured using optical profilometry and height distribution perpendicular to the scribed cut was averaged to determine the representative surface deformation. The surface profiles were found to be nearly symmetric about the cut center and averaged value of the two sides are plotted in Figure 3.7 along with error bars for the three line energies. The error bars are equal to one standard deviation of the measured height values and represent the variations in the surface profile along the cut direction. The kerf widths of the three scribing lines were found to be roughly the same as the laser beam diameter of 0.2 mm. For all three line energies, surface deformation is highest near the kerf and decays monotonically with distance from the scribed cut. The magnitude of surface deformation is dependent on line energy and is found to increase as the line energies are increased.

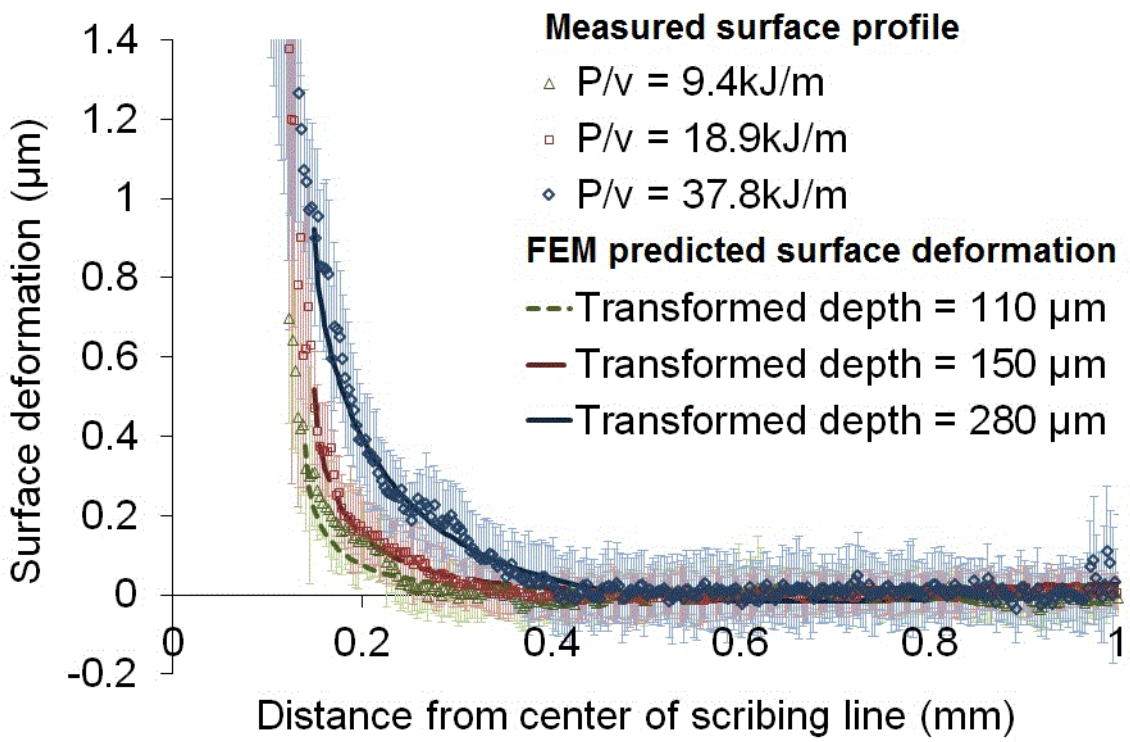

Figure 3.7. *Comparison of measured surface deformation with FEM model prediction. Measured surface profile including error bars of first standard deviation were presented in the data*

3.4.3 Numerical modeling of laser cutting induced phase transformation

The experimental observations suggest that the material separation during the cutting experiments is through a "score and snap" mechanism: (1) laser irradiation led to scribing as well as heating and transformation of the material from sp3-bonded cBN to sp2-bonded BN phases in the transformation zone along the cutting path [10]; (2) the constrained volumetric expansion of the material in transformation resulted in deformation and development of stress field in the material surrounding the transformation zone; (3) The transformation induced stress fields lead to propagation of cracks formed during scribing that result in the material separation. In order to validate the "score and snap" mechanism, numerical modeling is

utilized to determine if the scribed initial cracks can propagate through the thickness under transformation induced stress field. The numerical modelling is performed in two steps: firstly, FEA deformation models are used to predict the surface deformation of thick specimens. The numerical predictions are compared to experimentally measurements to estimate the transformation zone size and expansion strains as a function of line energy. In the second step, the estimated transformation zone size and expansion strains are utilized in the FEA fracture models of thin specimen with different crack depths to determine the energy release rates as a function of crack depth. Finally, the computed energy release rates are compared to the fracture toughness of PCBN in order to determine the propensity of crack propagation under different line energies.

Numerical predictions of surface deformation that best describe the measured surface deformation are also plotted as smooth lines in Figure 3.7. The numerical results for all the laser line energies corresponded to a constant expansion strain of 1.3% and transformation zone width of 0.15mm. The width of transformation zone was assumed to be constant based on the observation of similar kerf widths for all the line energies. Depths of transformation zone depend on laser line energy and were found to follow a linear relationship that is plotted in Figure 8.

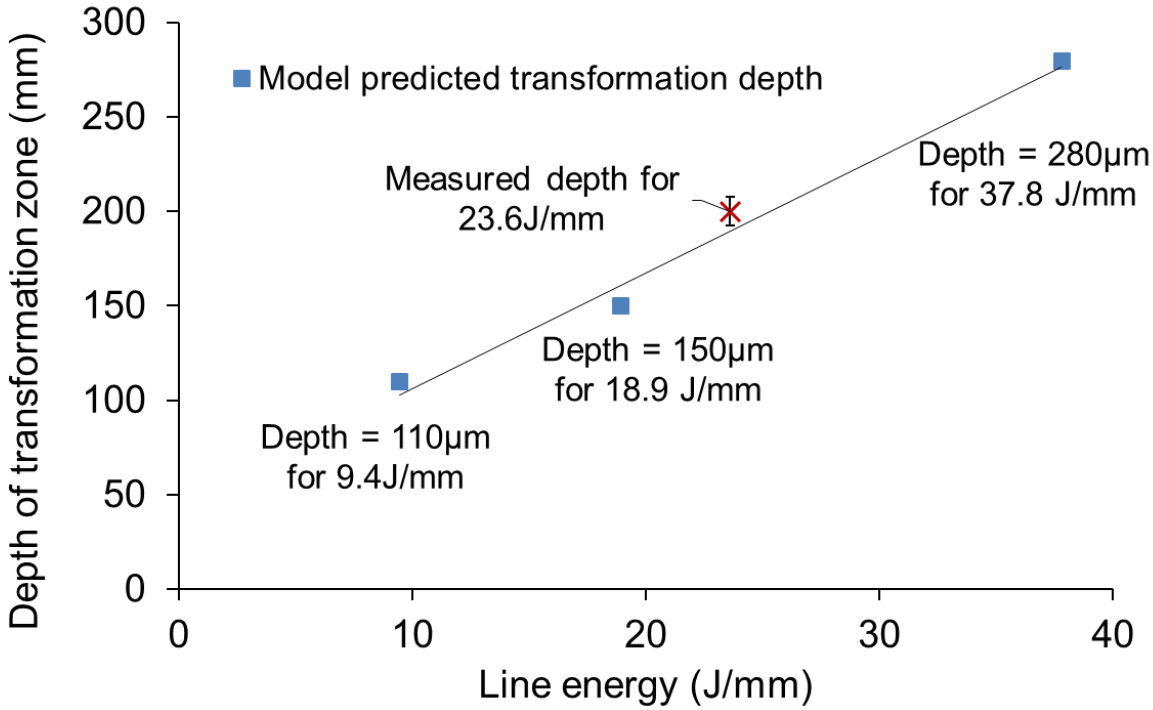

Figure 3.8. *Relationship between line energy and depth of transformation zone*

The linear relationship between line energy values and depth of transformation zone can also be used to approximate the transformation depth for PCBN specimens of 1.6 mm that were used in the first set of cutting experiments. On the through-cut specimen cut with line energy of 23.6J/mm, depth of transformed zone measured from transverse SEM image (see Figure 5(b)) is plotted in Figure 3.8.

Two different numerical predictions of the finite element model - surface deformation and transformation depth - were compared to experimental results from two independent sets of experiments. Good agreement between the measured and predicted response in both cases indicates that numerical model can describe the transformation induced deformation and consequently relate the LWJ cutting parameters (line energy) to the size of the transformation depth and expansion strain. The small discrepancy between them may come from inaccurate

modeling assumptions. The assumption of constant expansion stain and constant width of transformation zone is probably the main source for the discrepancy.

3.4.4 Fracture energy results and crack behavior prediction

In the first set of experiments, laser radiation is initially incident over the specimen boundary resulting in damage across the whole thickness and therefore, equilibrium depth of a channeling crack is most appropriate for approximating the CO2-LWJ induced cut depth in the specimens. In order to compute the energy release rates for channeling cracks, FEA fracture model shown in Figure 3.4 was first utilized to predict the plane strain energy release rate of the PCBN specimen. In this model, the transformation zone depth was estimated using the linear relationship obtained in Figure 3.8 for each line energy. The transformation zone width and expansion strain were kept 0.15 mm and 1.3% as found from the deformation model. Finally, the computed energy release rates for plain strain cracks were used in equation (1) to determine the energy release rates for channeling cracks as a function of the crack depth.

The energy release rates corresponding to the three line energies used in cutting experiments are plotted as function of channeling crack depth in Figure 3.9. Energy release rates reach the highest for cracks that are approximately twice the depth of the initial crack due to the large tensile stresses outside the transformation region induced from material expansion. Critical energy release rates (Gcritical) range based on reported fracture toughness of BZN7000 as 7.7-10 MPa$\sqrt{m}$ [19] was also plotted in Figure 3.9 in order to explain the fracture characteristics observed in the cutting experiments. Channeling energy release rates for all crack depths corresponding to line energy of 5.9J/mm are lower than the critical range suggesting that under this processing condition laser irradiation induced damage results in scribing of samples and the transformation induced stress field is not sufficient to propagate

the channeling cracks. Channeling energy release rates corresponding to cutting line energy of 11.8J/mm lies right between the critical range, indicating that this processing condition is threshold for transition between scribing cuts to through the thickness cuts. Channeling energy release rates at all crack depths for the highest cutting line energy of 23.6J/mm is higher than Gcritical suggesting that cracks are expected to propagate along the laser path through the whole thickness. The numerical prediction based on comparison between computed energy release rates with Gcritical agrees well with fracture characteristics observed in the cutting experiments.

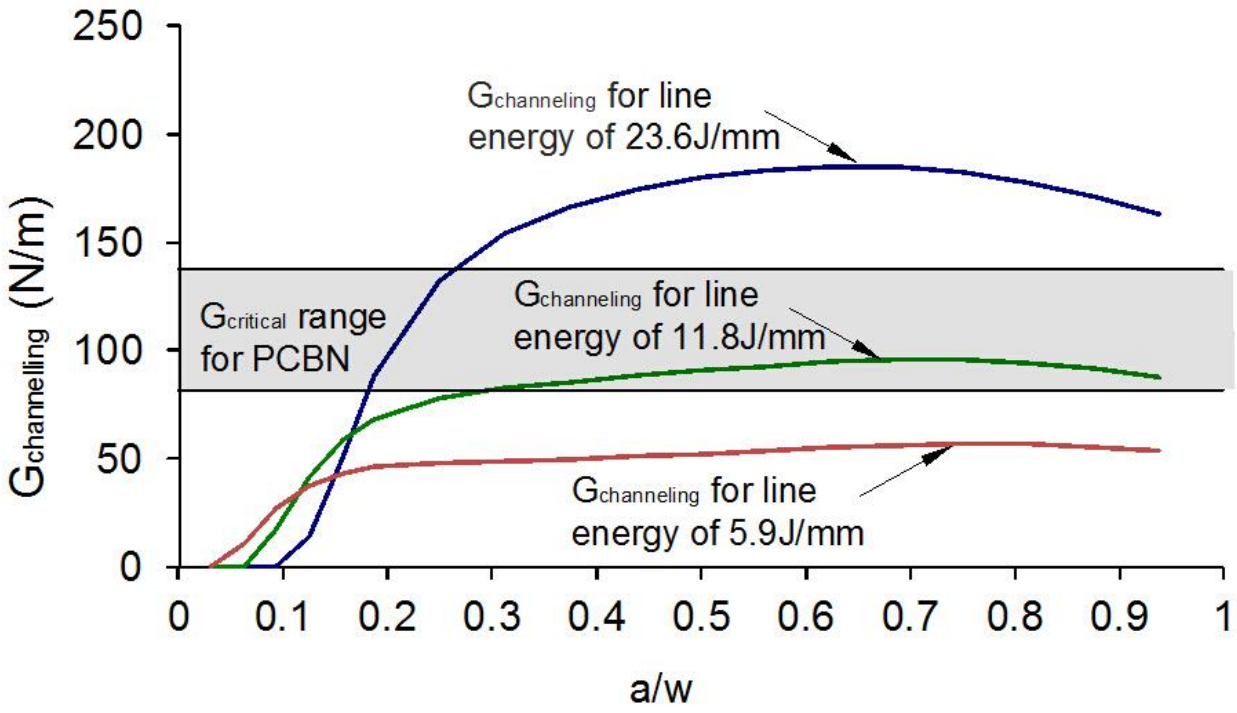

Figure 3.9. *Energy release rate for channeling crack*

Results of numerical modeling based on "score and snap" cutting mechanism for material separation are able to describe the experimentally observed transition from scribing to through-cut of PCBN specimens. Our assumptions of uniform expansion strain associated

with PCBN transformation and shape of transformation zones are simplistic but can adequately describe the mechanism governing material separation. The numerical model may be used to determine the line energy values required for scribing and through cutting of PCBN specimen with different thicknesses and different geometries.

3.5 Conclusion

The hybrid CO2-LWJ machining system is used for cutting experiments on two different thicknesses of PCBN blank samples in order to study the effect of processing parameters on the fracture behaviors and to estimate the size of phase transformed zone as well as associated expansion strain. Three different fracture behaviors were observed in cutting experiments on thinner PCBN blanks indicating a transition from scribing to through-cut at threshold value of laser line energy. Surface analyses of the cut samples indicate that laser-heated PCBN undergoes phase transformation. Based on the experimental observations, a "score and snap" cutting mechanism is proposed for material separation. Laser irradiation of the sample surface leads to scoring and phase transformation of the PCBN from sp3 to sp2 hybridized BN phases along the cutting direction. Constrained volumetric expansion of transformed material leads to development of tensile stresses in the surrounding material and propagation of laser-scored cracks along the thickness. Finite element modeling of the transformation induced surface deformation and energy release rates for cracks is utilized to validate the "score and snap" mechanism for PCBN cutting. Numerical modeling of the transformation induced surface deformation indicates that transformation zone depth increases linearly with laser line energy used for cutting and volumetric changes associated with transformation may be modeled using an uniform volumetric expansion strain. Comparison

of the computed energy release rate for channeling cracks with reported values of PCBN fracture toughness indicate that "score and snap" cutting mechanism describes the experimental observations. These results suggest that controlled crack propagation is an efficient mechanism for separation of PCBN materials.

3.6 Acknowledgement

The authors would like to gratefully acknowledge the financial support provided by the US National Science Foundation under the grant CMMI -1000035. The authors would also like to thank Diamond Innovations, Inc. (Worthington, OH) for providing the Polycrystalline Cubic Boron Nitride samples.

3.7 References

[1] R. H. Wentorf, "Synthesis of Cubic Form of Boron Nitride," *Journal of Chemical Physics*, vol. 34, pp. 809-&, 1961.

[2] P. B. Mirkarimi, K. F. McCarty, and D. L. Medlin, "Review of advances in cubic boron nitride film synthesis," *Materials Science & Engineering R-Reports*, vol. 21, pp. 47-100, Dec 15 1997.

[3] C. C. White, M. R. VanLandingham, P. L. Drzal, N. K. Chang, and S. H. Chang, "Viscoelastic characterization of polymers using instrumented indentation. II. Dynamic testing," *Journal of Polymer Science Part B: Polymer Physics*, vol. 43, pp. 1812-1824, 2005.

[4] H. Hidai and H. Tokura, "Hydrothermal-reaction-assisted laser machining of cubic boron nitride," *Journal of the American Ceramic Society*, vol. 89, pp. 1621-1623, May 2006.

[5] O. D. Sibailly, F. R. Wagner, L. Mayor, and B. Richerzhagen, "High precision laser processing of sensitive materials by Microjet," in *Fourth International Symposium on Laser Precision Microfabrication*, 2003, pp. 501-504.

[6] D. Kalyanasundaram, G. Shehata, C. Neumann, P. Shrotriya, and P. Molian, "Design and validation of a hybrid laser/water-jet machining system for brittle materials," *Journal of Laser Applications,* vol. 20, pp. 127-134, May 2008.

[7] D. Kalyanasundaram, P. Shrotriya, and P. Molian, "Obtaining a relationship between Process parameters and Fracture energy for CO2 Laser/Waterjet Machining of Ceramics," *Journal of Engineering Materials and Technology*, vol. 131, pp. 011005-10, 2009.

[8] C. Barnes, P. Shrotriya, and P. Molian, "Water-assisted laser thermal shock machining of alumina," *International Journal of Machine Tools & Manufacture,* vol. 47, pp. 1864-1874, Oct 2007.

[9] B. P. Payne, N. S. Nishioka, B. B. Mikic, and V. Venugopalan, "Comparison of pulsed CO2 laser ablation at 10.6 mu m and 9.5 mu m," *Lasers in Surgery and Medicine,* vol. 23, pp. 1-6, 1998.

[10] H. Sachdev, R. Haubner, H. Noth, and B. Lux, "Investigation of the cBN/h-BN phase transformation at normal pressure," *Diamond and Related Materials,* vol. 6, pp. 286-292, Mar 1997.

[11] J. Robertson, "Diamond-like amorphous carbon," *Materials Science & Engineering R-Reports,* vol. 37, pp. 129-281, May 24 2002.

[12] H. F. Bueckner, "A Novel Principle for Computation of Stress Intensity Factors," *Zeitschrift Fur Angewandte Mathematik Und Mechanik,* vol. 50, pp. 529-&, 1970.

[13] J. R. Rice, "A Path Independent Integral and Approximate Analysis of Strain Concentration by Notches and Cracks," *Journal of Applied Mechanics,* vol. 35, pp. 379-+, 1968.

[14] T. L. Anderson, *Fracture mechanics: fundamentals and applications*: CRC press, 2005.

[15] S. Ho and Z. Suo, "Tunneling Cracks in Constrained Layers," *Journal of Applied Mechanics-Transactions of the Asme,* vol. 60, pp. 890-894, Dec 1993.

[16] L. Song, L. J. Ci, H. Lu, P. B. Sorokin, C. H. Jin, J. Ni, *et al.*, "Large Scale Growth and Characterization of Atomic Hexagonal Boron Nitride Layers," *Nano Letters,* vol. 10, pp. 3209-3215, Aug 2010.

[17] M. A. Mannan, H. Noguchi, T. Kida, M. Nagano, N. Hirao, and Y. Baba, "Growth and characterization of stoichiometric BCN films on highly oriented pyrolytic graphite by radiofrequency plasma enhanced chemical vapor deposition," *Thin Solid Films,* vol. 518, pp. 4163-4169, May 31 2010.

[18] H. Sachdev, "Influence of impurities on the morphology and Raman spectra of cubic boron nitride," *Diamond and Related Materials,* vol. 12, pp. 1275-1286, Aug 2003.

[19] M. P. DEvelyn and K. Zgonc, "Elastic properties of polycrystalline cubic boron nitride and diamond by dynamic resonance measurements," *Diamond and Related Materials,* vol. 6, pp. 812-816, Apr 1997.

CHAPTER IV

CONTROLLED CRACK PROPAGATION BASED LASER/WATER-JET (LWJ) MACHINING OF TUNGSTEN CARBIDE SUPPORTED POLYCRYSTALLINE CUBIC BORON NITRIDE TOOL MATERIAL (PCBN-WC)

Zhuoru Wu, Ammar Melaibari, Pal Molian and Pranav Shrotriya

Abstract

This paper investigated a novel thermochemical material cutting mechanism through controlled crack propagation of the Tungsten Carbide supported Polycrystalline Cubic Boron Nitride (PCBN-WC) substrates with Laser/Waterjet(LWJ) machining system. The LWJ system integrates a high power CO2 laser beam with a low pressure waterjet to apply rapid heating and quenching that achieved fracture initiation and propagation along the machining path. Material separation in the workpiece is achieved in two steps:(1)a single-pass LWJ cutting with focused laser beam is used to create an initial groove on the sample surface and (2) subsequently, multiple passes with defocused laser beam are then applied to propagate a single crack through the work piece. Surface deformation, morphology and phase compositions were characterized on the cut sample using profilometry, scanning electron microscopy and Raman spectroscopy in order to identify the mechanism underlying the material separation. A finite element model was developed to predict the surface deformation and compared with surface profiling measured using optical profilometry to estimate the expansion strain and dimensions of phase transformed region. Fracture mechanics analysis based on the obtained expansion strain and transformed zone was performed to predict crack configurations and validate with experimental cutting results. Based on comparison between experimental observations and model predictions, a “score and snap” mechanism is identified for WC/cBN

tool cutting : (1) The first cutting pass with a focused laser beam results in scoring the sample through localized laser heating and subsequent waterjet quenching transformed PCBN near the top surface from sp3-bonded phase into sp2-bonded phases leading to volumetric expansion induced tensile stress development in the surrounding material; (2) Subsequently, multiple passes of defocused beam enlarged the transformed material zone that progressively drove the crack through WC layer leading to material separation.

KEYWORDS: Laser/waterjet machining (LWJ), defocused laser machining, PCBN, controlled fracture, phase transformation

4.1 Introduction

Cubic Boron Nitride (CBN) is the second hardest material on earth, and is a difficult-to-machine ceramic material due to its ultra-high hardness. PCBN has been used in industry as a substitute for diamond due to the superior thermal and chemical stability. The advantages that PCBN does not react with ferrous metals and has a high resistance to oxidation[1] makes it an ideal tool material for machining hard cast iron, high chrome alloy steels, high-strength nickel super alloys, powder metal alloys and metal matrix composites[2]. PCBN tool blanks consists of fine crystals are sintered under the conditions of high temperature and pressure with metallic (Co) or other binders. The common used binder phases includes nickel [3], magnesium carbonate [4, 5] and ceramics (AlN and TiN). Similar to carbon, boron nitride exits both diamond-like sp3 bonded phases(cBN and wBN) and graphite-like sp2 phases (hBN and rBN) and transformation between these phases would happen under high temperature or high pressure[6]. It was reported that the sp2-bonded structure occupies much more volume than

sp3-bonded structure[7], therefore transformed material has an tendency to expand the original material.

PCBN tools are usually available in two forms: a solid compact or a composite with tungsten carbide substrate. While PCBN offers high wear resistance during machining, carbide substrates offer the required toughness as well as low cost making the composite tools an ideal choice for manufacturers. PCBN blanks in the thickness range 1.6 mm to 4.8 mm are available to making inserts in the form of rounds, squares, diamonds, and triangles designed to fit special usage in different industries.

Due to the extreme hardness, it is difficult to machine the PCBN tool blanks. During tool production, speed is an important criterion as cutting hard materials can be time-consuming. Typical speed is on the order of few mm per minute. Many processes have been vigorously studied but none has the combination of speed, resolution and cost-effectiveness desired for industrial productivity. Current manufacturing methods for producing tool inserts in PCBN are diamond saw, wire-EDM and Nd:YAG laser cutting which are slow and less precise. Diamond saw is not acceptable due to rapid tool wear and slowness of the process. In addition, small kerfs are difficult to produce due to blade thickness. Electric discharge machining (EDM) [8, 9] and electric discharge grinding (EDG)[3, 10] of PCD are constrained by high machining cost, slowness and low efficiency. EDM cannot be used if the compact is not electrically conductive (example: PCBN with AlN binder). Conventional Nd:YAG laser cutting suffers from particle formation (due to vaporization) and thermal damages, conical kerfs and post processing becomes essential. Water jet-guided laser technology[11] - also known as Laser MicroJet® developed by researchers in Swiss Federal Institute of Technology was an innovative technology that allows precise cutting of PCBN materials with smaller kerf

and good surface finish. The concept of this technology is to focus a laser beam into a nozzle while passing through a pressurized water chamber. The free laminar waterjet is used as an optical waveguide to direct the Nd:YAG laser beam onto the sample. A Q-switched pulse laser (up to 300 W) of 532 nm wavelength and water pressure of 2-10 MPa was employed for the process. The waterjet permitted parallel beam transmission through the sample leading to taper-free and narrow kerf features. The tolerances are much smaller than those obtained with conventional laser and EDM processes. However the process suffers from very slow cutting speeds as it reports 120 passes with each pass at a speed of 25mm/s were needed to cut 1.6mm WC supported PCBN sample[11].

Given to the limitation of existing machining method of PCBN, a novel process of combining continuous wave CO2 laser and water-jet (LWJ) was developed by our group to improve the machining efficiency and quality of PCBN [4]. The CO2-LWJ machining system implemented a high power laser heating followed by low pressure waterjet quenching that achieved fracture initiation and controlled propagation along the cutting path. Experiments on 1.6 mm thick solid PCBN (BZN 7000) supplied by Diamond Innovation Inc. showed that cutting speeds up to 42.3 mm/s could be readily achieved in single pass. Results have been summarized in chapter 1. The advantages of our CO2-LWJ over traditional Nd:YAG laser are finer kerf (crack width of few μm), parallel surfaces and minimal recast layer/HAZ and almost two orders of magnitude faster cutting speeds.

Tsai and Chen[12] reported a laser cutting technique by controlled fracture used for the cutting of thick ceramic substrates by applying a focused Nd:YAG laser followed by a defocused CO2 laser. It successfully achieved the through cutting of thick alumina substrate along the moving path of the laser beams with a neat interface. Due to the observation of lateral

cracks and surface damages generated in LWJ cutting with focused beam, a similar technique combining single-pass focused beam and multi-passes defocused beam was applied aiming to reduce the uncontrolled lateral cracks.

4.2 Experimental details

4.2.1 PCBN/WC sample cutting experiments and sample characterization

A continuous wave CO2 laser (Model 820 Spectra Physics) of 10.6 μm wavelength was used in all the experiments. Cutting samples were mounted on a positioning workstation that controlled by a 2D CNC system. The beam from the laser was sent through a 127 mm focusing lens and irradiated on the sample surface to a focal spot diameter of 0.2 mm. A defocused spot can be achieved through adjusting the distance between laser head and sample surface. The waterjet trailed the laser beam on the sample surface with a spacing of 2mm between them. A constant water pressure of 0.4Mpa (60 psi) was maintained in all the experiments. Laser beam was surrounded by air with a pressure of 35kPa (5 psi) in order to prevent direct interaction of laser and waterjet. During the experiments, laser beam was irradiated outside the sample, translated through and stopped out of the other side.

The sample for cutting experiments is a double-layer WC supported PCBN blank, provided by Diamond Innovations, Inc. (Worthington, Ohio). The blank was 1.6mm thick wafer with 1mm thick PCBN sintered on 0.6 mm thick WC. The composition of PCBN was 50% with binder phase of 45% TiN and 5% AlN. Single-pass straight-line cutting with focused laser beam of 0.2mm was first performed to create an initial groove; 4 passes of defocused beam with spotsize of 0.5mm were followed to make the existing crack propagates through the

whole specimen. The processing parameters of power and speed were maintained at 400W and 42.32 mm/s (100 inch/min).

Scanning electron microscopy (SEM Model JEOL JSM-606LV at 20 kV) was used to inspect the cutting quality and characterize cutting features. An optical microscope (Nikon) was used to measure the groove depth with a resolution of 1 μm. Raman spectroscopy (Renishaw-inVia Raman Microscopy) with Ar-ion laser at a wavelength of 488nm was utilized to identify the material phases present in the transverse cut surfaces and as-received samples.

4.2.2 Defocused beam study and surface deformation measurement

In order to understand the mechanism and advantages of defocused LWJ beam, another set of experiments was carried out that different numbers of defocused passes were applied after the initial focused groove for learning the progressive effect of the defocused beam. Same power and speed (400W and 100in/min) were implemented as in the first set of experiments. Four cuttings were carried out on a 4.8mm thick PCBN sample with 1, 2, 4 and 8 passes of 0.5mm defocused LWJ beam following the initial groove produced with 0.2mm focused beam. The reason using 4.8mm thick sample was to ensure that samples does not undergo through-cut and thus enable characterization of the surface deformation.

3D topographies adjacent to the kerf along each scribed cut were measured using an optical profilometry (Zygo NewView 7100). Height distribution along the cut was averaged to a line normal to the cutting path and data on both sides of the cut center was averaged to one side that represented surface deformation of LWJ machining. The surface deformation was compared with finite element modelling predictions for validating the expected cutting mechanism.

4.3 Numerical modeling

4.3.1 Finite element analysis of phase transition induced surface deformation

In order to study the cutting mechanism of the combined focused and defocused beam, finite element models are developed to predict the surface deformation induced by different numbers of defocused paths. Phase transition of boron nitride can take place at high temperature from diamond-like sp3-bonded cubic(cBN) phase to graphite-like sp2-bonded hexagonal (hBN) phase[6, 13] and is associated with an increase of volume change [7]. A uniformly expanded inclusion was utilized to model the influence of material transition along the cutting path. Material inside the transition zone was assigned to the properties of hBN while material outside was maintained as PCBN and WC. The detailed material properties are summarized in Table 1. The model was simplified to 2D plane strain state of a transverse cross-section of workpiece and only half of it was analyzed with fixed boundary condition on the axis of symmetry. For each cut with different numbers of defocused passes, the shape and dimensions of the transformed zone were modelled based on the fitting of FEA computed surface deformation with the experimental measured surface profile. The constant expansion strain of transition zone was also determined from the best fitting result.

4.3.2 Fracture mechanics analysis of cracks

Fracture mechanics analysis was performed to determine the crack propagation behavior for the first set of cutting experiment of PCBN-WC specimen. Laser irradiation heated the surface and caused localized damages that resulted in crack nucleation and propagation. At the beginning of each cut, a crack was initiated across the edge of the specimen. As the laser beam moved in, the existing crack extended towards center of the plate following the LWJ path that achieved separation of the material. Besides the controlled fracture, some

micro cracks might generate and develop into uncontrolled lateral cracks that spall the materials around the cut region. Figure 4.1 shows the three crack configurations in the schematic plot of LWJ machining system.

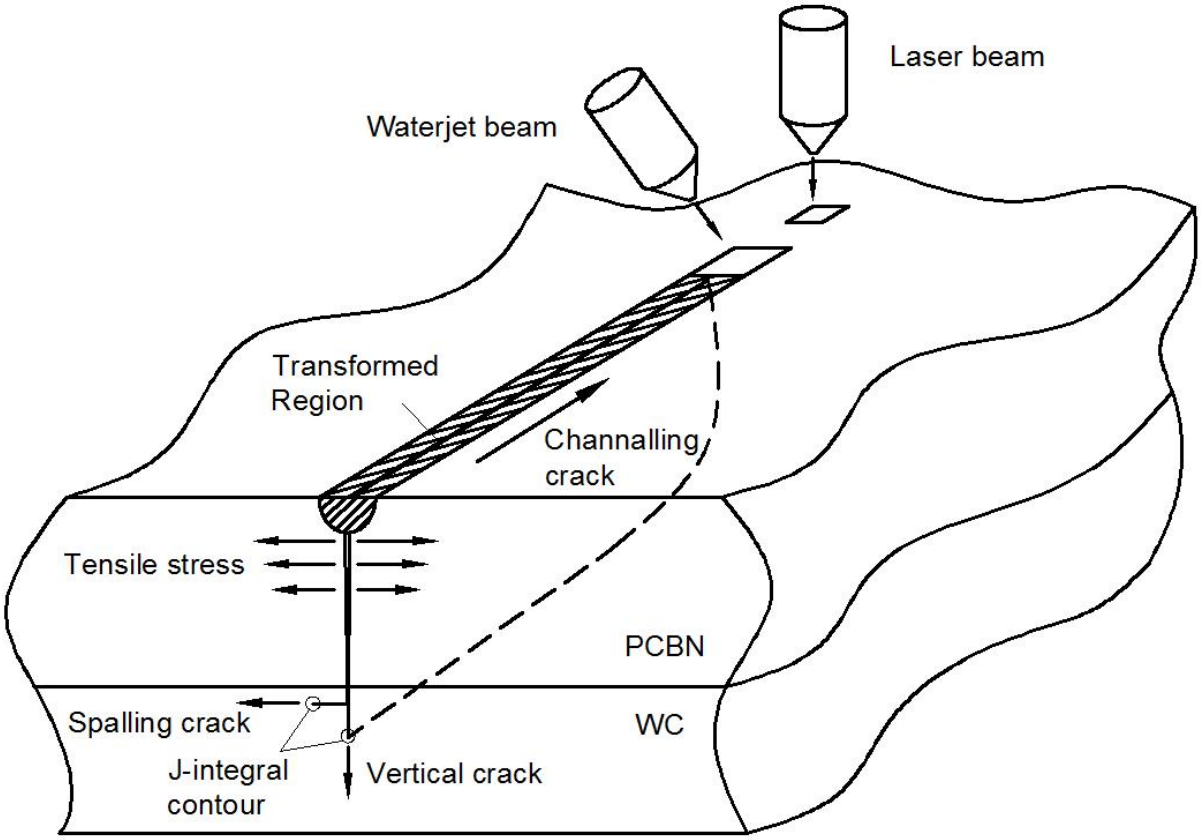

Figure 4.1. *Crack propagation mechanism*

2D plane strain analysis was used to model the lateral crack and vertical crack initiated at sample edge with different crack lengths. J-integral evaluation was utilized to calculate energy release rate that characterize the crack behavior. In 2D plane strain vertical crack model, the crack length was assigned from a small initial value to the rest of whole thickness such that the function of energy release rate verses crack length throughout the thickness can be obtained. Lateral cracks were assumed to start from the vertical crack below the transformation zone and were assigned to a very small initial value and an initial direction parallel to the sample surface.

In this paper, only the initiation of lateral cracks was investigated while the propagation is not in the scope of discussion. It is worthy to notice that the J-integral domain is not allowed to across the interface between inhomogeneous materials. Therefore the crack tip contour were chosen to be very close to the interface without crossing the boundary. In such way, a narrow gap would appear in the plane strain energy curve but would not affect the integration in getting channeling fracture energy.

The existing vertical plane strain crack channeled along the LWJ path based on the assumption that the fixed depth and constant tip shape was maintained during the crack propagation. Gchanneling, can be determined from the integration of plain strain energy release rates, Gplain [14]:

$$G_{\text{channeling}} = \frac{1}{a}\int_0^a G_{\text{plain}}(a')\,da' \quad (4.1)$$

The computed channeling energy release rate was compared to the weighted energy release rate of PCBN-WC specimen to predict the fracture behaviors. For a unit advance of the channeling crack, the required energy is balanced by the energy needed to create crack surfaces across the whole thickness in both PCBN and WC[15]

$$G_{\text{critical}} = h\Gamma_{PCBN} + (a-h)\Gamma_{WC} \quad (4.2)$$

Where Γ_{PCBN} and Γ_{WC} are critical fracture energies respectively for PCBN layer and WC layer. a is the crack length and h is the thickness of PCBN layer.

Table 4.1. *Material properties of PCBN, hBN and WC*

	Density (kg/m^3)	Thermal Conductivity (W/mK)	Specific Heat (J/kgK)	Poisson's Ratio	Young's Modulus (Gpa)	Thermal expansion coefficient	Fracture Toughness (Mpa√m)
PCBN	3450	200	900	0.15	710	5.6×10^{-6}	5-7.7
hBN	2010	360	600	0.2	70	2×10^{-6}	-
WC	15630	80	300	0.22	570	5×10^{-6}	12-16

4.4 Result and discussion

4.4.1 LWJ cutting result and specimen characterization

Figure 4.2 demonstrated the PCBN-WC samples cut with CO2-LWJ focused and defocused beams. In a previous study on cutting of solid PCBN[16], material separation was successfully achieve with single-pass focused LWJ beam. However, the same cutting condition could not cut though the carbide backed PCBN due to the high toughness of tungsten carbide. Increasing energy input caused destructive cutting edge and uncontrolled breaking of the specimen (Figure 4.2(A)). Due to the failure attempts of cutting with focused beam, the combined focused and defocused beam was introduced to achieve a clean through-cut. A superficial score was first created by a focused LWJ beam with no material separation (Figure 4.2(B)). The multiple-passes defocused beam was then performed that successfully achieved through-cut of this double-layer sample without much surface damage (Figure 4.2(C)). However, sometimes lateral cracks can still be observed but significantly reduced compared to the focused cutting (Figure 4.2(D)).

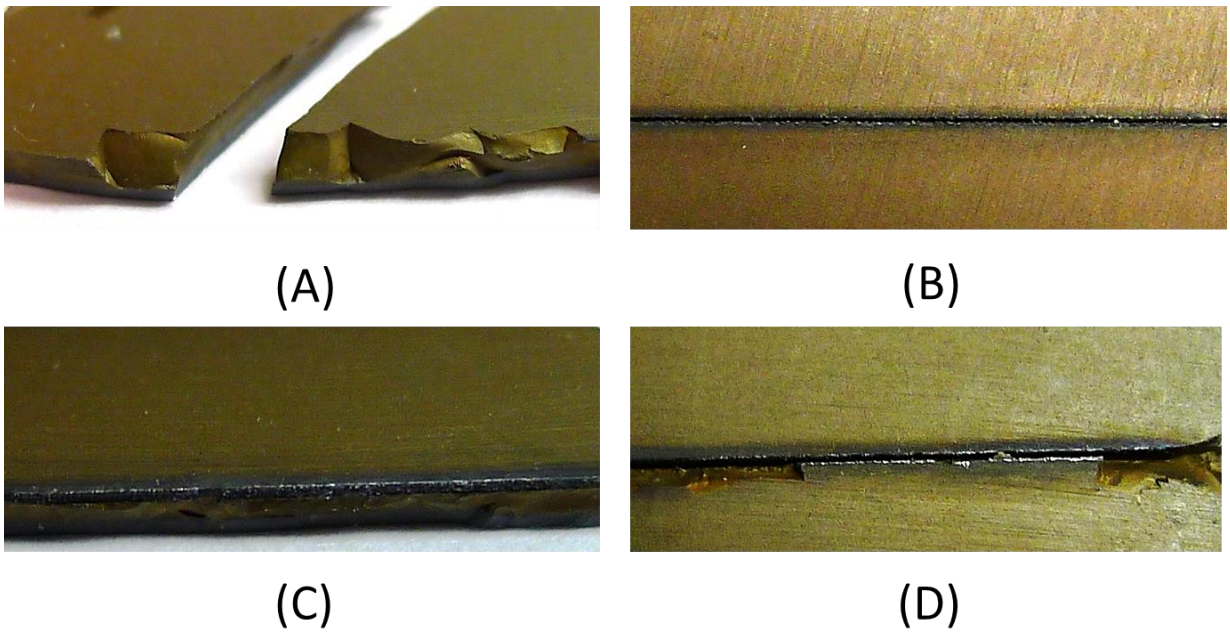

Figure 4.2. *(A) Single-pass focused cutting at high energy input caused severe damage and breaking of the sample (B) Initial groove by focused beam (C) Through-cut after multi-passes defocused beam (D) Less lateral cracks with combined focused and defocused cutting*

SEM micrographs were undertaken for studying micro features of the through-cut specimen. The cut interface with three layers of different surface morphologies is shown in Figure 4.3(A). Raman spectroscopy was carried out on multiple locations across the whole thickness, and the results are shown in Figure 4.4. The top layer was LWJ machined region that shows no cBN phase but several new phases around 1160cm-1, 1370cm-1 and 1530cm-1. The 1370cm-1 peak was reported to be the hBN phase [17] proving that phase transformation happened and produced hBN from original PCBN during laser heating and water quenching. The peak at 1160cm-1 relate to a boron product that has been detected in boron carbide[18], boron oxide and other boron-rich materials[19]. The 1560cm-1 peak has been found in boron carbide and was considered ascribing to the anti-symmetric stretching of the linear chain[20]. In addition, the 1530-1560cm-1 peak was often found in carbon clusters [21, 22] that might be

produced from the chemical reaction of binder during LWJ cutting. The Raman result validated the phase transition of the laser irradiated region therefore was marked as transformation zone in SEM photo (Figure 4.3(A)). The middle layer with a fracture morphology shows only cBN peak at 1059cm-1 and 1302 cm-1[23] and presented the same composition with the original specimen that has been labeled as fracture zone in Figure 4.3(A). The bottom layer labeled as WC zone formed from the propagation of the crack through WC material. Based on the scale shown, the phase transition depth for the PCBN-WC sample are roughly 400μm. Compared to 200μm of solid PCBN cut with single-pass LWJ beam[16], the multiple defocused beam transformed material in a deeper region twice of the single-pass focused beam. Figure 4.3(B) shows the lateral cracks propagated between PCBN and WC interface that lead to spalling of PCBN layer. Figure 4.3(C) shows the chipping-off of the transformed material and the initiation of lateral microcracks from the bottom of the transformation zone. The severe damage not only caused a waste of material but brought inconvenience to the post processing of the specimen, which need to be eliminated in some way.

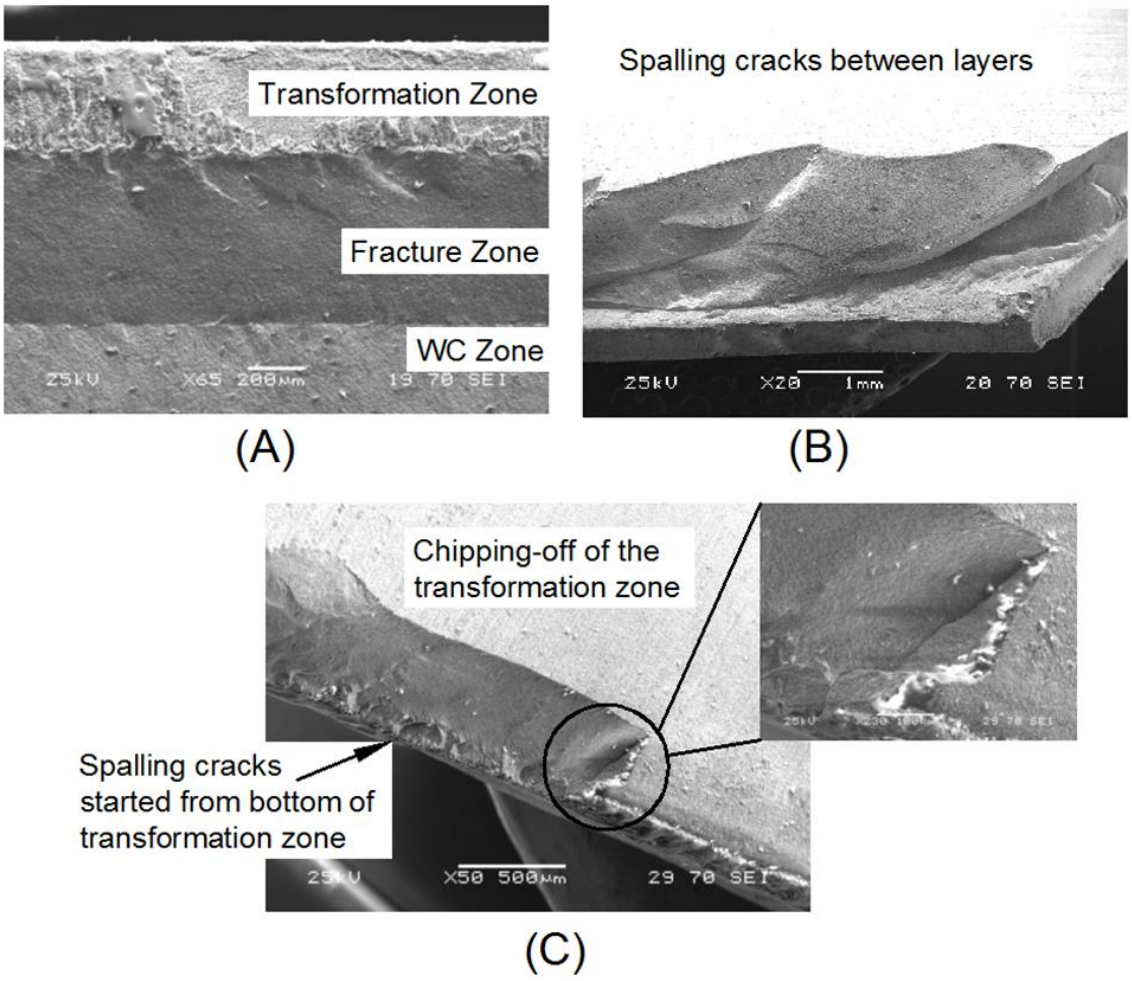

Figure 4.3. *(A) Cross-section image of WC-PCBN after 4 times of defocused machining (B) Chipping-off of the transformation region (C) Spalling cracks at the interface between layers*

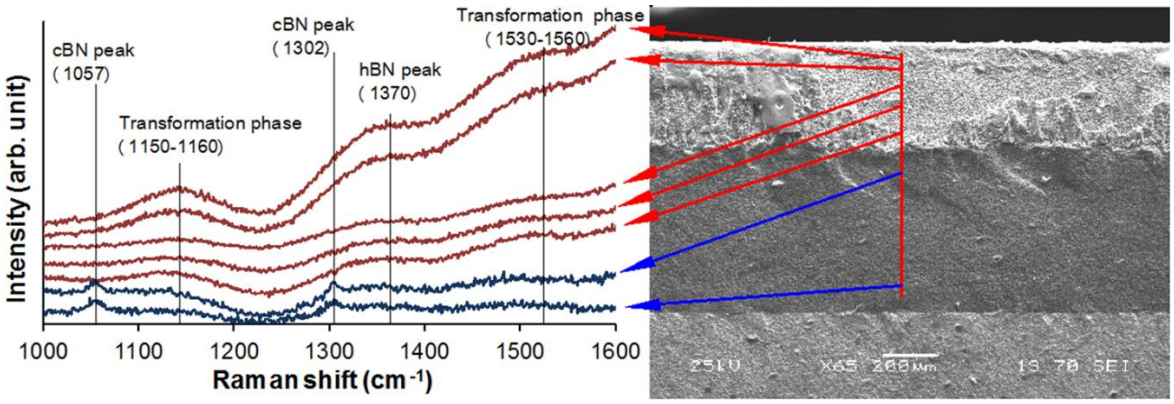

Figure 4.4. *Raman spectrum of transformed zone and fracture zone*

4.4.2 Surface profile measurement and comparison with FEA analytical result

In the second set of experiments performed on the thicker PCBN samples, four scoring lines were observed for the four cuttings with 1, 2, 4 and 8 defocused passes and surface profiles from the center of cutting path are plotted in Figure 4.5. The result shows the progressive effect of the 0.5mm defocused beam. The deformation zone become higher and wider as the increasing of defocused LWJ pass. Profiles of four passes and eight passes are nearly overlapping indicating the saturation of deformation zone at four defocused passes. The width of the breakout (0.3mm in half) corresponds well with the diameter of defocus beam (0.25mm in half). The kerf widths of the four scribing lines were found to be roughly the same (0.11mm in half) and match the focused laser spot size (0.1 mm in half).

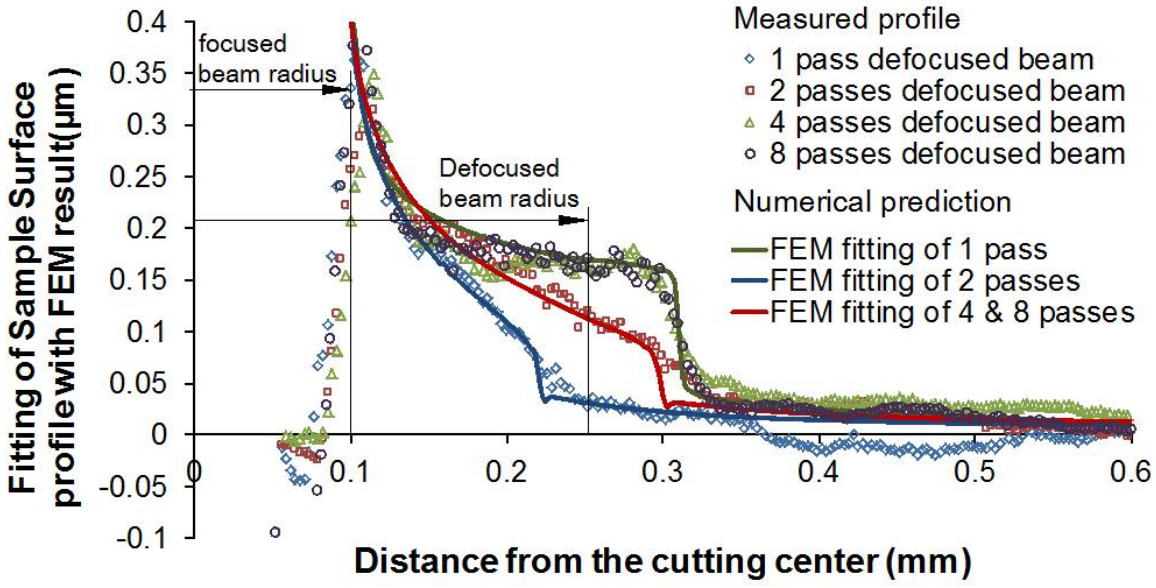

Figure 4.5. *Surface profile the four lines with 1, 2, 4 and 8 defocused passes and comparison of the measured data with FEM based prediction*

The FEA computed results are also plotted in Figure 4.5 for determination of the shapes and dimensions of the transformed zones with a constant expansion strain. This result correspond to a constant expansion strain of 0.008. Cross-sections of the overall transformation

zone were composed of a deep and narrow zone in the vertical direction as well as a wide and shallow zone near surface. The transformation zones along depth direction were modeled as semi-ellipses in order to approximate the influence of Gaussian laser beam. The width of the transformation zone was chosen to be 0.22mm that can well fit the surface profile in all the four cases. The depth of the transformation zone was obtained from the cut interfaces of SEM images (200 μm for single-pass focused cutting and 400 μm for 4-passes defocused cutting). The transformation zones near surface induced by the defocused beam were approximated with different shapes in order to fit the surface profile measurements of each cut line. The groove was simplified to a triangle subtracted from workpiece with depth measured from microscope. Groove width was kept constant as 0.2mm based on the similar surface profile measurements. Figure 4.6 represented the development of the transformed region for multiple defocused laser passes in FEA model. Detailed shapes and dimensions of cross-sections of the transformation zone for different numbers of defocused passes were summarized in Table 4.2.

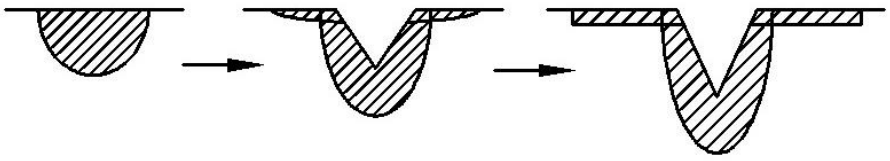

Figure 4.6. *Simplification of the transformed region for multiple defocused laser passes in FEA model*

Table 4.2. *Shape and dimensions of transformation zone near surface*

# of defocused passes	Semi-ellipse depth	Groove depth	Shape of defocused transformation zone	Dimensions of defocused transformation zone
0	200μm	0	-	-
1	250μm	150μm	ellipse	Depth: 5μm, width:220μm in half
2	300μm	160μm	ellipse	Depth: 5μm, width:300μm in half
4&8	400μm	175μm	rectangle	Depth: 5μm, width:300μm in half

Figure 4.5 demonstrate well agreement of predicted numerical result with experimental measured surface profile indicated that the chosen shapes and expansion strain for the phase transition zone were capable to reflect the progressive effect of the defocused cutting passes. The initial focused pass transformed material in a deep and narrow region and a grooved was produced due to material evaporation. The following defocused passes induced a wide and shallow transformation zone near sample surface and deepened the existing transformation zone and groove depth. As the number of pass increased, more material has been transformed resulting in the higher and wider breakout of material. The material phase transition reached saturation at four passes such that no more deformation could be induced even with more LWJ passes. The estimated transformation zone size and expansion strains are utilized in the FEA fracture model of PCBN-WC specimen to determine the energy release rates as a function of crack depth.

4.4.3 Energy release rate calculation of channeling cracks

Energy release rate was computed to characterize the fracture behavior of double-layer PCBN-WC sample cut with combined focused and defocused beam. The calculation was achieved in two steps: the single-pass scribing with focused LWJ beam and 4 passes of defocused beam that achieved through cut. Dimensions of transformation zone obtained in Table 4.2 and expansion strain of 0.008 were utilized in fracture models. Figure 4.7 plotted the channeling energy release rate computed from equation (1) as a function of a/w (ratio of crack length to the thickness of material) corresponding to the cutting parameters of 100in/min and 400W. Computed energy release rate was also compared to the weighted critical channeling energy obtained from equation (2) to predict the fracture behavior. The fracture energy of WC was reported to be 240N/m-602N/m[24] and the PCBN was 81N/m-137N/m in literature[25].

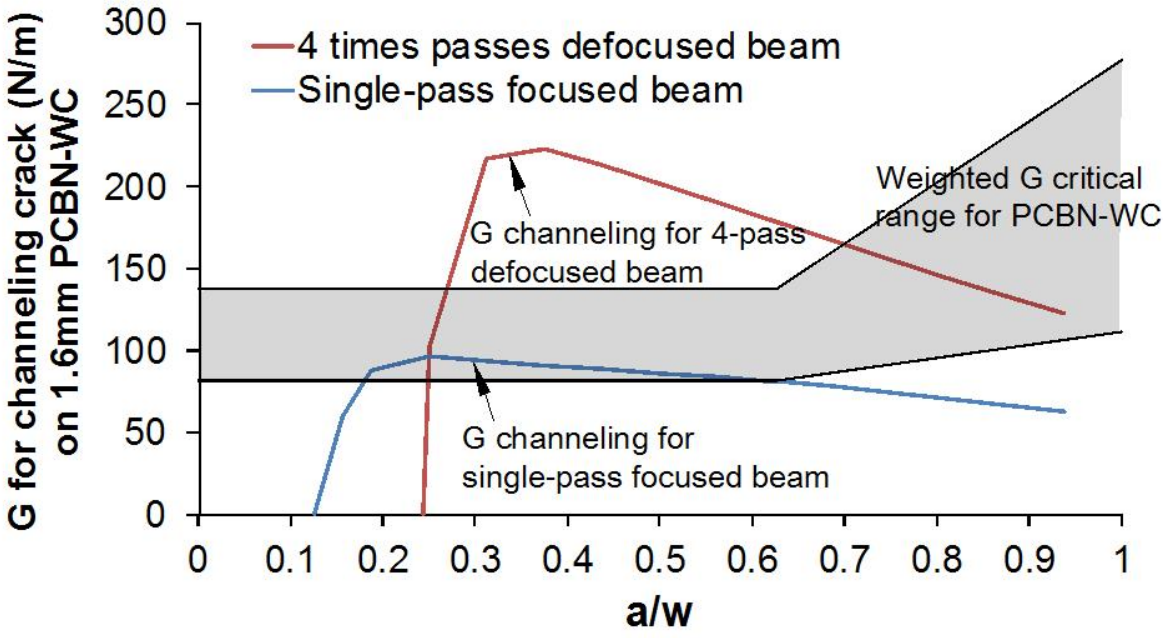

Figure 4.7. *Energy release rate for channeling crack machined with single-pass focused beam and 4 times defocused beam*

Based on fracture mechanics theory, initial crack will propagate if the energy release rate exceeds the critical fracture energy of material, otherwise crack will stop from growth. As shown in Figure 4.6, magnitudes of energy release rates of the initial focused pass was lower than the critical range of PCBN and WC indicating no crack propagation under single-pass LWJ cutting . While the energy release rates for 4 times defocused beam increased more than twice that capable to drive the crack through most of the whole thickness. Besides the increasing of fracture energy, defocused LWJ machining also applied thermal shock to the whole specimen leading to degradation of fracture toughness of tungsten carbide. Dongbin Han and John Mecholsky[26] reported that the toughness of tungsten carbide decreased 20% in 3 times of thermal shock with temperature gradient of 400 ℃. The similar situation happened in the multiple defocused LWJ machining that leading to the reduction of fracture toughness of tungsten carbide that also helped crack propagation through.

4.4.4 Fracture energy calculation of spalling cracks and a possible solution to reduce spalling

Experimental observation (SEM graphs of Figure 4.3(B) and 4.3(C)) suggested that two vulnerable locations were most probable for initiation of lateral cracks: the interface between two layers and the region just below the transformation zone. The interface crack might come from the defects in the original tool blank during sintering procedure thus it is not going to be discussed in this paper.

Modeling investigation of the lateral cracks near transformation zone were performed for three cases: the single-pass focused cutting, combined focused and defocused cutting and a designed case aiming to reduce lateral cracks. In all the three models, expansion strain was maintained at 0.008 and the dimensions of phase transition zone induced by LWJ beam was

designed to make sure that the magnitude of fracture energy for channeling crack was above the critical value in order to achieve material separation. For the single-pass focused cutting, a semi-elliptical transformation zone of 0.6mm deep and 0.22mm wide was required to achieve a through-cut. Dimensions of defocused cutting have been obtained in Table 4.2. A flat transformation zone was designed for minimizing lateral cracks and a semi-elliptical zone of 0.6mm in width and 0.25mm in depth can satisfy the through-cut condition.

In all the three cases, lateral cracks were assigned to a very small initial value of 0.016mm (a/w = 0.01) and an initial direction parallel to the sample surface at three locations: 0.016mm(0.01w), 0.048mm(0.03w) and 0.08mm(0.05w) below the phase transition zone. Figure 4.8 shows the energy release rate of lateral cracks for the three cases. In all the three cases, energy release rate decreased as the initial crack location getting far away from the transformation zone. Therefore most lateral cracks were observed near phase transition zone. The single-pass focused beam induced the largest fracture energy for the lateral crack which agree with the experimental observation of the spalling of specimen. The defocused cutting caused less fracture energy so that lateral cracks got suppressed compared to focused beam cutting. The designed flat transformation zone induced compressive stress field intent to close the crack and resulted in zero fracture energy. Therefore wider and shallower transition zone is feasible to reduce or even eliminate the lateral cracks.

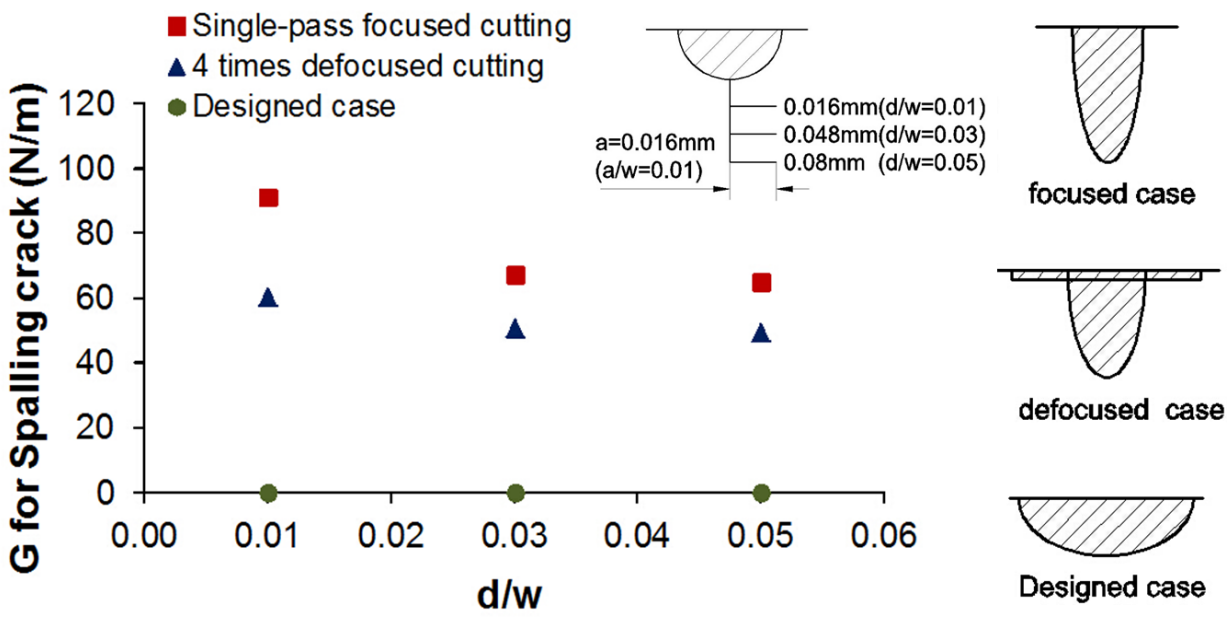

Figure 4.8. *Energy release rate of 0.01w spalling cracks at 0.01w, 0.03w and 0.05w below transformation zone*

All the experimental testing and numerical modeling suggest the mechanism of the combined focused and defocused beam through a phase transition induced fracture propagation: (1) During initial focused scoring the localized laser heating and subsequent waterjet quenching caused phase transition of PCBN along the cutting path from sp3-bonded phase into sp2-bonded phases that resulted in a volume expansion in a deep and narrow region (2) Multiple defocused passes transformed material in a flat zone on sample surface and deepened the existing zone in vertical direction. (3) The constrained volumetric expansion resulted in sample deformation and development of stress field in the material surrounding the transformation zone. (4) The stress field lead to vertical crack propagation towards both thickness direction and along laser path that achieved material separation. At the same time, stresses induced by the wide and shallow zone on top surface helped suppress lateral cracks.

4.5 Conclusion

LWJ Cutting experiments are conducted on the 1.6mm tungsten carbide supported PCBN with process parameters of 100in/min and 400W. A new method of performing multi-passes defocused beam after the scribing of single-pass focused beam was applied that successfully achieved complete cutting. In order to understand the function of the defocused beam, a set of experiments was performed on a 4.8mm thick PCBN piece with 1, 2, 4 and 8 defocused passes after the scribing of focused beam aiming at duplicate the cutting effect during defocused machining without material separation. Lateral cracks were found in focused cutting and the defocused machining can apparently suppress uncontrolled lateral cracks compared with the focused one.

Material separation mechanism is proved to occur through controlled fracture propagation under the stress fields imposed by the volumetric expansion associated with phase transition. FEA model with a uniform expansion zone was utilized to model the influence of material transformation along the cutting path. Transformation depth was determined from SEM image of cut interface to be 200 μm for single-pass cutting and 400 μm for multi-passes defocused cutting. Surface profile of the 4.8mm sample for studying defocused beam was measured using profilometry and compared with FEA predicted deformation to estimate the expansion strain and shapes of transformation region. The best fitting expansion strain was found to be 0.008. Based on the obtained expansion strain and transformation zone size, a FEA fracture model was developed to estimate crack behavior for double-layer PCBN-WC specimen. The model result represent well agreement with experimental observations. Initiation of lateral cracks was also studied in this paper. The energy release rate of lateral crack for three cases were calculated: the single-pass focused cutting, combined focused and

defocused cutting and a designed case aiming to reduce lateral cracks. Results explained suppression of lateral cracks machined by defocused beam and suggested a wider and shallower transformation zone for reducing the uncontrolled lateral cracks.

4.6 References

[1] P. B. Mirkarimi, K. F. McCarty, and D. L. Medlin, "Review of advances in cubic boron nitride film synthesis," *Materials Science & Engineering R-Reports*, vol. 21, pp. 47-100, Dec 15 1997.

[2] X. Ding, W. Y. H. Liew, and X. D. Liu, "Evaluation of machining performance of MMC with PCBN and PCD tools," *Wear*, vol. 259, pp. 1225-1234, 2005.

[3] X. L. Liu, Y. F. Li, F. G. Yan, Y. Wang, J. S. Hu, and Y. J. Wang, "Study on precision grinding technique of PCD tool's cutting edge," in *Advances in Grinding and Abrasive Technology Xiii*. vol. 304-305, ed, 2006, pp. 186-190.

[4] M. Akaishi and S. Yamaoka, "Physical and chemical properties of the heat resistant diamond compacts from diamond-magnesium carbonate system," *Materials Science and Engineering a-Structural Materials Properties Microstructure and Processing*, vol. 209, pp. 54-59, May 1996.

[5] T. Irifune, A. Kurio, S. Sakamoto, T. Inoue, and H. Sumiya, "Materials - Ultrahard polycrystalline diamond from graphite," *Nature*, vol. 421, pp. 599-600, Feb 6 2003.

[6] H. Sachdev, R. Haubner, H. Noth, and B. Lux, "Investigation of the cBN/h-BN phase transformation at normal pressure," *Diamond and Related Materials*, vol. 6, pp. 286-292, Mar 1997.

[7] J. Robertson, "Diamond-like amorphous carbon," *Materials Science & Engineering R-Reports,* vol. 37, pp. 129-281, May 24 2002.

[8] Y. H. Liu, Y. F. Guo, and J. C. Liu, "Electric discharge milling of polycrystalline diamond," *Proceedings of the Institution of Mechanical Engineers Part B-Journal of Engineering Manufacture,* vol. 211, pp. 643-647, 1997.

[9] P. L. Tso and Y. G. Liu, "Study on PCD machining," *International Journal of Machine Tools & Manufacture,* vol. 42, pp. 331-334, Feb 2002.

[10] J. Y. Pei, C. N. Guo, and D. J. Hu, "Electrical discharge grinding of polycrystalline diamond," in *Advances in Materials Manufacturing Science and Technology*. vol. 471-472, ed, 2004, pp. 457-461.

[11] A. Pauchard, M. D. Marco, B. Carron, G. Suruceanu, B. Richerzhagen, A. Brulé, *et al.*, "Recent Developments in the Cutting of Ultra Hard Materials Using Water Jet-Guided Laser Technology," presented at the ALAC, 2008.

[12] C. H. Tsai and H. W. Chen, "Laser cutting of thick ceramic substrates by controlled fracture technique," *Journal of Materials Processing Technology,* vol. 136, pp. 166-173, May 10 2003.

[13] F. R. Corrigan and F. P. Bundy, "Direct Transitions among Allotropic Forms of Boron-Nitride at High-Pressures and Temperatures," *Journal of Chemical Physics,* vol. 63, pp. 3812-3820, 1975.

[14] S. Ho and Z. Suo, "Tunneling Cracks in Constrained Layers," *Journal of Applied Mechanics-Transactions of the Asme,* vol. 60, pp. 890-894, Dec 1993.

[15] T. Ye, Z. Suo, and A. G. Evans, "Thin-Film Cracking and the Roles of Substrate and Interface," *International Journal of Solids and Structures,* vol. 29, pp. 2639-2648, 1992.

[16] Z. Wu, "The mechanism governing cutting of Polycrystalline Cubic Boron Nitride (PCBN) tool blanks with phase transformation induced fracture," Master of Science, Mechanical Engineering, Iowa State University, 2013.

[17] L. Song, L. J. Ci, H. Lu, P. B. Sorokin, C. H. Jin, J. Ni, *et al.*, "Large Scale Growth and Characterization of Atomic Hexagonal Boron Nitride Layers," *Nano Letters,* vol. 10, pp. 3209-3215, Aug 2010.

[18] U. Kuhlmann and H. Werheit, "Raman Effect of Boron-Carbide (B4.3c to B10.37c)," *Journal of Alloys and Compounds,* vol. 205, pp. 87-91, Mar 1994.

[19] V. L. Solozhenko and O. O. Kurakevych, "New boron subnitride B13N2: HP-HT synthesis, structure and equation of state," *Joint 21st Airapt and 45th Ehprg International Conference on High Pressure Science and Technology,* vol. 121, 2008.

[20] K. Shirai and S. Emura, "Lattice vibrations and the bonding nature of boron carbide," *Journal of Physics-Condensed Matter,* vol. 8, pp. 10919-10929, Dec 9 1996.

[21] M. Yoshikawa, G. Katagiri, H. Ishida, A. Ishitani, and T. Akamatsu, "Raman-Spectra of Diamondlike Amorphous-Carbon Films," *Journal of Applied Physics,* vol. 64, pp. 6464-6468, Dec 1 1988.

[22] M. Yoshikawa, Y. Mori, H. Obata, M. Maegawa, G. Katagiri, H. Ishida, *et al.*, "Raman-Scattering from Nanometer-Sized Diamond," *Applied Physics Letters,* vol. 67, pp. 694-696, Jul 31 1995.

[23] H. Sachdev, "Influence of impurities on the morphology and Raman spectra of cubic boron nitride," *Diamond and Related Materials,* vol. 12, pp. 1275-1286, Aug 2003.

[24] K. Jia, T. E. Fischer, and B. Gallois, "Microstructure, hardness and toughness of nanostructured and conventional WC-Co composites," *Nanostructured Materials,* vol. 10, pp. 875-891, Jul 1998.

[25] M. P. DEvelyn and K. Zgonc, "Elastic properties of polycrystalline cubic boron nitride and diamond by dynamic resonance measurements," *Diamond and Related Materials,* vol. 6, pp. 812-816, Apr 1997.

[26] D. B. Han and J. J. Mecholsky, "Strength and Toughness Degradation of Tungsten Carbide-Cobalt Due to Thermal-Shock," *Journal of the American Ceramic Society,* vol. 73, pp. 3692-3695, Dec 1990.

CHAPTER V

THE EFFECT OF ASSIST FLUID ON LASER MACHINING OF POLYCRYSTALLINE CUBIC BORON NITRIDE (PCBN)

Zhuoru Wu, Ammar Melaibari, Pal Molian and Pranav Shrotriya

Abstract

Polycrystalline Cubic Boron Nitride (PCBN) is an ultrahard material that difficult for machining with traditional methods. An innovative method combining CO2-laser with various assist media was able to achieve high-quality cutting of PCBN through controlled fracture that can overcome the deficiencies of existing methods such as thermal damage and low speed. In order to understand the role of assist media in laser machining, cutting experiments was undertaken on PCBN samples with three assist fluids: Argon, Nitrogen and Waterjet. Though-cut were achieved in all the three samples and cutting features were studied by Raman spectroscopy, scanning electron microscopy (SEM) and optical profilometry. The cutting mechanism was proved to be material phase transition induced fracture propagation. Laser heated PCBN undergoes chemical phase transformation from sp3-bonded cubic phase (cBN) into hexagonal phase (hBN) and other sp2-bonded phases. The transformed material occupies more volume that expand the original material and lead to tensile stresses. The stress drive the crack propagated in a controlled way that separate the material. A theoretical model predicting phase transition induced material deformation was developed to obtain transformation strain and transformation zone size. These values are subsequently used in a fracture model to estimate fracture energy for predicting crack behaviors (scribing/through-cut) and compared with experimental cutting observations. Both modeling and experimental result indicated that

Waterjet coupled threshold amount of laser energy that produced thin transformed layer as well as controlled cracking; while Nitrogen and Argon have stronger ability to couple laser energy but unfavorable to control fracture propagation because of over deep phase transition zone and rough cut interface.

KEYWORDS: Laser machining, PCBN, assist gas, controlled fracture, phase transformation

5.1 Introduction

Polycrystalline cubic boron nitride (PCBN) is the second hardest known material, diamond being the hardest. Unlike diamond, PCBN does not exist in a natural form, but only synthetically made. It is one of the best-performance cutting tool material for machining hard cast iron, high chrome alloy steels, high-strength nickel super alloys and powder metal alloys because of its advantages over diamond in terms of thermal and chemical stability. PCBN is manufactured by sintering fine particles of cBN with the aid of ceramic matrix typically TiN or AlN under high pressure and high temperature conditions. PCBN not only possesses the outstanding mechanical properties such as extreme hardness and wear resistance but also exhibits high thermal conductivity, high Young's Modulus, low coefficient of friction, and chemical inertness (less reactive to metals like titanium). In recent years, PCBN tools are increasingly used in micro-manufacturing of a variety of precision components because PCBN is able to keep its nature when scaling down the end mills from conventional to microscopic sizes. In addition, PCBN meets the high demands of form accuracy, surface quality and low subsurface damage in ductile machining of brittle materials.

Boron nitride exits four main phases: hexagonal (hBN), rhombohedral (rBN), cubic zincblende (cBN), and wurtzite (wBN) phases. The cBN and wBN phases are diamond-like

sp3 bonded phases and hBN and rBN phases are graphite-like sp2 phases. The stable phases at ambient conditions are cBN and hBN structure while rBN and wBN are metastable phases that cannot last for a long time. Transformation between these phases might happen under high temperature or high pressure[4]. It was reported that the sp2-bonded structure occupies much more volume than sp3-bonded structure[5].

Many machining techniques have been developed to shape PCBN that ranged from waterjet to electric discharge machining (EDM) and pulsed Nd:YAG laser. Waterjet was not favorable due to the shortcomings of time consumption, wide kerf, and poor surface finish and taper. In EDM, the process has been used to fabricate all insert shapes with good quality, but the material removal rates were very low. The Nd:YAG laser has excellent prospects for machining PCBN but suffers from central issues like formation of recast layer, phase transition and kerf geometry that require a secondary process. Thus the existing processes for the fabrication of PCBN tools are inefficient with respect to cost, time, and energy consumption.

We have recently demonstrated a novel, hybrid CO2 laser/waterjet(LWJ) process for machining hard ceramic materials that seems to eliminate many of the deficiencies associated with pulsed Nd:YAG laser and EDM [2, 3]. It may be noted that LWJ uses an entirely different mechanism than conventional laser machining where a laser beam causes the material removal by heating up and evaporating the material. In LWJ, stresses induced by phase transition provide controlled crack initiation and propagation that offers a fast, cheap, and low energy approach to cut PCBN. The LWJ process begins with rapid laser heating followed by waterjet (fast quenching) leading to localized damage and phase transformation of surface layer that resulting in a stress field surrounding the transformed material. The stress fields propagate the localized cracks through the thickness with small kerfs, less taper and high-speed. In addition

to waterjet, other media such as Argon, Nitrogen, Oxygen and air were often functioned as assist gas in laser machining[1-3]. In this paper, the influence of three assist fluids: Argon, Nitrogen and waterjet, on the mechanism of material removal, is investigated and compared. The laser machining system with different assist fluids is schematically shown in Figure 5.1. An analytical model was developed for studying the laser/assist media machining mechanism of phase transition induced fracture propagation. The model was validated through comparison with surface deformation measurement. The validated model was then used to compute energy release rate of crack and compared with the fracture toughness of PCBN to understand the effect of each assist fluid.

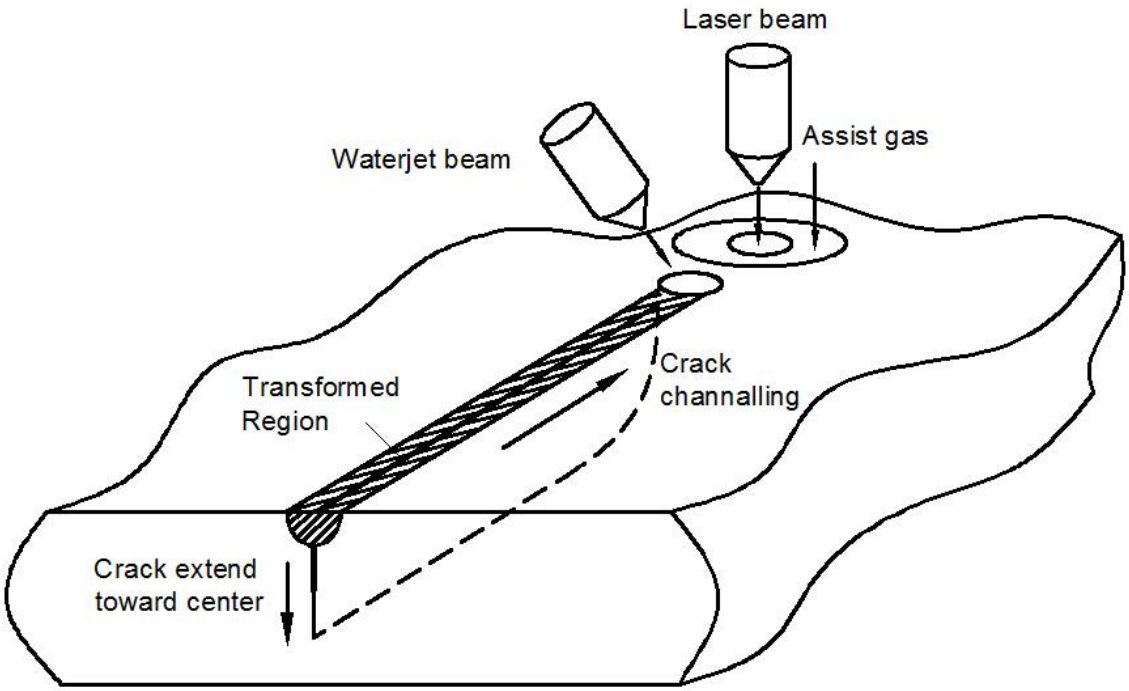

Figure 5.1. *Laser machining system with different assist fluids*

5.2 Experiment

5.2.1 Cutting experiments details

Equilateral triangular inserts of solid PCBN, prepared by EDM, were offered by Diamond Innovations (Worthington, Ohio) for the experiments. The triangles have 7 mm side length and 1.6 mm thickness. The average particle size is 4 μm with a composition of 75% of cBN and 25% of Ti based matrix containing carbon (BZN 9000 series). Surface roughness (Ra) of the top (polished) and the side (EDM machined) were 0.3 and 3 μm respectively.

A continuous wave CO2 Laser (Model 820 Spectra Physics) of 10.6 μm wavelength and 500W power was used in all the cutting experiments. The laser beam was focused to a spot of 0.2 mm diameter on the sample surface. Three different assist fluids: Argon, Nitrogen and Waterjet were used along with laser to cut three the triangular inserts. Laser machining was accomplished at two different cutting speeds of 42.3 and 84.6 mm/sec (100 and 200 in/min) for each PCBN insert. The pressure of Argon and Nitrogen was kept at 140 kPa (20 psi) and the pressure of abrasive-free waterjet was kept higher at 5.5 MPa (800 psi). The assist gas of Argon and Nitrogen was transmitted surround the laser beam through the same passage with laser beam. The waterjet was transported from a pump through a separate hole with a spacing of 4mm from laser beam to avoid the absorption of laser power by direct contact with water. Details of the LWJ setup are described elsewhere [4].

5.2.2 Cutting sample characterization and 3D surface profiling

Measurements of kerf geometries and surface roughness profiles were carried out using an optical profilometry (Zygo NewView 7100) with 5X and 20X magnifications. Scanning electron microscopy (SEM Model JEOL JSM-606LV at 20 kV) was used to characterize the machined layer and identify the depth of phase transition zone. Dispersive Raman spectroscopy

(Renishaw-inVia Raman Microscopy) was used to test the phase transitions of cut samples. Ar-ion laser at 488 nm wavelength was used for excitation.

The 3D topographies of top surfaces around each cutting edge were measured with optical profilometry (Zygo NewView 7100) of the three machined samples assisted with Nitrogen, Argon and Waterjet. Surface height distribution along a line normal to the cutting path can be obtained by averaging the 3D data along the cutting direction. The averaged data characterized laser machining deformation was compared with FEM predictions for validating the expected cutting mechanism.

5.3 Numerical modeling and validation

5.3.1 Finite element model for determination of cutting induced deformation

Previous study on laser cutting assisted with waterjet was proved to achieve material separation through a "score and snap" mechanism: (1) Laser irradiated zone of the PCBN specimen undergoes a phase transition that expanding the original volume; (2) phase transition induced constrained volumetric expansion resulted in sample deformation and development of tensile stress field below the expansion region; (3) A score line was also created due to laser ablation and the tensile stress fields drove the scribing crack propagating through the whole thickness. In this paper, Nitrogen and Argon will be analyzed based on the same method and the role of different assist fluids will be compared and discussed.

Finite element model was developed in ABAQUS (Simulia, Providence, RI) to predict the deformation in PCBN samples after laser machining and compared with the experimental measurement. A transformation zone undergoing uniform expansion along the laser cutting path was utilized to model the influence of material phase transition. The model can be

simplified to 2D plane strain state of a cross-section perpendicular to the laser path as shown in Figure 5.2(a). Half of the specimen was analyzed with zero boundary condition on the axis of symmetry. The phase transition zone was characterized by a semi-elliptical shape to catch the effect of the Gaussian laser beam. The model was composed of 8-noded quadratic plane strain elements with refined mesh in the phase transition zone. The transformed region was applied to the material properties of hBN – a typical phase with sp2 structure found in the transformed region, and the rest was assigned properties of PCBN. The depth of the semi-elliptical transition zone were measured from the SEM images of transverse cross-section of the cut specimen. The width of the transformation zone will be determined based on the comparison of FEA predicted surface deformation with the surface profiling measurements. The expansion strain of the transformation zone was also obtained through this comparison. The expansion size and expansion strain are subsequently used to estimate fracture energy for cracks that lead to cutting/scribing of the sample.

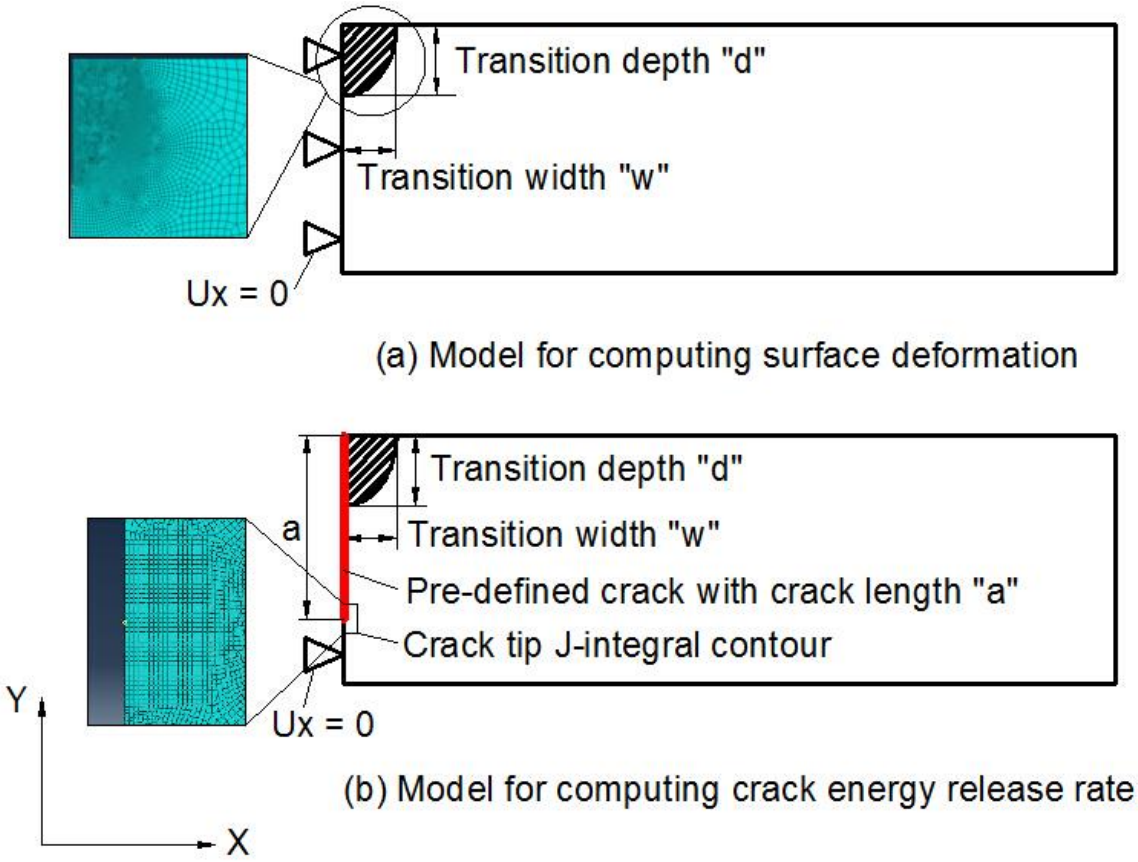

Figure 5.2. *Finite element model for computing (a) surface deformation induced by material phase transition; (b) energy release rate for crack at different depth*

5.3.2 Fracture mechanics analysis of cracks

Based on the obtained transformation size and strain, fracture mechanics analysis was performed to determine the crack propagation behavior. The machining may be represented through a two-step analysis: at the beginning of the cut when there are no pre-existing cracks in the workpiece, plane strain analysis of edge crack may be utilized to approximate the initial cut depth. Subsequently, analysis of the channeling crack may be utilized to approximate the propagation of the initiated cut along the laser path. The two crack configurations were shown in Figure 1: crack extended towards center of plate and crack channeled along the laser moving direction. Plane strain condition was applied to the former for estimating the energy release

rate at different crack lengths across the whole thickness. The energy release rate of the later crack configuration was computed by integrating and averaging plain strain energy release rates over the crack depth.

For the plane strain crack configuration, fracture energy was calculated through J-integral evaluation[5] on multiple contours around the crack tip. Stable value could be reached at out layers of elements with suitable mesh refinement. The crack model was implemented the same configurations as the model for calculating surface deformation except the existing of a pre-defined crack located at the center of the transformation zone (Figure 5.2(b)). Crack length varied from a small initial value below the transformation region to the rest of whole thickness. For each model with different length of crack, J-integral was computed individually to get the function of energy release rate verses crack length.

Energy release rate for channeling of the existing plane strain crack was computed following method of Ho and Suo[6]. For steady state crack, it is assumed that crack propagated at a fixed depth and a constant shape. The channeling process can be treated as removing a unit slice far ahead of the crack tip and attaching a unit slice with plane strain crack far behind the crack tip. The difference of energy stored in these two unit slices is the released energy for crack propagating unit distance, which is the released energy of the plane strain crack and can be obtained by integration

$$G_{\text{channeling}} = \frac{1}{a}\int_0^a G(a')\,da' \quad (5.1)$$

Where $G(a')$ is the fracture energy for plane strain cracks of various depths.

Channeling energy release rates were compared with critical value of material properties for predicting fracture behaviors for each cutting condition.

5.4 Results and discussion

5.4.1 Laser cutting results and Raman spectroscopy with different assist media

The cutting efficiency and overall quality was strongly depended on the type of assist media. At the cutting speed of 100in/min (42.3 mm/sec), complete separation was achieved using Nitrogen and Argon. Waterjet caused deep scribing of the sample that can be snapped by hand pressure. At the cutting speed of 200in/min (84.6 mm/sec), only scribing was found in all the three samples. The kerf widths were measured by optical microscope to be 200 μm assisted by waterjet, 220 μm assisted by Argon and 230 μm assisted by Nitrogen. SEM was used for study of material microstructures of specimens machined with different fluid media. Figure 3 represents the SEM images of cutting section for the three complete separation samples at the velocity of 42.3 mm/sec. On the cutting section of each specimen, two distinct layers with different microstructures could be observed which were marked as transition zone and fracture zone in Figure 5.3. The transition layer near top surface was formed under chemical reaction between PCBN, laser and assist media. The fracture layer below that was generated by crack formation and propagation through the thickness. The transition layer produce by different media represented different structures and roughness. Nitrogen produced the roughest machining layer with a debris-like particulate structure. Argon-machined layer behaved a less rough structure than nitrogen while the recasting of particles could still be observed somewhere. Waterjet produced the finest structure with small roughness and slight recast phenomenon. The depths of the transformation zones were measured to be 500 μm, 350 μm and 310 μm for nitrogen, argon and waterjet assisted samples respectively base on the scale shown on the image.

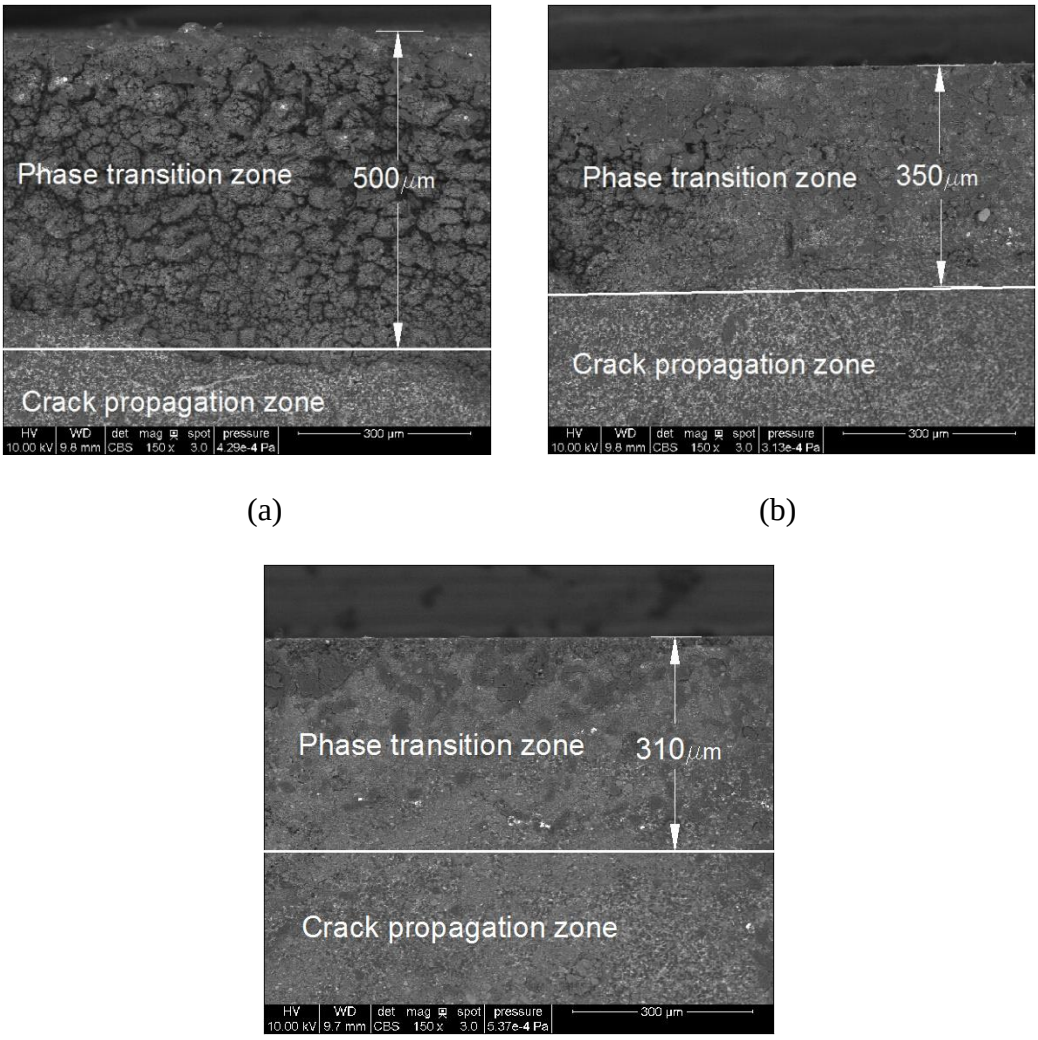

(a) (b)

(c)

Figure 3 *SEM image of cutting section for specimens with assist media of (a) Nitrogen (b) Argon (c) Waterjet*

Raman Spectroscopy was conducted on the cutting transverse sections for analyzing the phase transition under the three assist media. Figure 4 displays the recorded spectrum of the three transformed layers as well as the fracture zone of PCBN covering a Raman shift range from 1250 to 1700 cm^{-1} where Boron composites vibrations reside. The cracked area has the same structure as in the bare material that clear shown 1302 cm-1 peak of

cBN[7]. The machined area revealed no cBN peak but several new phases for each of the three samples. In all of them, two broad peaks around 1370 cm^{-1} and 1580 cm^{-1} can be observed. The 1370 cm^{-1} peak could belong to sp2 bonding between N-B in the rhombohedral phase (rBN) or in plane vibrations of the hexagonal phase (hBN) [8]. The slight shifting of this peak in the three samples can be attributed to the effect of decreasing in the crystalline size of hBN. Nemanich et al[9] indicated that the Raman line for hBN can be shifted to higher frequency, broadened, and became asymmetric as the crystalline size decreases. The Raman features around 1580 cm^{-1} can be attributed to hBNC[10] or B4C[11] probably resulted from reaction between BN with carbon from the binder. The formation of rhombohedral BN and well-crystallized hBN layers was observed along grain boundaries. Rapid heating and cooling associated with the process will cause the more probable cBN transformation to hBN, hBNC and rhombohedral phase.

Raman spectroscopy result provided the fundamental support for the cutting mechanism that laser irradiation led to material phase transition from sp3-bonded cBN to sp2-bonded BN phases. Similar Raman peaks detected in all the three specimens suggested that phase transition was independent from assist fluids. The assist media was considered mainly serving two purposes: (1) Shielded processing area to minimize oxidization and heat affected zones, (2) Affected laser energy absorption and penetration. Different types of assist gas have been widely used in laser welding. Assist gases could remove the plasma produced during laser processing that scatters the laser beam, such that the laser absorptivity can be increased[12].

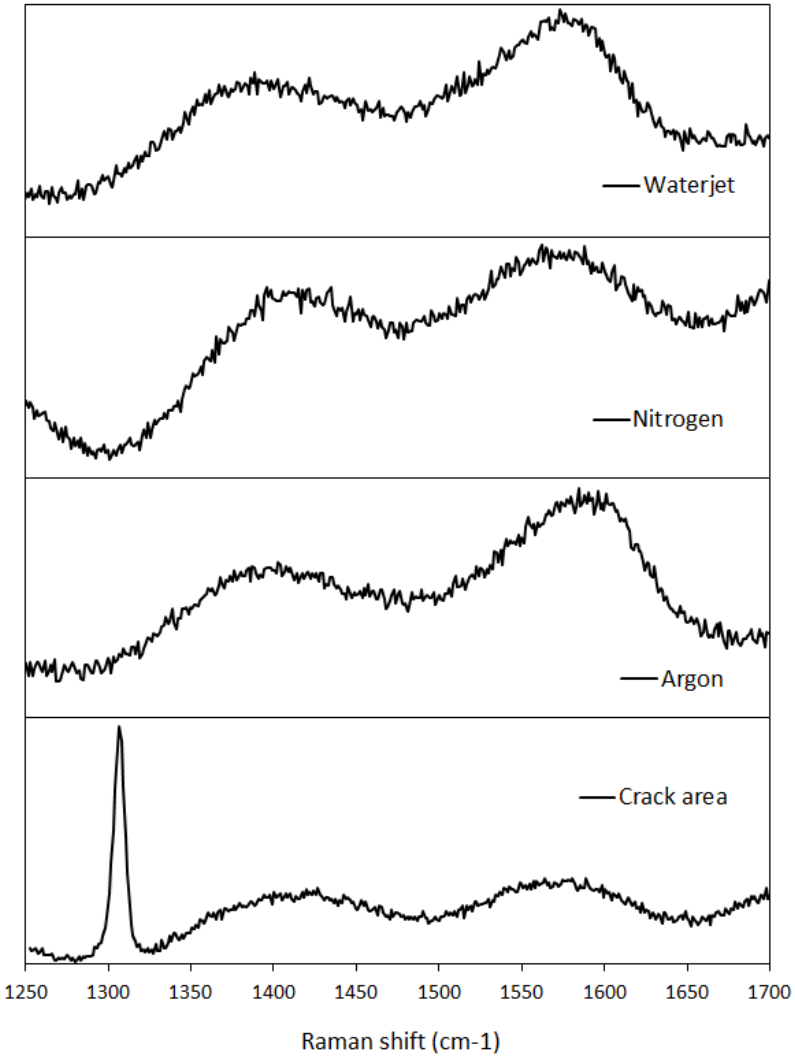

Figure 5.4. *Raman Spectroscopy for crack zone and machined zone with Nitrogen, Argon and waterjet*

Among the three assist media, Nitrogen produced the deepest machining zone and widest kerf that probably due to the highest laser energy coupling capability. Raman spectroscopy revealed the presence of hBN and hBNC phases could be the reason for the rough cutting interface. The transformed phase and sputtered particles from evaporation that make up the recast layer may account for high degree of surface roughness of the machining zone. This interaction has been recorded between diamond and different gases in a research

conducted by Gloor et al[13]. Argon performed medium energy coupling capability that yield a shallower machining depth. In the waterjet assist cutting, the laser energy was partly dissipated by waterjet that reduced the amount of energy been absorbed and penetration depth. Therefore waterjet sample represented the shallowest machining zone and small kerf width as well as a relative smooth microstructure. Among Nitrogen, Argon and waterjet, waterjet was find to be the best assist medium because of its thin and good-quality machining region, less sputtered particles and light recast layer. The crack propagation was much better controlled due to the rapid quenching.

5.4.2 Surface profiling of phase transition induced deformation and comparison with modeling result

3D topographies of top surfaces adjacent to the cut edge was measured using optical profilometry for the three through-cut specimens assisted with Argon, Nitrogen and waterjet. Average height distribution along a line perpendicular to the cut characterized surface deformation induced by material phase transition during laser cutting. The scattered curve in Figure 5 represented the surface deformation for the three specimens. Surface deformation is highest near the cutting edge and decays gradually as the distance getting larger from the cut center. Among the three assisted media, Nitrogen produced the largest magnitude of surface deformation because of its best coupling ability with laser energy. Argon induced middle amount of deformation and waterjet induced the least due to the dissipation of energy.

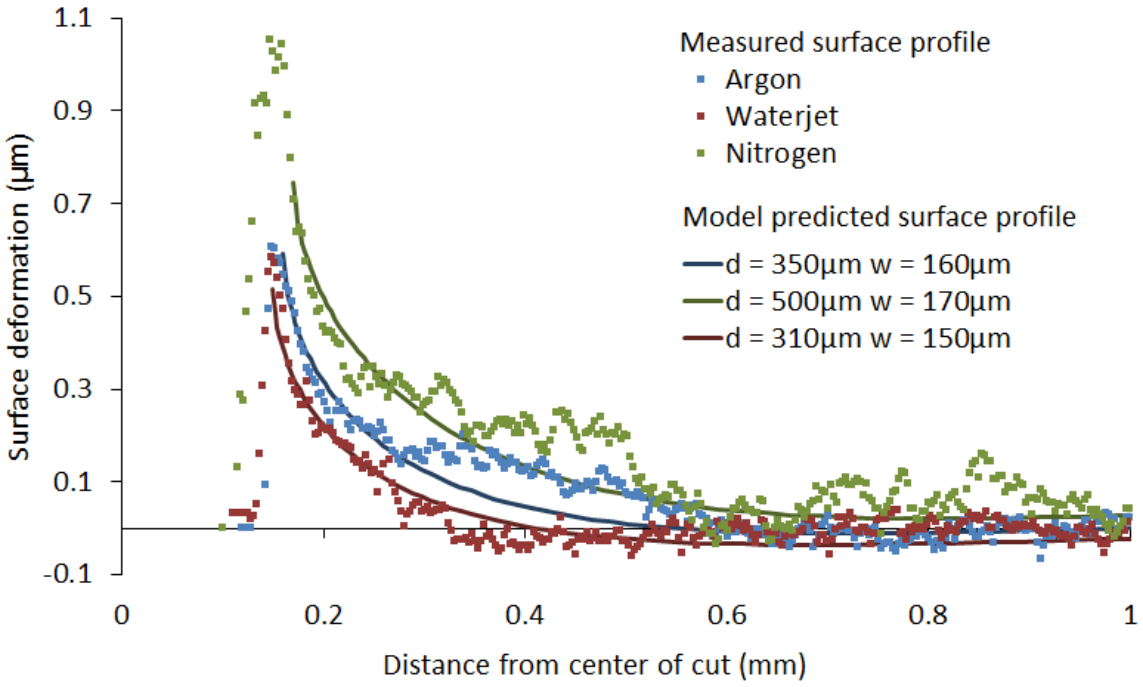

Figure 5.5. *Comparison of measured surface deformation with FEM model prediction*

Figure 5.5 also plotted numerical predicted surface deformation (solid curves) from model in Figure 2 that best describe the profiling measurement for the three assist media. This result corresponded to an expansion train of 0.007 for all the three specimens. The depth of the semi-elliptical transition zone were obtained from SEM images in Figure 5.3. The width of transition zone was assumed to be 0.15, 0.16 and 0.17mm through the comparison of measured profile.

The same expansion strain predicted for the three assist media implied the similar chemical reaction and phase transition happened during laser machining. This result agreed with Raman spectroscopy that similar peaks were detected from each transition zone of the three specimens. The major difference between assist media was found to be the energy coupling ability resulting in different penetration depth.

5.4.3 Fracture energy release rates for crack channeling

The estimated expansion strains and phase transition zone are utilized in the fracture model to determine the energy release rates for channeling cracks as a function of crack length. Figure 5.6 plotted the channeling energy release rate obtained by equation (1) representing the channeling energy release rate as a function of a/w (ratio of crack length to the thickness of material) for the three different assistant media. The fracture toughness range of PCBN reported as 7.7 - 10MPa m1/2 [14] was also plotted for determination of crack propagation behavior. Crack length was assumed to starting from value equal to transformation depth due to the localized damage and pre-cracks caused by laser irradiation inside phase transition zone. Energy release rate reach the highest for crack length just exceeding transformed depth due to the large tensile stresses induced by material expansion, and decreased as crack propagating deeper. For all the three specimens machined with different media, channeling fracture energy are higher than fracture toughness range for crack length across the whole thickness, meaning that the initial crack are expected to propagate under the driven force and create through-cut crack. Nitrogen assisted cutting induced more than twice of driving force over fracture toughness, which correspond to above analysis that Nitrogen coupled overdue amount of laser energy that lead to uncontrollable cracks. Argon demonstrated medium level driving force and waterjet induced threshold amount of fracture energy.

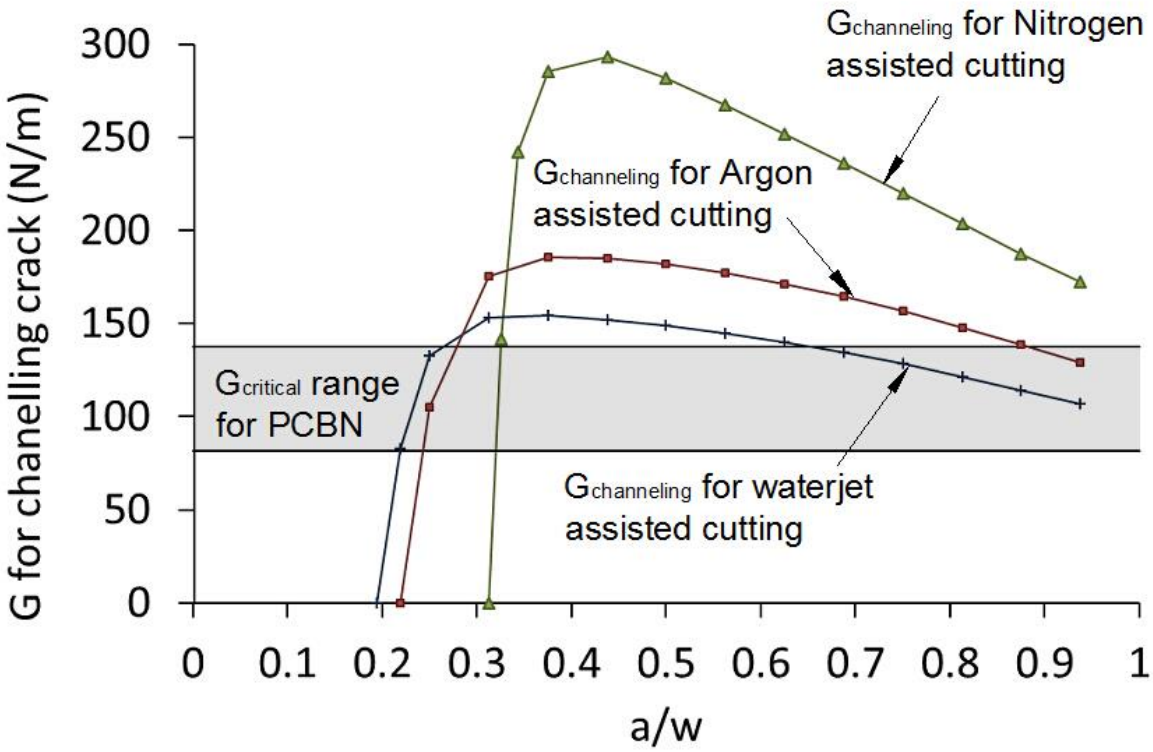

Figure 5.6. *Energy release rate of channeling crack machined by assist fluids of Nitrogen, Argon and waterjet*

The fracture modeling results match well with the experimental observations that all the three assisted media achieve through-cut of specimen. Nitrogen and Argon coupled more laser energy than needed that product rough cutting interface and deep transformation zone. Waterjet dissipated extra laser energy due to its rapid quenching effect that better controlled crack propagation and produced thin phase transition laser and better cut quality. These achievements enabled easier and low-cost post processing of tool inserts.

5.5 Summary

The effect of assist gas (Argon, Nitrogen) and water in CO2 laser machining of polycrystalline cubic boron nitride (75% c-BN and 25% Ti based matrix) was investigated.

Analysis of the observation revealed a two-step process consisting of phase transition of a thin surface layer of PCBN (h-BN and h-BNC)) and crack formation and propagation. SEM was used to characterize cut surface of machined area and cracked area (Figure 5.3) and Raman spectroscopy proved phase transition of machined area to sp2-bonded boron products while the cracked area retained the original cBN (Figure 5.4). FEA model was developed to simulate the influence of material phase transition with a semi-elliptical transformation zone near top surface undergoing uniform expansion. Surface profiles near cutting edges of the specimen cut with different assist media was measured using profilometry and compared with modeling result to estimate the expansion strain and dimensions of transformation region. Energy release rate was calculated based on the predicted expansion strain and transformation region and shows well agreement with observed cutting results. The cutting mechanism through a phase transition induced fracture propagation was proved. Nitrogen and Argon induced unfavorable phase transitions that did not offer controlled fracture mechanism and produced low surface roughness that do not make these assist gases suitable for the controlled crack separation. Water is an excellent candidate in producing threshold amount of phase transition with very thin layer as well as controlled cracking. Optimization of LWJ process is in order to further improve the process.

5.6 References

[1] R. S. Patel and M. Q. Brewster, "Gas-Assisted Laser-Metal Drilling: Experimental Results," Journal of Thermophysics and Heat Transfer, vol. 5, pp. 26-31, Jan 1991.

[2] D. K. Y. Low, L. Li, and A. G. Corfe, "The influence of assist gas on the mechanism of material ejection and removal during laser percussion drilling," Proceedings of the

Institution of Mechanical Engineers Part B-Journal of Engineering Manufacture, vol. 214, pp. 521-527, 2000.

[3] D. K. Y. Low, L. Li, and A. G. Corfe, "Effects of assist gas on the physical characteristics of spatter during laser percussion drilling of NIMONIC 263 alloy," Applied Surface Science, vol. 154, pp. 689-695, Feb 2000.

[4] D. Kalyanasundaram, G. Shehata, C. Neumann, P. Shrotriya, and P. Molian, "Design and validation of a hybrid laser/water-jet machining system for brittle materials," Journal of Laser Applications, vol. 20, pp. 127-134, May 2008.

[5] J. R. Rice, "A Path Independent Integral and Approximate Analysis of Strain Concentration by Notches and Cracks," Journal of Applied Mechanics, vol. 35, pp. 379-+, 1968.

[6] S. Ho and Z. Suo, "Tunneling Cracks in Constrained Layers," Journal of Applied Mechanics-Transactions of the Asme, vol. 60, pp. 890-894, Dec 1993.

[7] H. Sachdev, "Influence of impurities on the morphology and Raman spectra of cubic boron nitride," Diamond and Related Materials, vol. 12, pp. 1275-1286, Aug 2003.

[8] L. Song, L. J. Ci, H. Lu, P. B. Sorokin, C. H. Jin, J. Ni, et al., "Large Scale Growth and Characterization of Atomic Hexagonal Boron Nitride Layers," Nano Letters, vol. 10, pp. 3209-3215, Aug 2010.

[9] R. J. Nemanich, S. A. Solin, and R. M. Martin, "Light-Scattering Study of Boron-Nitride Micro-Crystals," Physical Review B, vol. 23, pp. 6348-6356, 1981.

[10] L. Ci, L. Song, C. H. Jin, D. Jariwala, D. X. Wu, Y. J. Li, et al., "Atomic layers of hybridized boron nitride and graphene domains," Nature Materials, vol. 9, pp. 430-435, May 2010.

[11] U. Kuhlmann and H. Werheit, "Raman Effect of Boron-Carbide (B4.3c to B10.37c)," Journal of Alloys and Compounds, vol. 205, pp. 87-91, Mar 1994.

[12] W. Steen, K. G. Watkins, and J. Mazumder, "Laser Material Processing," ed: Springer Science & Business Media, 2010, p. 131.

[13] S. Gloor, S. M. Pimenov, E. D. Obraztsova, W. Luthy, and H. P. Weber, "Laser ablation of diamond films in various atmospheres," Diamond and Related Materials, vol. 7, pp. 607-611, Feb 1998.

[14] M. P. DEvelyn and K. Zgonc, "Elastic properties of polycrystalline cubic boron nitride and diamond by dynamic resonance measurements," Diamond and Related Materials, vol. 6, pp. 812-816, Apr 1997.

CHAPTER VI

THE MECHANISM GOVERNING MACHINING OF POLYCRYSTALLINE DIAMOND (PCD) WITH LASER/WATERJET (LWJ) SYSTEM

Abstract

Polycrystalline diamond (PCD) is a popular tool material due to its ultra-high hardness and good chemical/thermal stability, and hence difficult to machine with traditional methods. This paper presents a novel material removal mechanism for cutting tungsten carbide (WC) supported PCD substrates by controlled crack propagation through both experimental and computational investigation. A hybrid CO2 laser/waterjet (LWJ) machining system with laser heating followed by waterjet quenching was utilized to conduct cutting experiments and the sample response transitioned from scribing to through-cut as laser line energy increases. Raman spectrometry and scanning electron microscopy (SEM) were performed on the cut surfaces to identify material separation mechanism. Finite element models were developed to predict surface deformation induced by graphitization and compared with surface profile measured from profilometry to estimate graphitization size and expansion strain. Fracture mechanics model was subsequently developed to compute energy release rate for cracks under different cutting line energies and validated with experimental observations. The experimentally validated model describing the cutting process relates processing parameters to the machining response of PCD-WC specimen and can be effectively used for guiding high-quality machining.

KEYWORDS: CO2 laser/waterjet machining (CO2-LWJ), Polycrystalline Diamond (PCD), controlled crack propagation

6.1 Introduction

Polycrystalline diamond (PCD) is a synthesized material that made by sintering randomly orientated diamond crystals[1] or converting from graphite at high temperature and high pressure[2]. It has superior mechanical and thermal properties such as high hardness, high strength, high wear resistance, strong corrosion resistance and good thermal conductivity. Because of these advantages, it has been widely used as cutting tools, drill bits and abrasives in various industries including automotive, aerospace, oil field and woodworking industries[3]. PCD blanks are usually available in two forms: a composite double-layer blank of a thin layer PCD backed on tungsten carbide(WC) substrate and unsupported solid piece of PCD with binder phases like cobalt[4].

PCD inserts have exceptional tool life but are difficult to machine. Traditional machining methods for PCD tools are grinding (mechanical and electrical) and electrical discharge machining (EDM). Both of them suffered from low material remove rates less than 2 mm^3/min) [5-7]. Moreover, EDM are constrained by the conductivity of machined material and therefore inefficient to machine low electrically conductive PCD structures (e.g. chemical vapor deposited diamond). Grinding machining also has drawbacks such as high cutting forces and high wheel costs. Nd:YAG Laser machining is an improved technique over EDM and grinding with a higher cutting speeds and narrow kerf. However, the material removal occurs through vaporization and melt blow can only produce shallow grooves each time and may require multiple passes for cutting of thick pieces. Harrison et al.[8] reported laser cutting of carbide supported PCD using nanosecond laser pulses at 1064 um wavelength

at low material removal rate of 7.6 mm^3/min. Okuchi, Takuo, et al.[9] investigated cutting of PCD with 355nm Nd:YAG Laser and found it's suitable only for thin samples with thickness less than 200 μm. Abrasive waterjet is another potential approach for cutting PCD that has been investigated by Axinte, D. A., et al.[10]. Their result shown that diamond abrasive can achieve a higher material removal rate of 249.9 mm^3/min for cutting PCD sample. However, drawbacks like high nozzle wear, high cost of abrasives and large kerf taper need to be addressed for implement in industry. In the cutting processes discussed above, the material removal is accomplished by material erosion (EDM/EDG), thermal evaporation (laser cutting) or mechanical wear (grinding and abrasive waterjet) that result in slow machining speeds.

In the current work, we investigate a hybrid machining method of PCD blanks that synergistically combines high-power CO2-laser and low-pressure abrasive-free waterjet. The CO2-Laser/waterjet machining (CO2-LWJ) [11, 12] system has been used in cutting low-conductive ceramic such as Alumina[13], Aluminum Nitride[14] and Zirconia[12] through thermal shock induced stress. It has also been applied to cut high-conductive material like Polycrystalline cubic boron nitride(PCBN)[15] and thin layer PCD specimen, but the cutting mechanism was not fully understood. In this paper, Raman spectroscopy, scanning electron microscopy (SEM) and optical profilometry were used to investigate cutting mechanism and characterize cutting quality. The cutting process was modeled using the finite element method and validated with measured surface deformation of the specimen. Fracture mechanics analysis of the cutting process was performed and compared with experimental observations. The results indicate that using the material removal mechanism of material separation through crack propagation, smaller kerf, parallel walls, higher speed and substantial energy savings can be achieved over conventional machining processes.

6.2 Cutting experiment and material characterization

The material used for cutting experiment was Tungsten Carbide (WC) supported PCD blanks with 8% cobalt as binder phase supplied by Diamond Innovations, Worthington, Ohio, USA. The blank was 1.6 mm thick disk of 58mm diameter with PCD layer of 0.5mm and WC layer of 1.1mm. The surface roughness of the received samples was 1.0 µm Ra and 1.3 µm RMS.

Cutting experiments on the PCD specimen were performed using a hybrid CO2-LWJ machining system. A continuous wave CO2 Laser (Model 820 Spectra Physics) of 10.6µm wavelength has been modified to accommodate the low-pressure waterjet. The laser beam was used for localized heating of the sample surface and the abrasive free waterjet is used to rapidly quench the heated area. Figure 6.1 presents the modified laser head with waterjet. The laser beam was transmitted through the middle nozzle and focused to a spot of 0.2 mm diameter on the sample surface. Waterjet was transported through the adjacent hole with a spacing of 6mm from laser beam to avoid direct contact and absorption. The pressure of waterjet was maintained at 410 kPa (60 psi). Air flow at a pressure of 34 kPa (5 psi) was transmitted surround laser beam through the same passage to protect the lens from damage due to spatter. A series of single-pass straight cutting experiments was carried out at two fixed laser power (P) of 1200W and 1500W with various cutting speeds of 8.5, 6.4, 4.2, 2.1 and 1.3 mm/s (200, 150, 100, 50 and 30 inch/min). Cutting experiment was repeated twice for the same processing parameters. Line energy P/v was utilized as a combined parameter to characterize energy input per unit length. The PCD blank was taped on a CNC controlled workstation. Laser beam was irradiated outside the PCD blank, translated through and stopped out of the other side. After

each cutting, the sample surface was carefully examined and fracture behaviors (through-cut/scribing) were recorded.

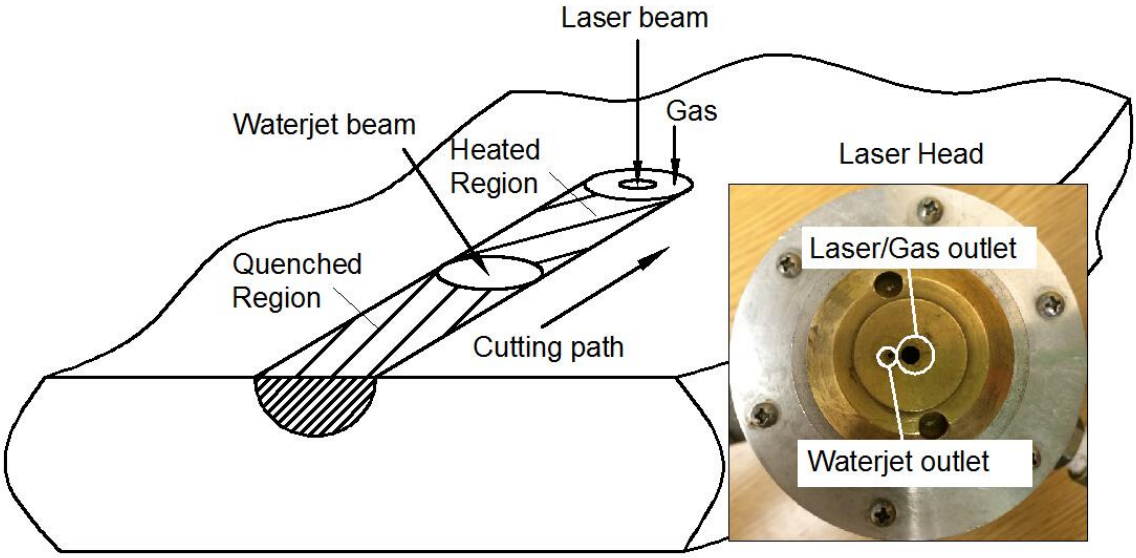

Figure 6.1. *Laser/Waterjet(LWJ) machining system*

Surface profiles around each cutting kerf were measured using optical profilometry (Zygo NewView 7100). 3D topographic information of the top surfaces was gathered and the height distribution along the cutting path was averaged to characterize deformation induced by LWJ machining. Raman spectroscopy (Renishaw-inVia Raman Microscopy) with Ar-ion laser at a wavelength of 488nm was utilized to determine the phases change of the LWJ machined region. Scanning electron microscopy (SEM Model JEOL JSM-606LV at 20 kV) was used to inspect the cut surface in order to identify the depth of phase transformation zone.

6.3 Numerical modeling and validation

Diamond could convert to graphite at high temperatures. Davies & Evans [16] reported graphitization of diamond at zero pressure would happen as temperature approach 1500 ℃ and become rapid at 2100 ℃. Melting temperature of graphite would start at about 3700 ℃(4000K)[17]. Transformation of diamond (sp3-bonded tetrahedral lattice) to graphite (sp2-bonded hcp lattice) is associated with large volumetric expansion[18]. In current work, this transformation was achieved by Laser/Waterjet(LWJ) machining, which created tensile stresses in the surrounding material. The stresses helped propagate the crack through the whole thickness that achieved material separation. Fracture mechanics analysis was performed to determine the driving forces (energy release rate) for cracks caused by LWJ machining at different line energies.

6.3.1 Finite element model for determination of transformation zone and expansion strain

Finite element model was developed in ABAQUS (Simulia, Providence, RI) to estimate the phase transformation volume and associated expansion strain. Figure 6.2(a) schematically represents the graphitization zone of a semi-elliptical cylinder subjected to uniform expansion along the laser/waterjet cutting path. The cross-section was characterized by a semi-elliptical shape to approximate the effect of the Gaussian laser beam. Due to the long cutting path, the model could be simplified to 2D plane strain state of a cross-section perpendicular to the machining direction as shown in Figure 6.2(b). Laser beam was symmetric distributed, therefore only half of the specimen was modeled with zero displacement in horizontal direction on the axis of symmetry. Zero displacement in vertical direction was applied on outer edge of the model to simulate support of the table. The model was composed

of 8-noded quadratic plane strain elements with refined mesh in the transformation zone. Material properties of graphite, PCD and tungsten carbide were assigned respectively to the semi-elliptical zone, PCD layer and Carbide layer. Calculation of surface deformation was performed for different values of transformation depth and width undergoing constant expansion strain. The modeling results were subsequently compared with surface profiling measurements of each cutting kerf to estimate size of transformation zone and expansion strain associated with each cutting line energy.

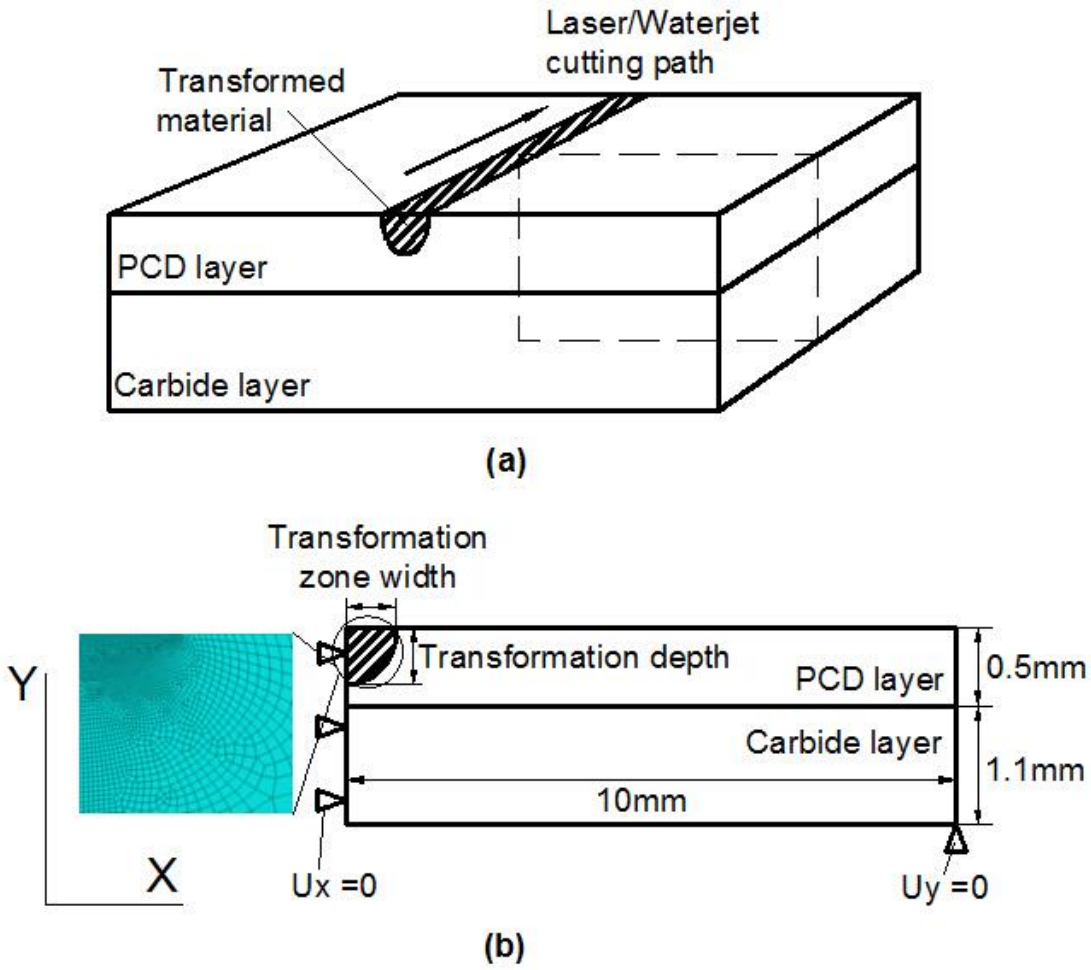

Figure 6.2. *(a) Schematic diagram of the workpiece machined by LWJ beam (b) Plane strain finite element model and boundary conditions for predicting sample deformation*

6.3.2 Fracture mechanics analysis of cracks

Laser irradiation and waterjet quenching not only transforms material but also causes localized damage that results in crack nucleation and propagation. At the beginning of each cutting, LWJ beam initiated a crack across the edge of specimen. As laser beam moved in, the existing crack extended towards both the thickness direction and channeled along cutting direction as schematically shown in Figure 6.3(a). Crack propagation analysis was performed in three steps: (1) 2D plane strain model as represented in Figure 6.3(b) was developed to evaluate fracture energy release rate at different crack depths; (2) crack channeling is analyzed by integrating and averaging plain strain energy release rates over all the crack depths; (3) computed channeling fracture energy was compared to critical energy release rate weighted for the double-layer PCD-WC specimen to predict fracture behaviors.

Plane strain fracture model (Figure 6.3(b)) was built in ABAQUS with application of transformation zone and expansion strain obtained from model in Figure 6.2. A seam crack with depth "a" was created through center of the transformation zone with contacting constrains applied on crack edge. Crack depth was varied from a value equal to transformation depth to the whole thickness. Fracture energy release rate was calculated for different crack depths through J-integral evaluation developed by Cherepanoy[19] and Rice[20]. J-integral is a path-independent contour integral that is equal to the fracture energy release rate for extreme brittle materials such as PCD and WC. The meshes for each model were refined at crack tip till J-integral values reached equilibrium on multiple contours. In this way, energy release rates as a function of crack depths can be obtained to predict crack propagation behavior.

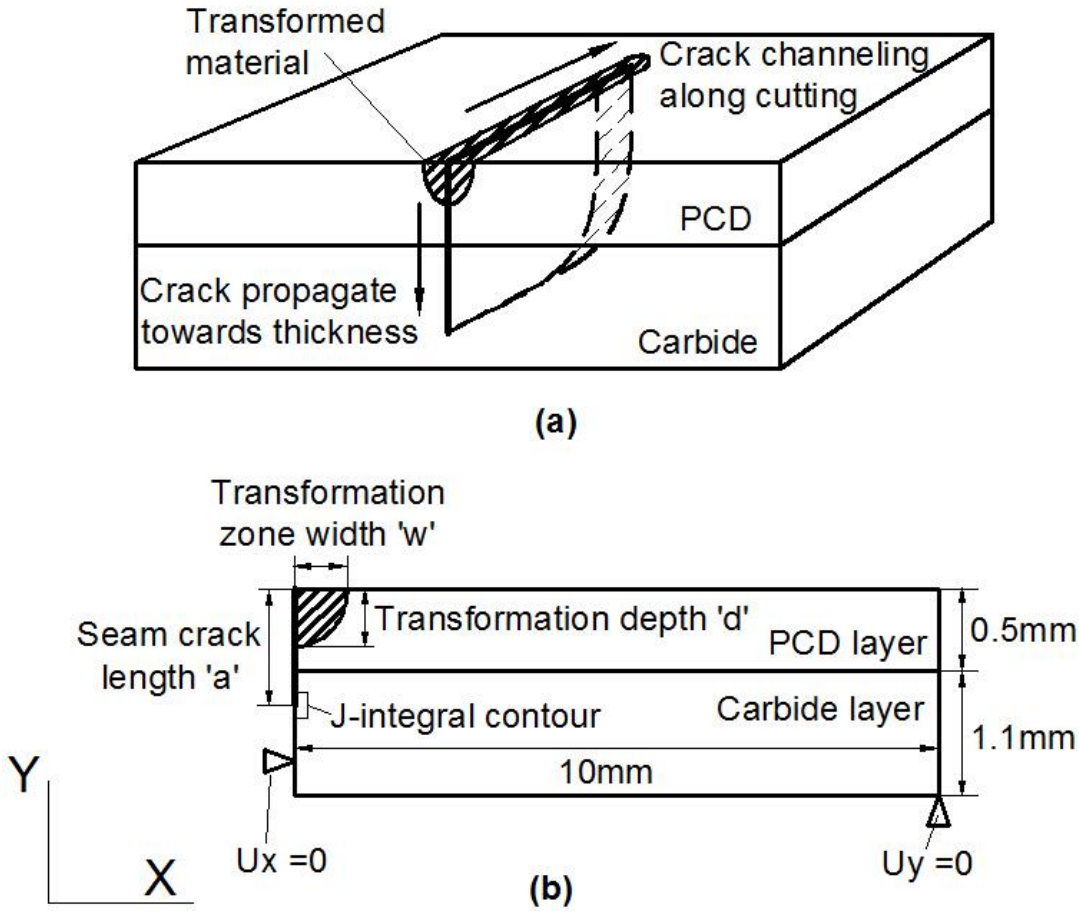

Figure 6.3. *(a) Crack configurations (b) Plane strain finite element model and boundary conditions for evaluation energy release rate at different crack lengths*

Crack channeled along the cutting path was analyzed based on the method of Ho and Suo [21]. Figure 6.3(a) demonstrates the configuration of channeling crack. It is based on the assumption that the existing plane strain crack propagated at a fixed depth and a constant tip shape. Therefore, crack tip advances a unit distance is equal to removing a unit slice far ahead of the crack tip and attaching a unit slice with plane strain crack far behind the crack tip. Energy release rate is only a function of crack depth and can be obtained by integrating the plain strain energy release rates over the crack.

$$G_{channeling} = \frac{1}{a}\int_0^a G(a')\,da' \quad (6.1)$$

Where $G(a')$ is the fracture energy for plane strain cracks of different crack depths.

Critical fracture energy release rate G_{IC} for linear-elastic materials was computed from their fracture toughness K_{IC} with relationship $G_{IC} = {K_{IC}}^2/E$. The balanced energy requirement for crack channeling in double-layer materials was calculated following Ye, Suo and Evans[22] as:

$$G_{IC} = h\Gamma_{PCD} + (a - h)\Gamma_{WC} \quad (6.2)$$

Where Γ_{PCD} and Γ_{WC} are critical fracture energy release rate respectively for PCD and WC. a is the crack length and h is the thickness of PCD layer.

6.4 Results and discussion

6.4.1 LWJ cutting result and material testing

The laser/waterjet cutting experiments were performed for a range of velocities at fixed laser power of 1200W and 1500W. For the laser power of 1200W, LWJ beam produced no scribing or grooves but changed color of the sample surface at all the cutting speeds. For the laser power of 1500W, scribing was observed at higher velocities and through-cutting was observed at lower velocities. Top view of machined PCD-WC specimen at speeds of 8.5, 6.4, 4.2, 2.1 and 1.3 mm/s are represented in Figure 4 which corresponds to laser line energies of 177, 236, 354, 708, 1181J/mm. For line energy higher than 354J/mm, LWJ machining produced only narrow grooves with a black zone around it. As lines energy increasing to 708J/mm, spalling of material around cutting groove was observed and resulted in localized damage to sample surface. A transition from scribing to controlled separation was observed at line energy of 1181J/mm with more amount of material spalling.

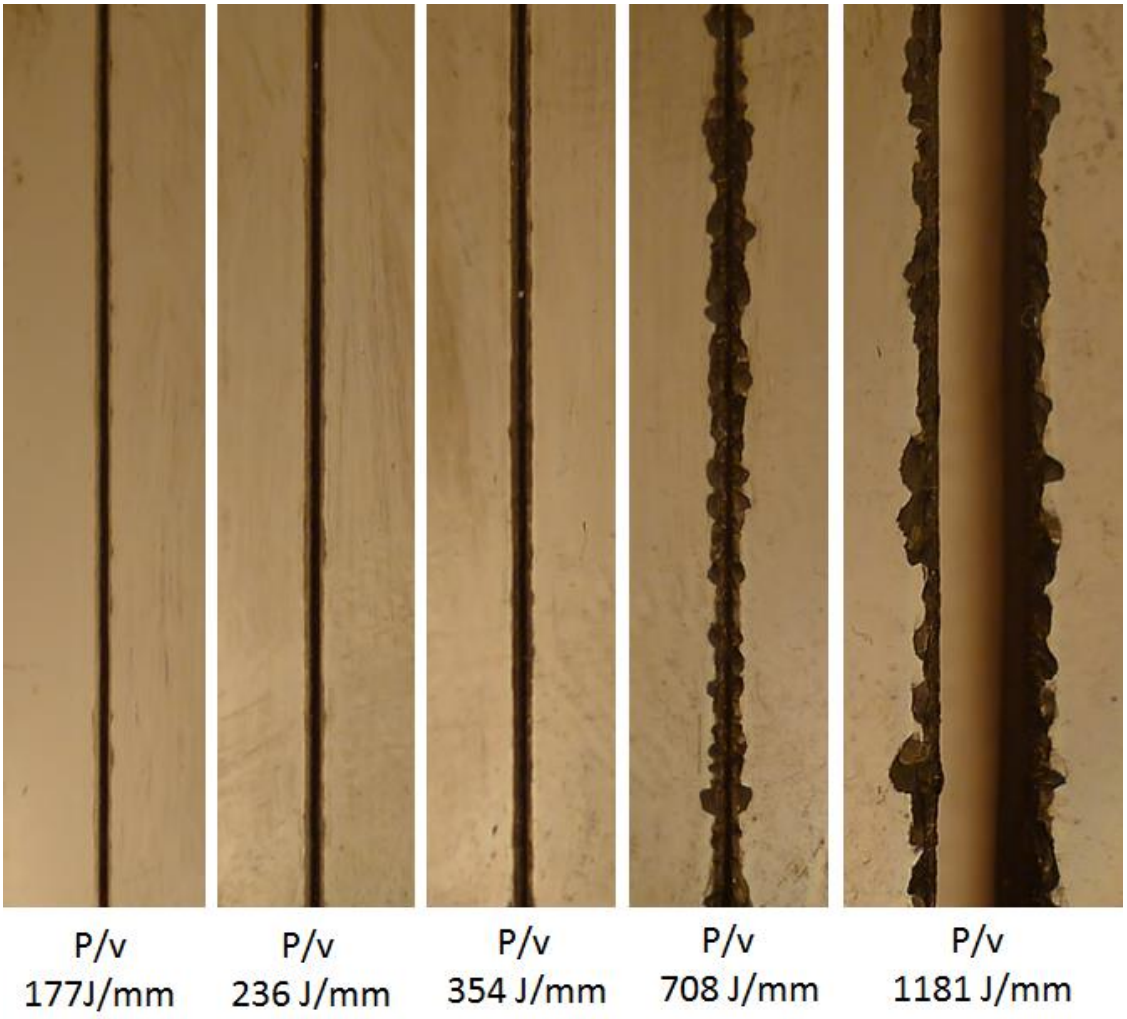

Figure 6.4. *Top view of machined PCD-WC specimen at line energies of 177, 236, 354, 708, 1181J/mm for laser power of 1500W*

Scanning electron microscopy (SEM) and Raman spectroscopy were used for inspecting specimen and identifying cutting mechanism. Figure 6.5(a) represents SEM image of the transverse cross-section of the specimen cut at line energy of 1181J/mm. The cross-section displays two colors representing PCD layer (top black) and WC layer (bottom white). The PCD layer performed non-uniform microstructures that can be divided into two areas with different surface morphologies. Raman spectroscopy measurements were taken from the two areas on the cut cross-section as well as from the black zone around cut grooves on sample

surface. Result are plotted in Figure 6.5(b). The black zone on sample surface and top area on cross-section represent only graphite phase of two peaks around 1357 and 1580 cm-1 [23]; while the lower area of PCD layer represents only a peak at 1332 cm-1 corresponding to diamond phase [23]. The same peak was found in the as-received material.

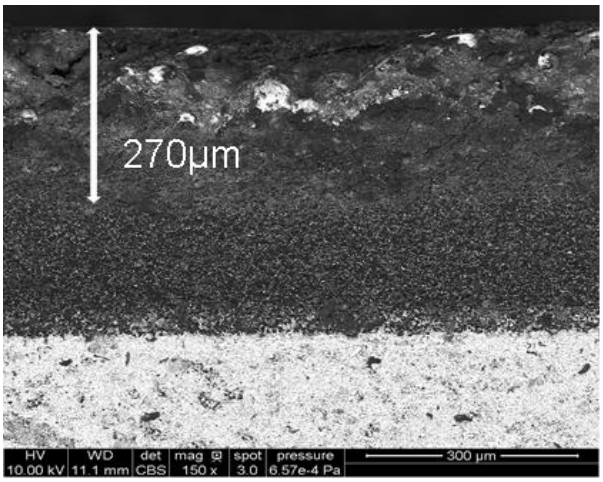

(a)

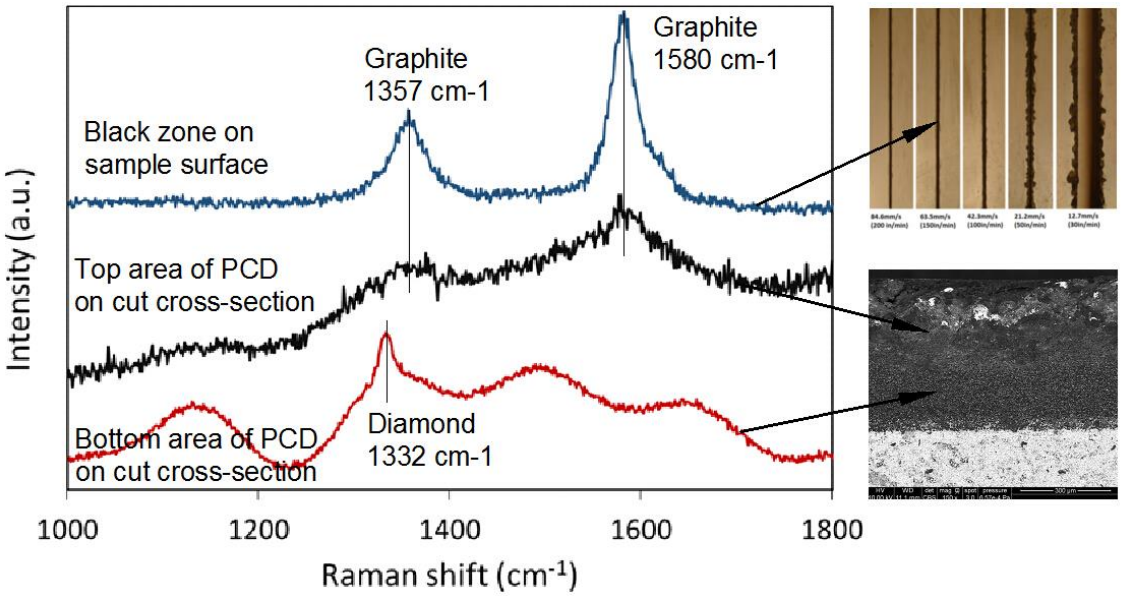

(b)

Figure 6.5. *(a) SEM of cross-section for the through-cut PCD specimen (b) Raman spectrum of black zone on sample surface, top area and lower area on cut cross-section*

It has been shown previously that the different modes of laser/LWJ machining of alumina [13, 24] was a function of line energy (ratio of laser power to velocity of machining table). However, in the present case similar material separation was not noticed for the same line energy for laser power of 1200W. This is due to the low absorption of diamond at wavelength of 10.6 μm of the CO2 laser[25]. As laser power increased to 1500W, energy input was sufficient to transform localized PCD into graphite and hence absorbed more laser energy as graphite has a higher absorptivity. It is also reported that the metal binder (cobalt) is able to assist in graphitization [2]. The SEM and Raman spectroscopy results proved the phase transformation of the region around the cutting kerf. The depth of graphitization zone for the through-cut sample can be measured from the SEM image (270 μm reading from Figure 6.5(a)). The region below that has the same composition as the original material that was formed due to propagation of cracks through the thickness.

6.4.2 Surface profiling measurement and comparison with modeling deformation

3D topographies of top surface adjacent to the cutting grooves were measured using optical profilometry for determination of the surface deformation after LWJ machining. Measurements were taken from an area of 1.8mm width along each cutting line and height distribution perpendicular to the cut was averaged to determine the representative surface deformation. Result are valid only for the scribing cuts at lower line energies of 177, 236 and 354J/mm while failed for the spalling cuts at 708 and 1181 J/mm. Figure 6.6 demonstrated detailed measurement procedure. The surface profiles were found to be nearly symmetric about the cutting center, therefore average of the two sides are computed to characterize the overall deformation. It can be observed from Figure 6.6 that height and width of deformed surface

increased as line energy getting higher. Groove widths are slightly larger than laser beam radius of 0.1 mm and increase with line energies as well.

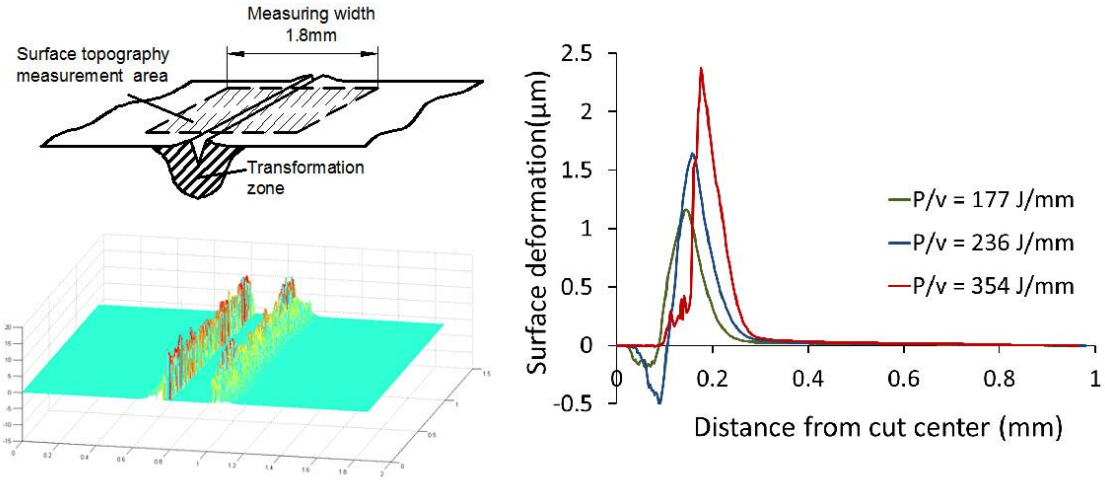

Figure 6.6. *Measurement of surface deformation*

Figure 6.7 plotted comparison of measured surface deformation (scattered curves) with numerical predictions (solid curves) calculated from model in Figure 6.2. The transformation depth and width of the model found through the comparison were 60 and 250 μm for the lowest line energy of 177J/mm, and 75 and 260 μm for the second lowest line energy of 236J/mm, and 100 and 270 μm for middle line energy of 354J/mm. All the modeling results were computed based on a constant expansion strain of 1.7%. The function between dimensions of transformation zone (depth and width) and laser line energy is plotted in Figure 8 which display a linear relationship.

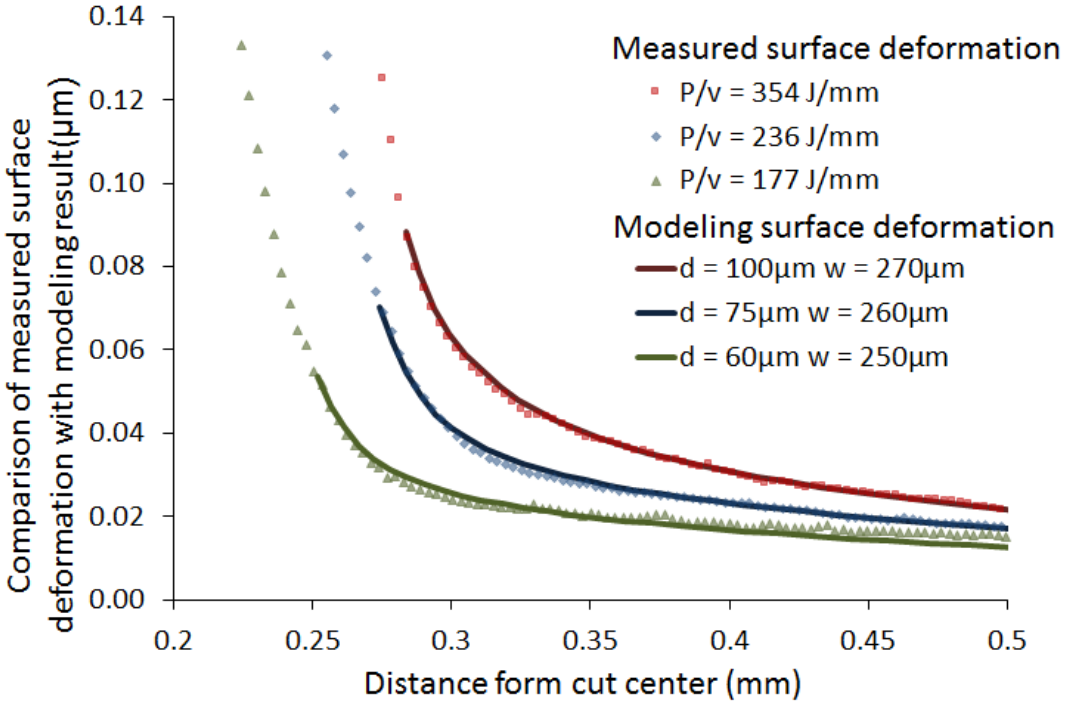

Figure 6.7. *Comparison of measured surface deformation with FEM modeling prediction*

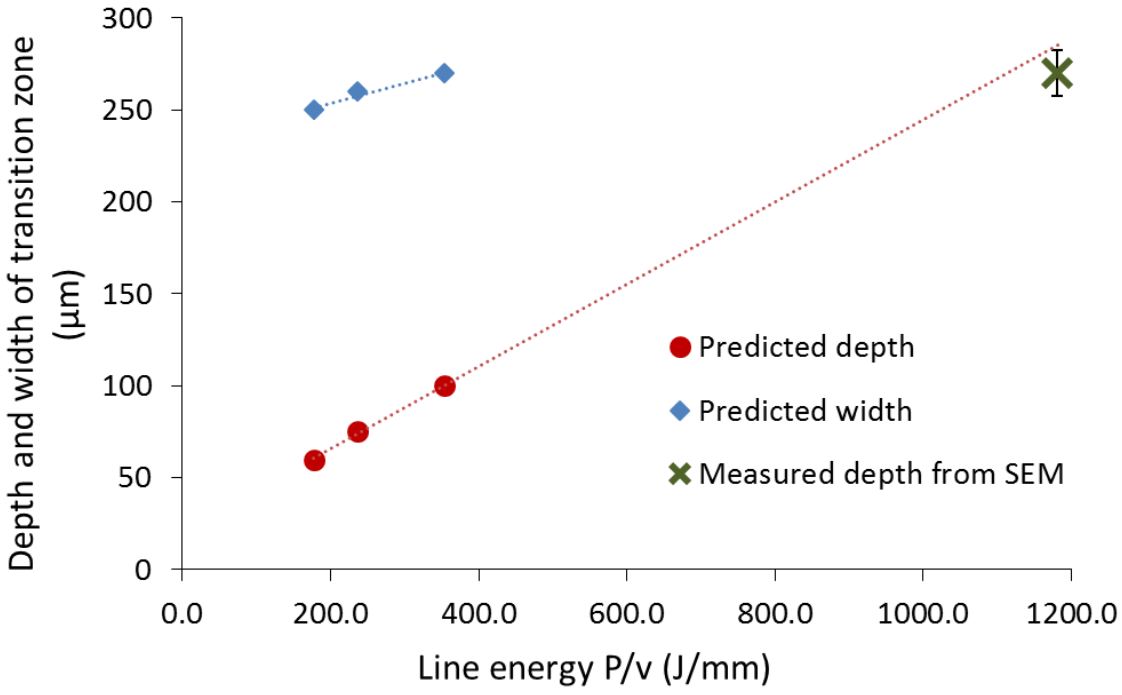

Figure 6.8. *Relationship between line energy and depth/width of transformation zone*

The linear relationship represented in Figure 6.8 relates the LWJ cutting parameters (line energy) to the size of the transformation zone subjected to a constant expansion strain. This relationship can be used to approximate the transformation size at other line energies where surface deformation measurements cannot be performed (for example: sample cut at 708J/mm and 1181J/mm). For the completely separated specimen, depth of transformed zone can be measured from the transverse SEM image as shown in Figure 6.5(a). The measurement was taken from 5 locations and the averaged value with error bar was also plotted in Figure 6.8. Good agreement between the measured and predicted transformation depth indicates that modeling assumptions and simplifications are appropriate to describe the actual situation.

6.4.3 Energy release rates for crack propagation

The channeling energy release rate at cutting line energies of 708J/mm and 1181J/mm were computed based on the model in Figure 6.3. The transformation depth and width was estimated using the linear relationship demonstrated in Figure 6.8 and found to be 180 μm for line energy of 708J/mm and 280 μm for line energy of 1181J/mm. The expansion strain was 1.7% as found from the comparison of surface deformation. Channeling energy release rate at different crack depths were determined using equation (1) and the critical energy requirement for the PCD-WC specimen was obtained by equation (2). Figure 6.9 plotted both the channeling energy and the critical energy release rates range as a function of non-dimensional crack depth (crack depth/specimen thickness). The critical energy release rate range was computed from reported fracture toughness of polycrystalline diamond as 3-6 MPa$\sqrt{m}$ [26]. The channeling energy curve starts from a crack equal to the transformation depth and increases as crack propagating due to the large tensile stresses outside the transformation zone induced from material expansion. Channeling energy release rates at all crack depths

corresponding to line energy of 708J/mm are lower than the critical range suggesting that under this processing condition stress field is not sufficient to propagate the channeling cracks. This prediction agrees well with the cutting observation that 708J/mm only performed scribing rather than material separation. Channeling energy release rates at all crack depths for cutting line energy of 1181J/mm is higher than the critical range suggesting that cracks are expected to propagate along the laser path through the whole thickness. This line energy corresponds to the complete separation shown in Figure 6.5(a).

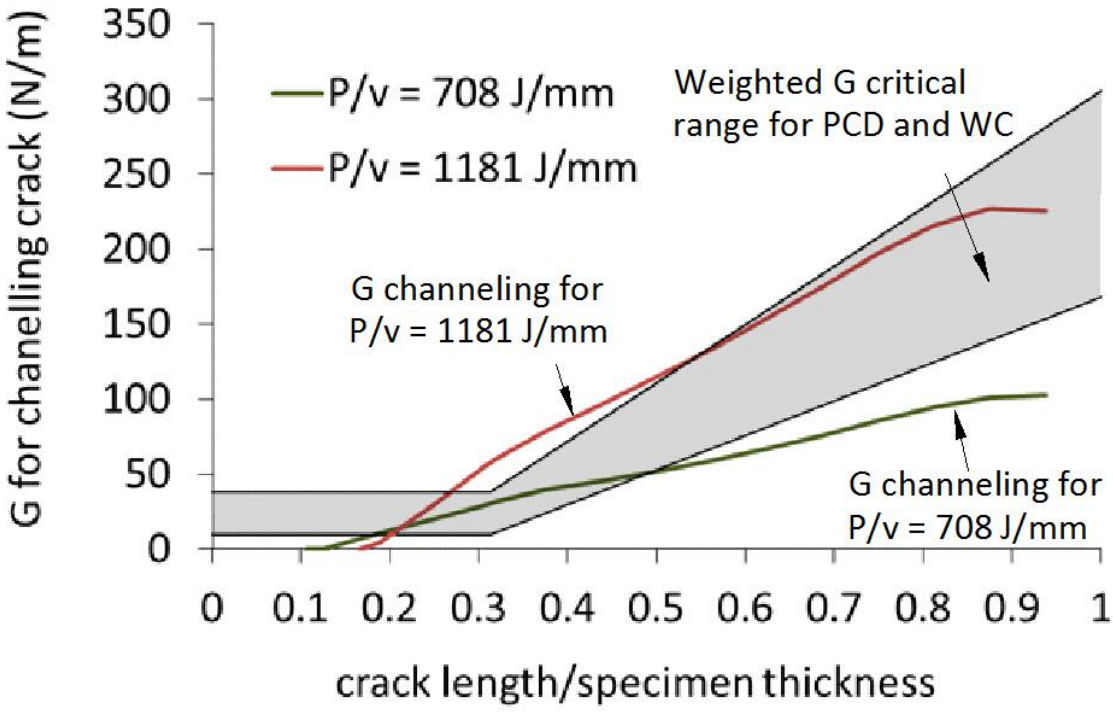

Figure 6.9. *Energy release rate for channeling crack*

6.5 Conclusions

The hybrid CO2-Laser/Waterjet(LWJ) machining system is used for cutting carbide supported PCD blanks and the effect of processing parameters and line energy requirement was studied through design of cutting experiments. At laser power of 1500W, five line energies were used in the cutting and a transition from scribing to through-cut was observed as line energy increased. Cutting speed was improved for an order of magnitude compared to traditional method such as EDM.

Cutting mechanism of graphitization induced fracture propagation was identified through SEM and Raman tests. SEM image of the transverse cross-section of the through-cut specimen indicates two types of microstructures of PCD. Raman spectroscopy taken on the two zones revealed that LWJ beam transformed a small region near top surface into graphite and the region below that was still PCD. These facts suggested the cutting mechanism as described below: Laser irradiation and waterjet quenching leads to scoring on the sample surface and graphitization of diamond along cutting path. Graphite occupies more volume than diamond, which results in constrained expansion and development of tensile stresses in the surrounding materials. The stresses drive the laser machined groove propagate through the thickness and separate the specimen.

Finite element modeling of the transformation induced surface deformation and energy release rates for cracks is utilized to validate the proposed mechanism. Surface deformation was measured using optical profilometry and compared with FEA results. It is found from the comparison that transformation zone depth increases linearly with laser line energy. Graphitization induced volumetric changes could be modeled using a semi-elliptical zone undergoing uniform volumetric expansion strain of 1.7%.

Close agreement was achieved through comparing numerical predictions with experimental observations. These results suggest that graphitization induced fracture is an efficient mechanism and the model could be used as a guide to control processing parameter for improving cutting quality.

6.6 References

[1] D. R. Hall, "Composite polycrystalline diamond compact," U.S. Patent US4604106 A, Aug 5, 1986.

[2] T. Irifune, A. Kurio, S. Sakamoto, T. Inoue, and H. Sumiya, "Materials - Ultrahard polycrystalline diamond from graphite," *Nature*, vol. 421, pp. 599-600, Feb 6 2003.

[3] M. W. Cook and P. K. Bossom, "Trends and recent developments in the material manufacture and cutting tool application of polycrystalline diamond and polycrystalline cubic boron nitride," *International Journal of Refractory Metals & Hard Materials*, vol. 18, pp. 147-152, 2000.

[4] H. Katzman and W. F. Libby, "Sintered Diamond Compacts with a Cobalt Binder," *Science*, vol. 172, pp. 1132-&, 1971.

[5] Y. H. Liu, Y. F. Guo, and J. C. Liu, "Electric discharge milling of polycrystalline diamond," *Proceedings of the Institution of Mechanical Engineers Part B-Journal of Engineering Manufacture*, vol. 211, pp. 643-647, 1997.

[6] D. Wang, W. S. Zhao, L. Gu, and X. M. Kang, "A study on micro-hole machining of polycrystalline diamond by micro-electrical discharge machining," *Journal of Materials Processing Technology*, vol. 211, pp. 3-11, Jan 1 2011.

[7] Z. B. Zhan, L. Li, N. He, and R. Shrestha, "An experimental study on grinding parameters for manufacturing PCD micro-milling tool," *International Journal of Advanced Manufacturing Technology,* vol. 73, pp. 1799-1806, Aug 2014.

[8] P. M. Harrison, M. Henry, and M. Brownell, "Laser processing of polycrystalline diamond, tungsten carbide, and a related composite material," *Journal of Laser Applications,* vol. 18, pp. 117-126, May 2006.

[9] T. Okuchi, H. Ohfuji, S. Odake, H. Kagi, S. Nagatomo, M. Sugata, *et al.*, "Micromachining and surface processing of the super-hard nano-polycrystalline diamond by three types of pulsed lasers," *Applied Physics a-Materials Science & Processing,* vol. 96, pp. 833-842, Sep 2009.

[10] D. A. Axinte, D. S. Srinivasu, M. C. Kong, and P. W. Butler-Smith, "Abrasive waterjet cutting of polycrystalline diamond: A preliminary investigation," *International Journal of Machine Tools & Manufacture,* vol. 49, pp. 797-803, Aug 2009.

[11] D. Kalyanasundaram, G. Shehata, C. Neumann, P. Shrotriya, and P. Molian, "Design and validation of a hybrid laser/water-jet machining system for brittle materials," *Journal of Laser Applications,* vol. 20, pp. 127-134, May 2008.

[12] D. Kalyanasundaram, P. Shrotriya, and P. Molian, "Fracture mechanics-based analysis for hybrid laser/waterjet (LWJ) machining of yttria-partially stabilized zirconia (Y-PSZ)," *International Journal of Machine Tools & Manufacture,* vol. 50, pp. 97-105, Jan 2010.

[13] C. Barnes, P. Shrotriya, and P. Molian, "Water-assisted laser thermal shock machining of alumina," *International Journal of Machine Tools & Manufacture,* vol. 47, pp. 1864-1874, Oct 2007.

[14] R. Molian, P. Shrotriya, and P. Molian, "Thermal stress fracture mode of CO2 laser cutting of aluminum nitride," *International Journal of Advanced Manufacturing Technology,* vol. 39, pp. 725-733, Nov 2008.

[15] Z. Wu, A. A. Melaibari, P. Molian, and P. Shrotriya, "Hybrid CO 2 laser/waterjet (CO 2-LWJ) cutting of Polycrystalline Cubic Boron Nitride (PCBN) blanks with phase transformation induced fracture.," *Optics & Laser Technology,* vol. 70, pp. 39-44, 2015.

[16] G. Davies and T. Evans, "Graphitization of Diamond at Zero Pressure and at a High-Pressure," *Proceedings of the Royal Society of London Series a-Mathematical and Physical Sciences,* vol. 328, pp. 413-&, 1972.

[17] F. P. Bundy, "The P, T Phase and Reaction Diagram for Elemental Carbon, 1979," *Journal of Geophysical Research,* vol. 85, pp. 6930-6936, 1980.

[18] F. P. Bundy, H. M. Strong, H. P. Bovenkerk, and R. H. Wentorf, "Diamond-Graphite Equilibrium Line from Growth and Graphitization of Diamond," *Journal of Chemical Physics,* vol. 35, pp. 383-&, 1961.

[19] Cherepan.Gp, "Crack Propagation in Continuous Media," *Journal of Applied Mathematics and Mechanics-Ussr,* vol. 31, pp. 503-&, 1967.

[20] J. R. Rice, "A Path Independent Integral and Approximate Analysis of Strain Concentration by Notches and Cracks," *Journal of Applied Mechanics,* vol. 35, pp. 379-+, 1968.

[21] S. Ho and Z. Suo, "Tunneling Cracks in Constrained Layers," *Journal of Applied Mechanics-Transactions of the Asme,* vol. 60, pp. 890-894, Dec 1993.

[22] T. Ye, Z. Suo, and A. G. Evans, "Thin-Film Cracking and the Roles of Substrate and Interface," *International Journal of Solids and Structures,* vol. 29, pp. 2639-2648, 1992.

[23] R. J. Nemanich, J. T. Glass, G. Lucovsky, and R. E. Shroder, "Raman-Scattering Characterization of Carbon Bonding in Diamond and Diamondlike Thin-Films," *Journal of Vacuum Science & Technology a-Vacuum Surfaces and Films,* vol. 6, pp. 1783-1787, May-Jun 1988.

[24] D. Kalyanasundaram, P. Shrotriya, and P. Molian, "Obtaining a Relationship Between Process Parameters and Fracture Characteristics for Hybrid CO(2) Laser/Waterjet Machining of Ceramics," *Journal of Engineering Materials and Technology-Transactions of the Asme,* vol. 131, Jan 2009.

[25] C. D. Clark, R. W. Ditchburn, and H. B. Dyer, "The Absorption Spectra of Natural and Irradiated Diamonds," *Proceedings of the Royal Society of London Series a-Mathematical and Physical Sciences,* vol. 234, pp. 363-381, 1956.

[26] D. Miess and G. Rai, "Fracture toughness and thermal resistance of polycrystalline diamond compacts," *Materials Science and Engineering a-Structural Materials Properties Microstructure and Processing,* vol. 209, pp. 270-276, May 1996.

CHAPTER VII

ATOMIC STUDY OF NANO-TWINNED CBN AND LAMELLA CBN/WBN MICROSTRUCTURES

Abstract

A novel heat treatment process involving surface heating using a continuous wave CO_2 laser followed by tandem waterjet quenching of the laser beam path was applied to increase the hardness of a dual phase cBN/wBN specimen(50% cBN and 50% wBN). The hardness has been improved by 100% in this specimen (nominal 75 GPa) and has almost reached the hardness of a typical polycrystalline diamond (65-80 GPa). The specimen before and after LWJ heat treatment has been investigated by Raman spectroscopy, high resolution scanning electron microscopy and X-ray diffraction to study the phase transformation and microstructure change. A micro-band cBN/wBN lamella structure was found in the untreated specimen. Atomic simulations are performed to study the nanotwinned cBN and cBN/wBN lamella structures. Shearing and indentation shearing are performed in LAMMPS to analyze strength as a function of grain size that possibly result in hardness increase

KEYWORDS: Composite wBN/cBN, Laser Heat Treatment, Hardness improvement, nanotwinned cBN, Microstructure

7.1 Introduction

Is was recently found in our group that the laser heat treatment of the dual phase wBN/cBN has almost doubled the hardness and matched with that of PCD[1]. The average

hardness was increased by 100% in wBN/cBN treated with a single pass LWJ beam. Results are represented in Figure 7.1.

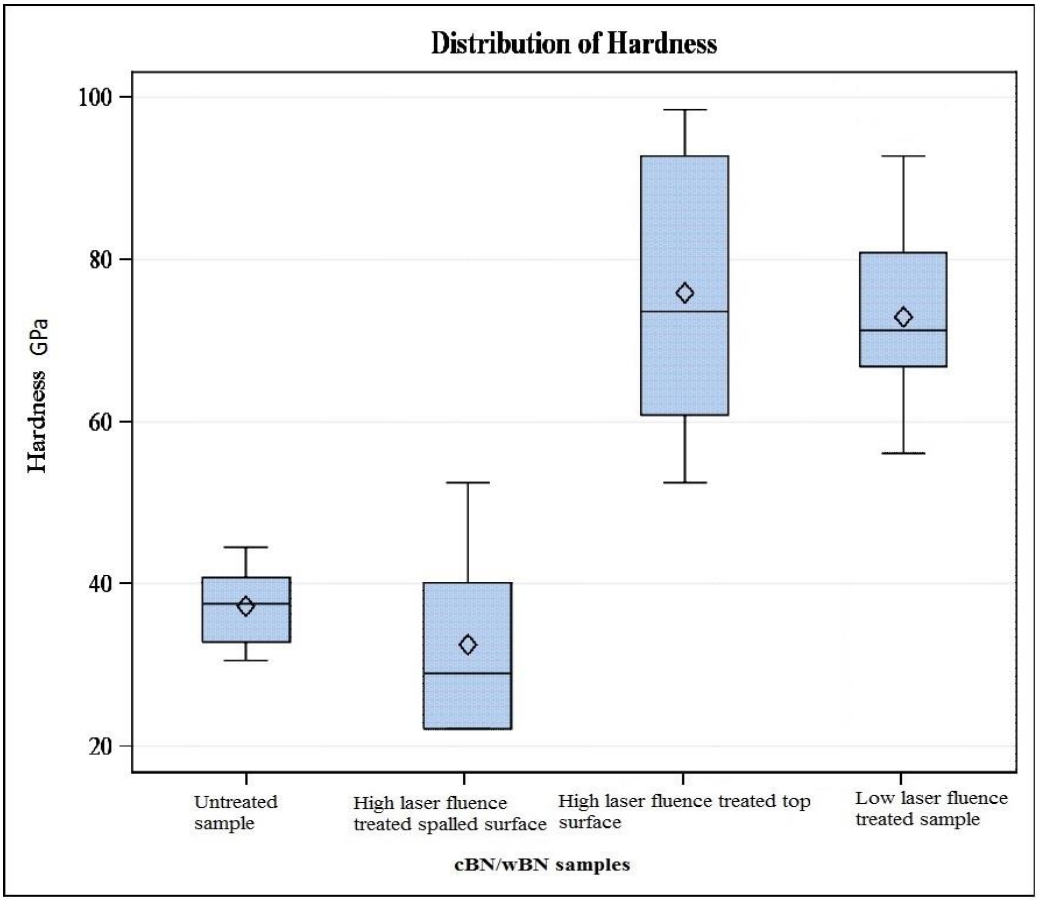

Figure 7.1. *Hardness of wBN/cBN composite before and after LWJ heat treatment*

XRD analysis was performed on specimen before and after the LWJ treatment and did not show any major difference. In both cases, it shows that the composite is a multiphase material with wBN and cBN being the dominant phases. This result excludes the possibility that the hardness increase is due to the material's phase transition. The microstructure of the sample before heat treatment was studied using HRSEM (high resolution scanning electron microscopy) and TEM (Transmission electron microscopy). The microstructure consists of two types of structures with different sizes and morphologies. The first type is lamellas of 0.5-

2 μm in length and 0.15-0.2 μm in thickness (Figure 7.2). Two features can be distinguished: regular band contract across the thickness (Figure 7.3) and interfaces at which the fragmentation takes place (Figure 7.2). The second type of structure is the independent grains with polyhedral faceting. Such polyhedral grains have the particle size of 0.1-0.2 μm (Figure 7.3). Their most common location is at the fragmentation sites and interfaces inside the lamellas. Lamella/polyhedron and polyhedron/polyhedron interfaces have both straight-line boundaries which result in formation of pores (Figure 7.3).

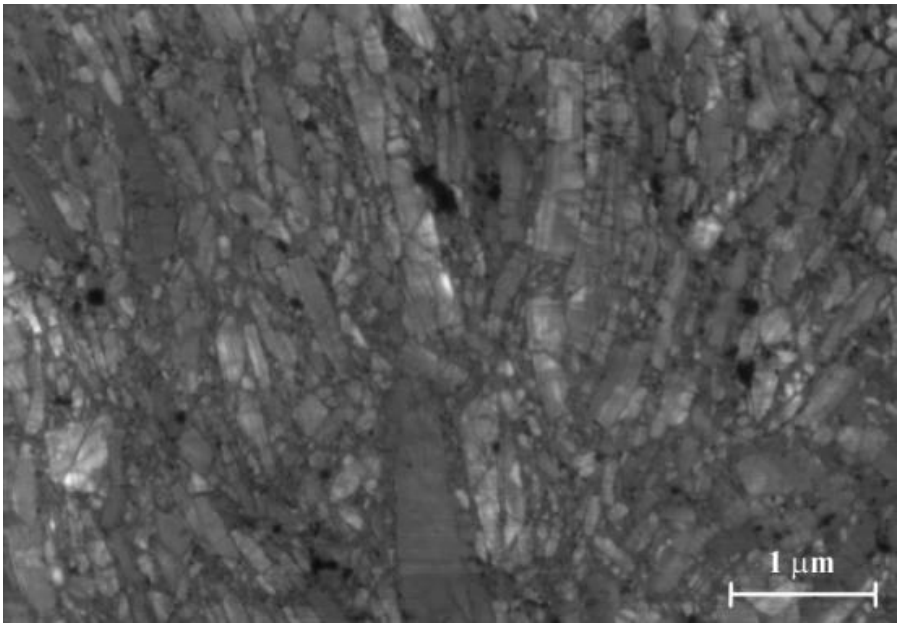

Figure 7.2. Microstructure of untreated wBN/cBN composite

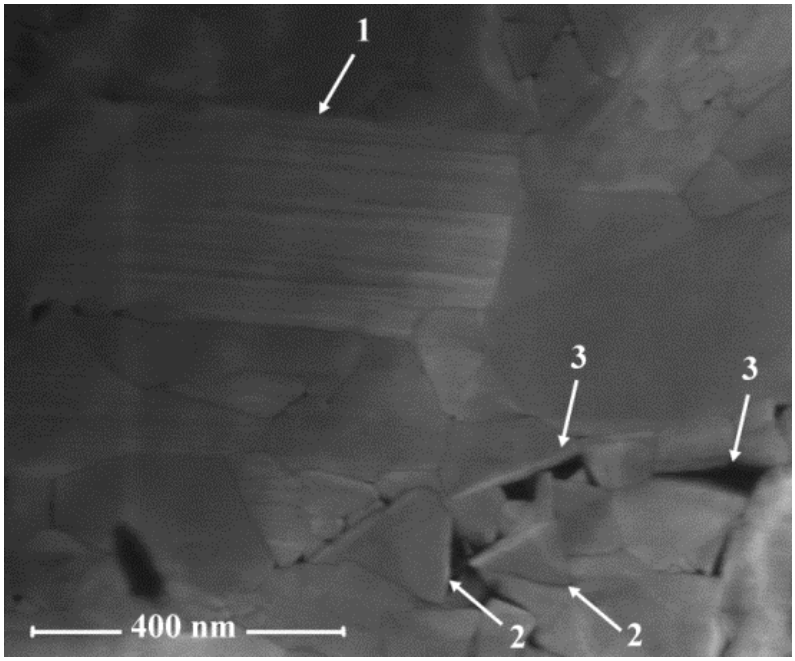

Figure 7.3. *Detailed microstructure of untreated wBN/cBN composite: (1) Micro-band sub-structure of the lamellas; (2) Polyhedral grains at the fragmentation interfaces; (3) Pores due to polyhedral faceting*

The lamellas are originally the wurtzite BN grains fragmented during cold compaction prior to HP-HT (high pressure-high temperature) processing. Smaller polyhedral grains nucleate mainly during plastic fragmentation of lamellas under HP-HT conditions and further evolve during recrystallization process. Such fragmentation takes place due to both of kink band nucleation and formation of interfaces via slip along prismatic and basal planes. Phase composition of the initial material is wurtzite BN, cubic BN, and multilayer polytypes. Confirmation to the existence of these polytypes is the micro-band sub-structure of lamellas (Figure 7.3 and 7.4) which comprises of thin wBN and cBN plates as a result of layerwise wBN → cBN transformation (Figure 7.4).

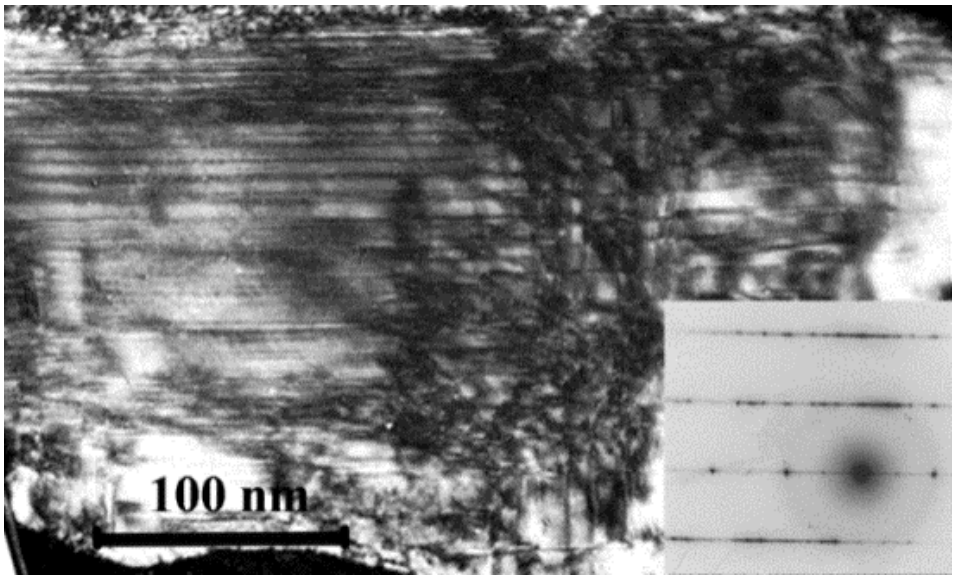

Figure 7.4. *Dark field (in 0001 wBN - 111 cBN joint reflection) TEM of micro-band sub-structure and corresponding SAED*

The existence of cBN/wBN lamella microstructure can be attributed to the observed increase in hardness. Similar phenomenon has also been reported by other researchers that a nanocomposite containing a mixture of cBN and wBN reached the same level of indentation hardness as diamond[2, 3]. Their experimental result suggested that wBN may be as hard or even harder than diamond, which came as a surprise since wBN and cBN have a similar bond length, elastic moduli, and ideal tensile and (pure) shear strength [4]. A quantum confined effect was proposed[2] to explain the observed phenomenon. Chen's group[5] performed the first-principles calculations on wBN structure undergoing biaxial shearing stresses to simulate indentation. They proved that under large compressive pressure, wBN compelled into a stronger structure through a volume-conserving bond-flipping structural phase transformation which produces a significant enhancement in its strength.

Nanotwinning has been reported a mechanism that substantial strengthen the cBN in experiment [6-8]. Hardness of nanotwinned cBN could reach 108Gpa as nanotwinned grain

thickness reduced to 3.8nm. They show that hardening of cBN is continuous with decreasing twin thickness down to the smallest sizes investigated, contrasting with the expected reverse Hall-Patch effect below a critical grain size or the twin thickness of 10-15 nm found in metals and alloys. Similar experimental observations were found in nanotwinned diamond[9] and nanotwinned copper[10, 11]. Chen's group[12] studied the nanotwinned cBN under indentation shear stresses using first-principle simulation. They revealed the twin-boundary dominated indentation strain-stiffening mechanism by bond rearrangement at the twin boundary under indentation compressive and shear strains.

The aim of this study is using atomic simulation (molecular statics) as a toolbox to analyze the strength change of cBN/wBN lamella structure and nanotwinned cBN structure as grain size (layer thickness) decreases. Hall-Patch effect is expected to contribute to the hardness increase.

7.2 Potential for cBN and wBN

The Tersoff potential is a three-body potential function which explicitly includes an angular contribution of the force. It reflects the local coordination environment of each individual atom, and allows for the formation and dissociation of covalent chemical bonds during a molecular simulation. Tersoff potential has achieved its appreciable success in treating systems containing silicon[13], carbon[14], germanium[14], gallium[15], nitrogen[15], or combination of these species. Due to the similarity in atomic structure and chemical bonding between silicon and cBN (diamond cubic lattice), Tersoff potential is a proper and the most widely used model to describe cBN structure. The form of the energy E, between two neighbouring atoms i and j, is taken to be [13]:

$$E = \frac{1}{2}\sum_i \sum_{j \neq i} V_{ij}$$

$$V_{ij} = f_c(r_{ij})[f_R(r_{ij}) + b_{ij} f_A(r_{ij})]$$

$$f_c(r) = \begin{cases} 1 & r < R - D \\ \frac{1}{2} - \frac{1}{2}\sin(\frac{\pi}{2}\frac{r-R}{D}) & R - D < r < R + D \\ 0 & r > R + D \end{cases}$$

$$f_R(r) = Ae^{-\lambda_1 r}$$

$$f_A(r) = -Be^{-\lambda_2 r}$$

$$b_{ij} = (1 + \beta^n {\zeta_{ij}}^n)^{-\frac{1}{2n}}$$

$$\zeta_{ij} = \sum_{k \neq i,j} f_c(r_{ik})\, g(\theta_{ijk})$$

$$g(\theta) = \gamma_{ijk}(1 + \frac{c^2}{d^2} - \frac{c^2}{[d^2 + (\cos\theta - \cos\theta_0)^2]}) \quad (7.1)$$

where r_{ij} is the distance between the atoms i and j, $f_A(r)$ including three-body interactions is the attractive pair potential, $f_R(r)$ is a two-body term that represent the repulsive pair potential and $f_c(r)$ is a smooth cutoff function. A, B, λ_1, λ_2 are constants determined through fitting model with experimental data.

Several kinds of Tersoff potential parameters for BN have been proposed thus far. Sekkal et al.[16] investigated the structure and the thermodynamic properties of BN using the same potential parameters for both Boron (B) and Nitrogen (N). The neglect of the differences of B-B, N-N and N-B interactions may bring some errors in this case. Albe and Moller[17] proposed a Tersoff-like interatomic potential for BN with the two-body term substituted by Morse potential (Brenner[18]). This model however loses the practicability in LAMMPS due to the fixed format of the Tersoff type (I used to try this but the structure cannot maintain

stable). Cagin's group [19, 20] developed tersoff penitential parameters for hexagonal boron nitride based nanostructures including BN nanotube and BN graphene and their results were highly consistent with first-principle and experimental investigations. Matsunaga et al.[21] fitted the Tersoff potential parameters to simulate cubic boron carbonitrides and the calculated lattice constant and bulk modulus for cBN and c-$C_{0.33}(BN)_{0.67}$ agreed well with the experimental measurements. Won Ha Moon[22] developed a new set of c-BN tersoff parameters. They inherited the potential parameters of Nitrogen from the silicon nitride simulation of de Brito Mota [23]. The B-N, B-B interactions were determined through fitting the lattice constant, cohesive energy, bulk modulus, heat of formation, and the structural stability with both theoretical and experimental data. The parameters c, d and h were taken from Albe[17]. Figure 7.5 compares the B-B, B-N and N-N interactions reported by Won Ha Moon (WHM) and Katsuyuki Matsunaga (KM). The N-N interaction that has only repulsive terms is very similar in these two studies. In contrast, B-N bonding is stronger in KM's work while B-B bonding is stronger in WHM's work.

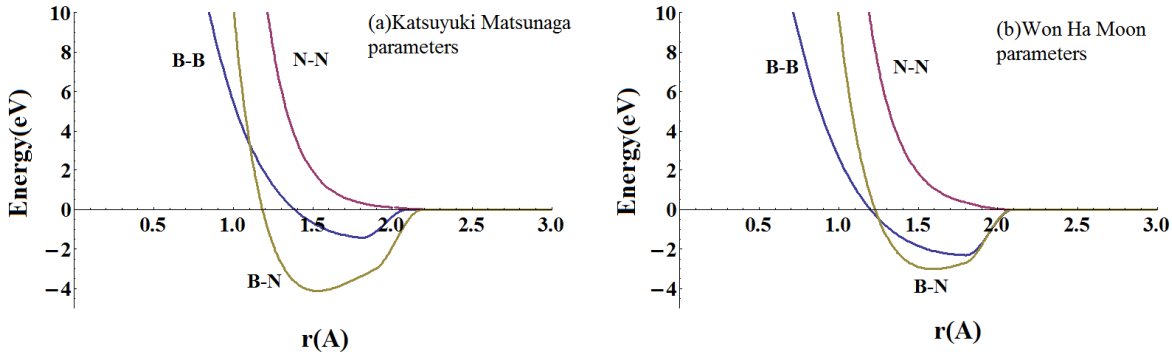

Figure 7.5. *B-B, B-N and N-N interactions of Katsuyuki Matsunaga[21] and Won Ha Moon[22]*

There are very few MD study of wurtzite BN. Marian's group[24] proposed Morse based two-body potential parameters for solid silicon nitride, boron nitride, and borosilazane,

and they investigated the structural properties of wBN. In their later publication[25], a three-body Stillinger-Weber term was added in describing the N-B-N interaction in addition to the original two-body terms. Such consideration of the three-body term improved the accuracy of w-BN simulation. The increased complexity of the potential form however makes it difficult to be implemented in LAMMPS. Stillinger-Weber potential has been successful in modeling the wurtzite structures, such as InN[26] and GaN[27, 28]. Won Ha Moon used a modified SW potential to model both c-BN and w-BN. I employed their parameters in w-BN structure but can't keep the structure stable. Tersoff potential has also been used in wurtzite AlN[29], but never been reported to be applied in wurtzite BN. It may make sense to use the same Tersoff parameters for both cBN and wBN since they have a similar bond length, elastic moduli and ideal tensile and shear strength[5].

In this study, cBN and wBN are modeled with the same Tersoff potential based on the parameters of Won Ha Moon[22].

7.3 Simulation method

cBN and wBN structures was created based on the reported lattice constant and atom arrangements. Figure 7.6 represents the crystal lattice structures of cBN and wBN (Pictures are taken from Wikipedia). Lattice constant a of cBN unit cell was measured to be 3.616 Å, and lattice constant a and c of wBN unit cell was reported to be 2.55 Å and 4.22 Å [30]. The structural relationship between cBN and w-BN is given by different stacking sequences. In cBN, both Boron and Nitrogen have the fcc structure that contains three types of planes with a ABCABC stacking sequence along the [111] direction. In wBN, both Boron and Nitrogen hold the hcp structure which contains only two types of planes with an alternating ABAB

arrangement along the [0001] direction. Thus, the(111), $(1\bar{1}0)$, and$(\bar{1}\bar{1}2)$ planes of c-BN are chosen to compare to (0001), $(\bar{1}2\bar{1}0)$, and $(10\bar{1}0)$ planes of w-BN. It is reported that the main slip plane in diamond system has been experimentally confirmed to be the (111) plane [31, 32]. Similar phenomenon has also been observed in cBN that the dislocation happens on the (111) plane [33]. Therefore, shear stress is applied in (111) plane of cBN and (0001) plane of wBN. The simulation structures are represented in Figure 7.7.

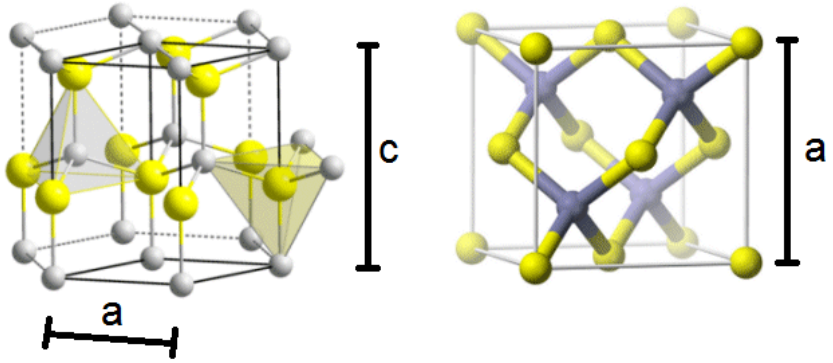

(a) (b)

Figure 7.6 *cBN and wBN cell: (a) wBN unit cell (b) cBN unit cell[34, 35]*

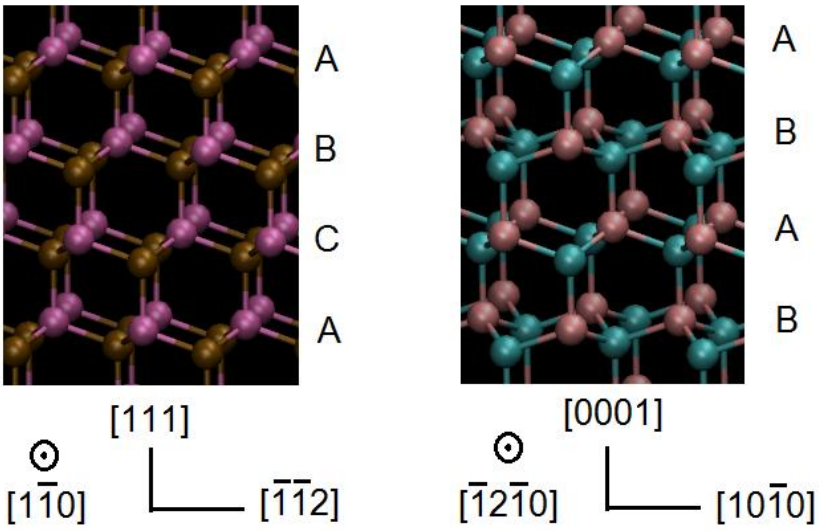

Figure 7.7. *Crystallographic stacking sequence in a rotated structure for (a) c-BN with* (111), $(1\bar{1}0)$, *and*$(\bar{1}\bar{1}2)$, *(b) for w-BN with* (0001), $(\bar{1}2\bar{1}0)$, *and* $(10\bar{1}0)$

Rectangular blocks of 20*20*5nm containing 34560 atoms in the direction shown in Figrue 7.7 are created for simulating single crystalline cBN and wBN. Nanotwinned cBN structure and cBN/wBN lamella structure of 2 layers, 4 layers and 8 layer are also generated in blocks of 20*20*5nm. The layer thicknesses are: 10nm for the 2 layer structure, 5nm for the 4 layer structure and 2.5nm for the 8 layer structure. Nonatwinned boundary and cBN/wBN lamella boundary are shown in Figure 7.8. Molecular statics simulations of pure shear and combined compression and shear are performed on these microstructures. The molecular statics is a quasi-static process in which the final relaxed configuration of the atomic structure is determined using an energy minimization technique. It has been increasingly employed as a means of simulating indentation process [36-38] because indentation can be regarded as a quasi-static process that the kinetics of individual atoms within the system are ignored. Molecular statics simulations yield a considerable improvement in the computational efficiency compared to that of MD simulations. Jeng et al. [39] compared molecular dynamics and molecular statics simulation of carbon nanotube under tension, and found that MS results are almost identical with MD results at 0.01K. Chang et al.[40] reported similar findings.

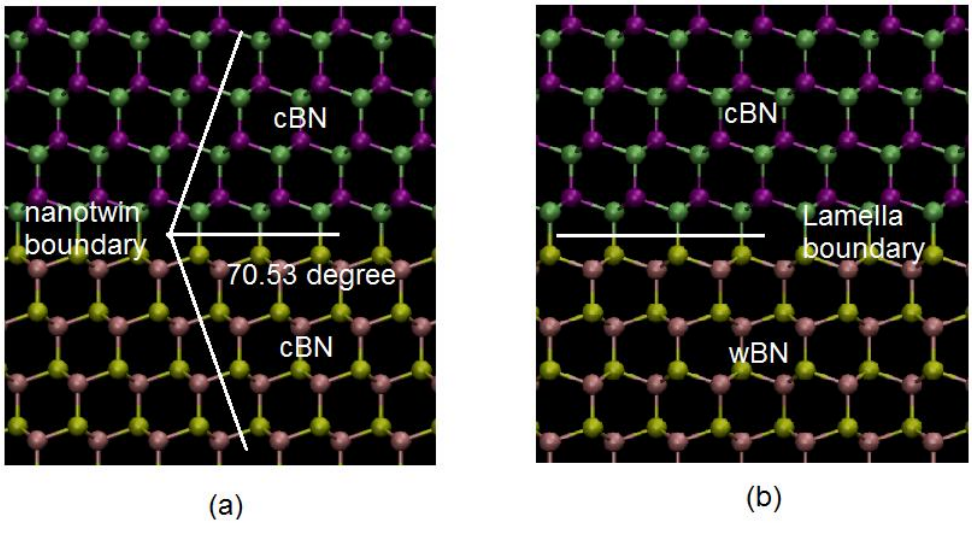

Figure 7.8. *(a) cBN nanotwinned boundary (b) for cBN/wBN lamella boundary*

In this work, we perform molecular statics calculations to determine the stress-strain relation that describes the indentation process where shear and normal compressive displacements are applied simultaneously. The ratio of normal displacement and shear displacement is equal to $tan\emptyset$, where $\emptyset = 68°$ is the centerline to face angle of a Vicker indenter. Figure 7.9(a) shows the loading condition. The top layer of atoms is forced to move a certain distance along +x and –y direction at each step, while the bottom layer of atoms is fixed to 0 displacement. The left and right layers of atoms also move a variable amount of displacement in +x and -y dimension depending on the atoms' coordinate. Periodic boundary condition is used in z direction, and shrink-wrapped boundary condition is assumed in the x and y direction. All the models are first relaxed in NVT ensemble for 10000 steps until the system reaches equilibrium.

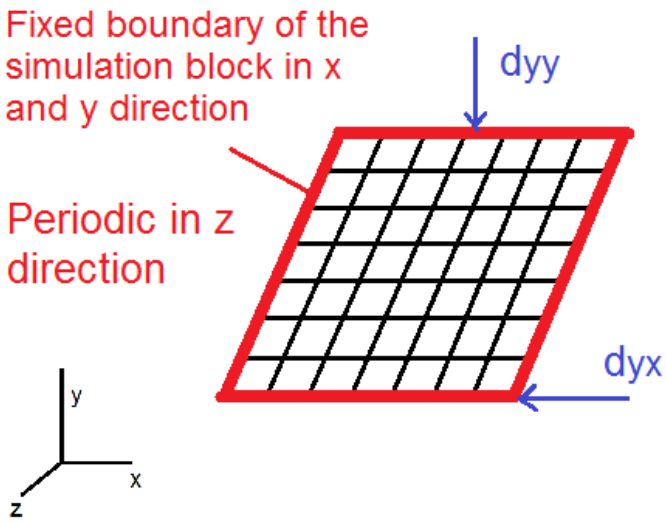

Figure 7.9. *Indentation loading*

7.4 Result and discussion

7.4.1 Combined shear and compression of single crystalline cBN and wBN in different directions

Figure 7.10 represents the stress-strain relationship for the 20*20*5 single crystalline cBN blocks under indentation loading in different directions. Elastic moduli are equal in all directions because of the isotropic nature of cBN lattice, while the plastic behaviors are different in different directions. The lowest stress response under indentation loading for cBN is found in the (111) $[11\bar{2}]$ slip systems. In (111) plane, $[\bar{1}\bar{1}2]$ is the strongest direction due to the three-layers stacking sequence ABCABC. Figure 7.11 shows the results for wBN. The stress response for wBN in the $[\bar{1}2\bar{1}0]$ direction is comparable with the $[1\bar{1}0]$ direction for cBN (cBN is a little bit stronger). The $[10\bar{1}0]$ and $[\bar{1}010]$ behave similarly since wBN structure is essentially symmetric along these two orientations. Zhang et al. published the shear stresses of cBN and wBN using ab initio DFT calculation which is accordant with the current work. The stress-strain curve for indentation loading in y direction for wBN is also plotted in Figure 7.11. Due to the orthotropic behavior of hcp lattice, modulus in y direction is different from those in (0001) plane. It is important to note that the simulation is limited only in investigating the indentation shearing on the easiest slip planes which are (111) for cBN and (0001) for wBN.

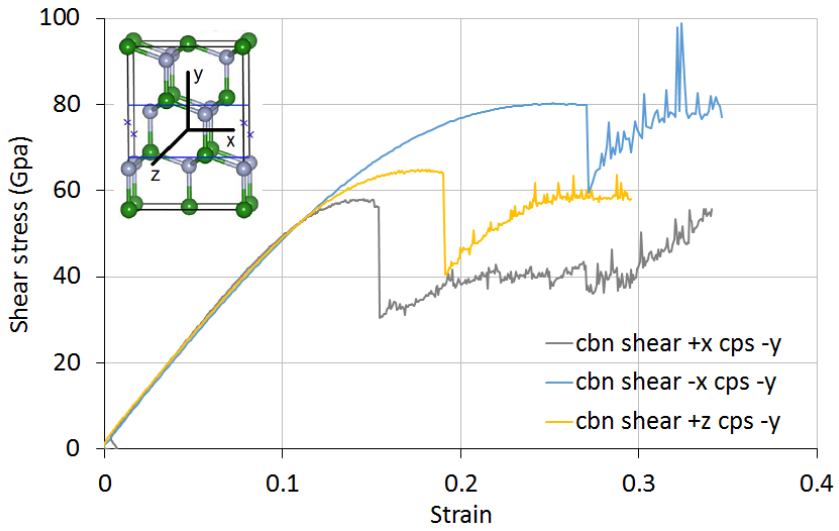

Figure 7.10. *Stress-strain relationships for single crystalline cBN under indentation loading in different directions*

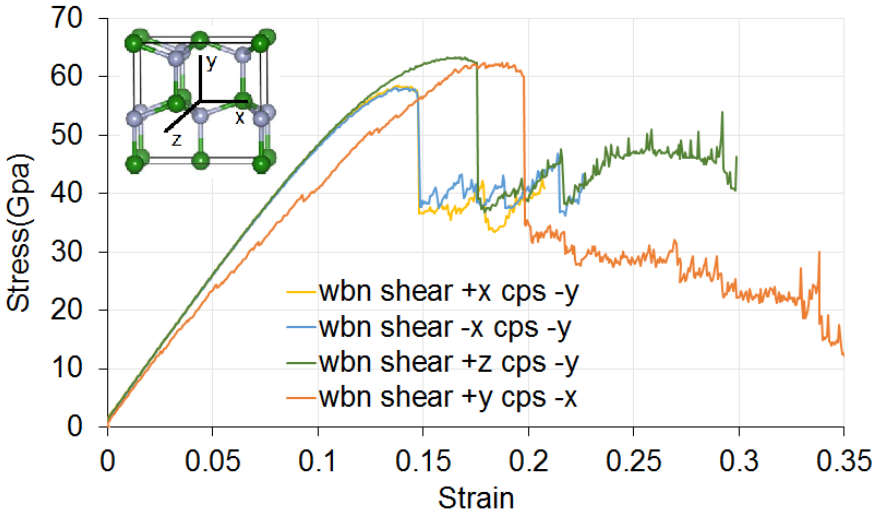

Figure 7.11. *Stress-strain relationships for single crystalline wBN under indentation loading in different directions*

The size effect of cBN and wBN are studied through applying indentation loading to structures with different thicknesses. Figure 7.12 plots the stress-strain relationships for a single crystalline cBN with thicknesses of 5nm, 10nm, and 20nm. A hardening effect can be observed as thickness decreases. Figure 7.13 shows the snapshot of the three models coloring coordination number of each atom at strain = 0.35. It can be observed that dislocations mainly

happens in (110) and (111) planes for cBN. The dislocations on (110) plane is restricted by the top and bottom boundary, and dislocations on (111) plane are impeded by left and right boundary. As structure thickness decreases, more dislocations are developed on (110) plane and are obstructed from moving by the top and bottom boundary. This may be the mechanism underlying the strain- hardening of the material. Figure 7.14 and 7.15 show the same loading condition on wBN structures. Strain hardening phenomena are not observed in wBN since the dislocations in wBN only occur in (0001) plane. Therefore, decreasing the thickness in [0001] direction barely disturbs the movement of dislocations.

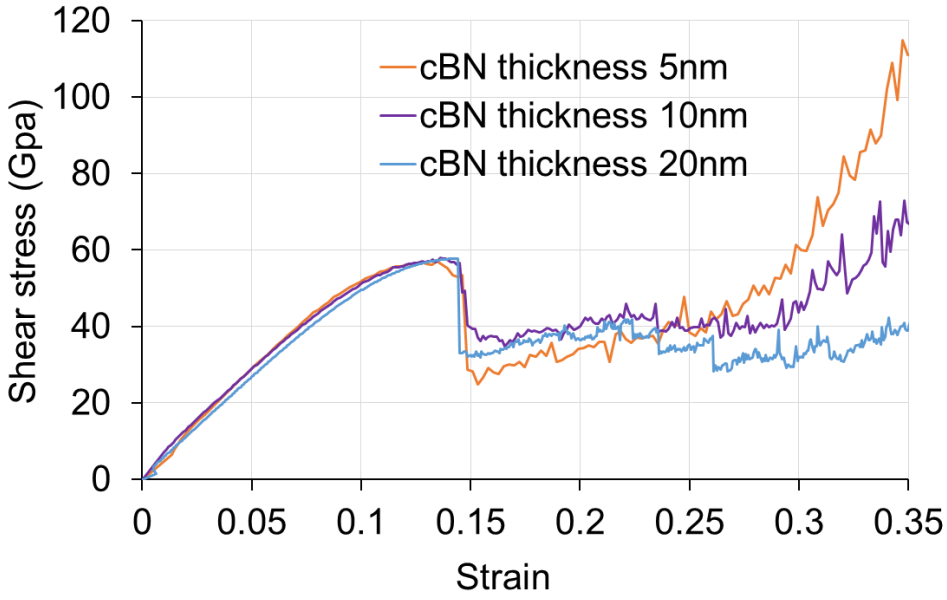

Figure 7.12. *Stress-strain relationships for single crystalline cBN with different thickness under indentation loading*

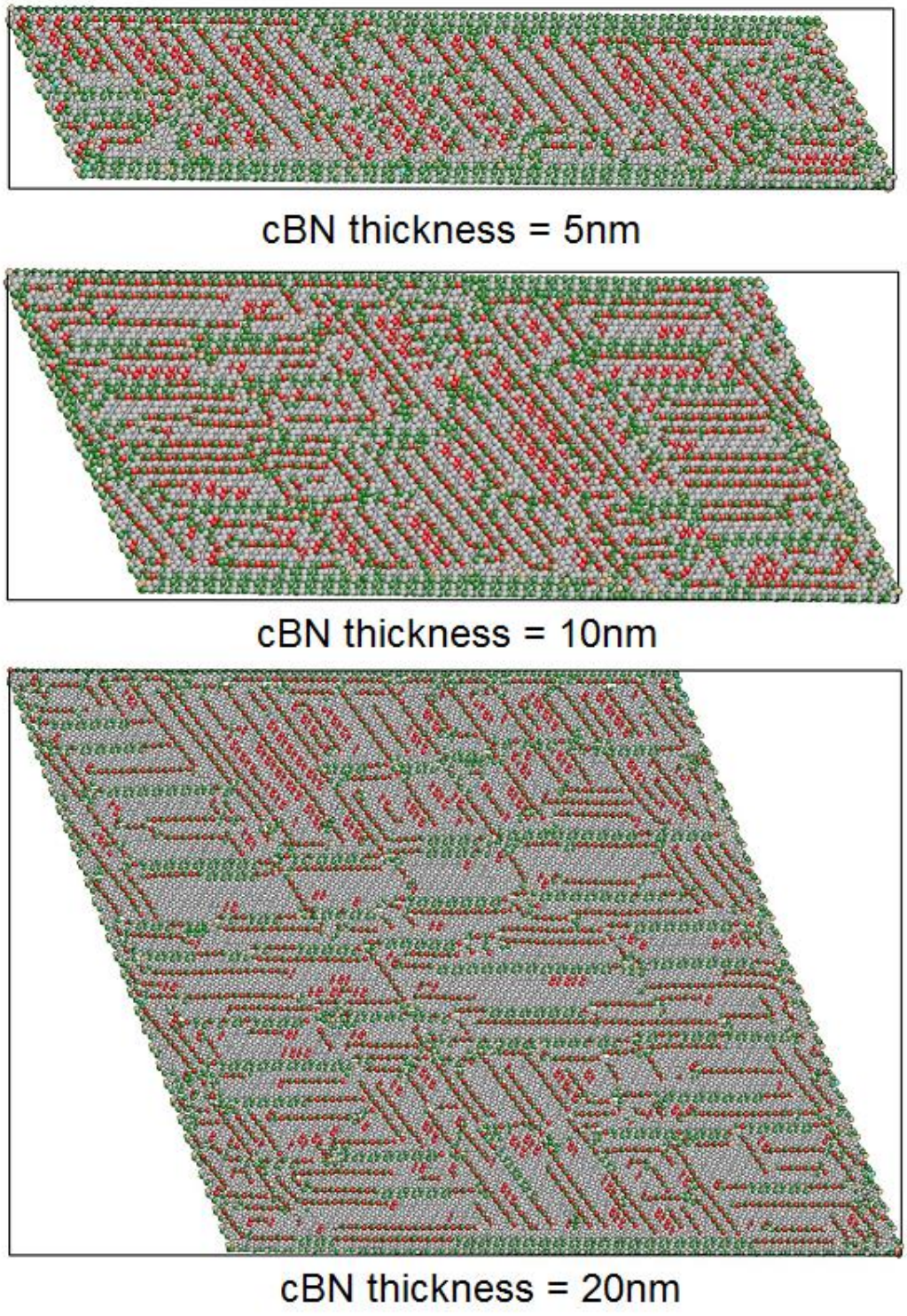

Figure 7.13. *Dislocations of cBN structure with different thicknesses at strain = 0.35*

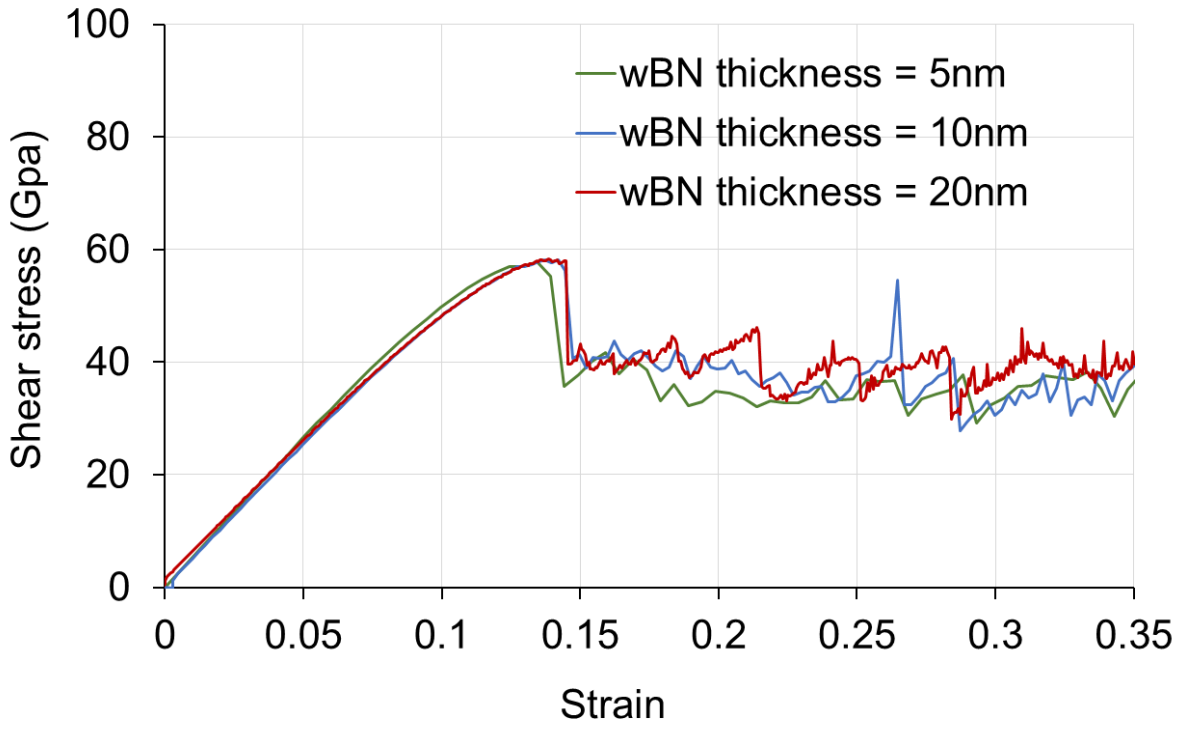

Figure 7.14. *Stress-strain relationships for single crystalline wBN with different thickness under indentation loading*

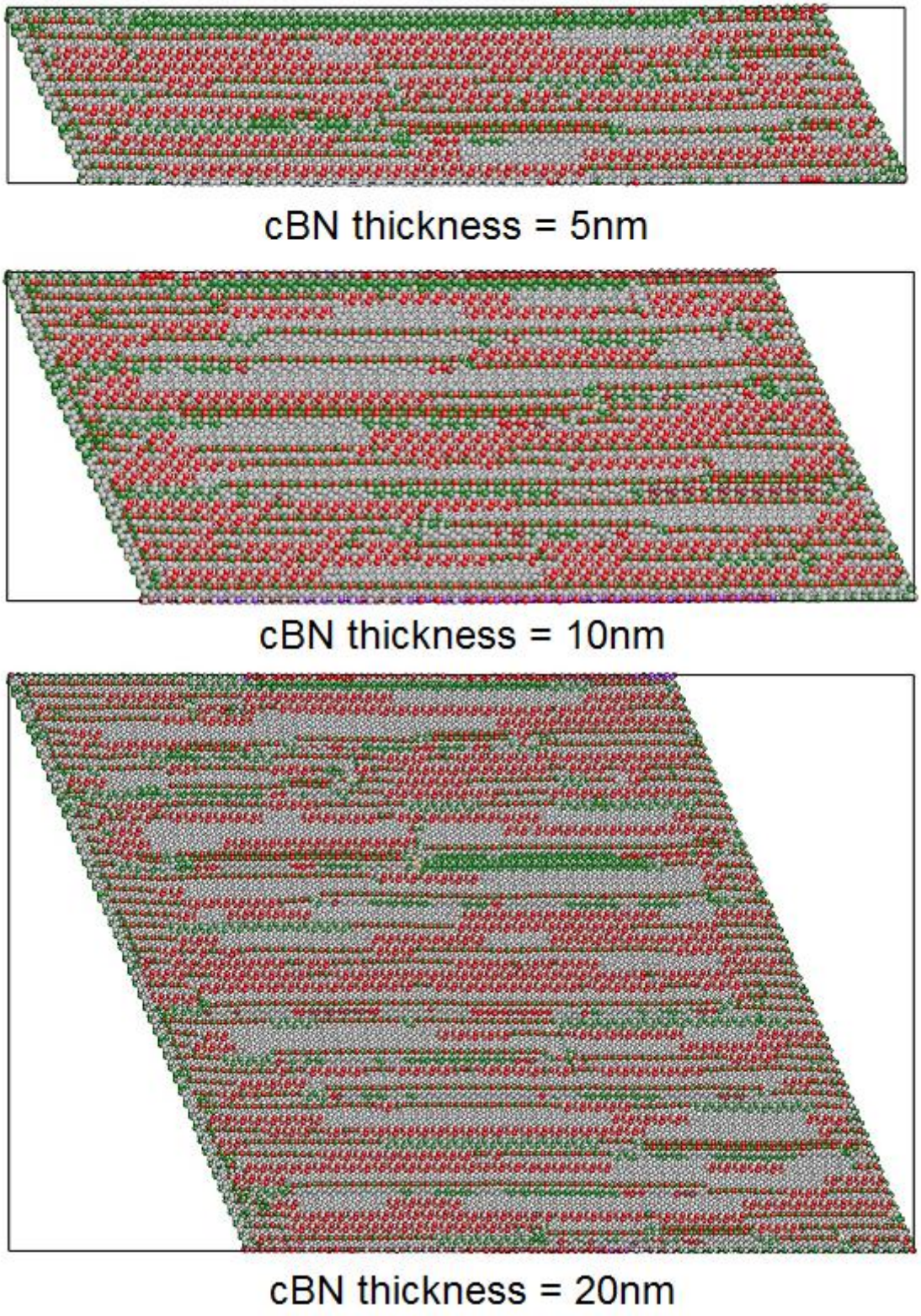

Figure 7.15. *Dislocations of wBN structure with different thicknesses at strain = 0.35*

7.4.2 Indentation loading on Nanotwinned cBN

Indentation loading is applied on nanotwinned cBN with 2 layers, 4 layers and 8 layers. The stress responses are plotted in Figure 7.16. Results show no significant differences in the three models. The hardening effect can be again observed in all of them.

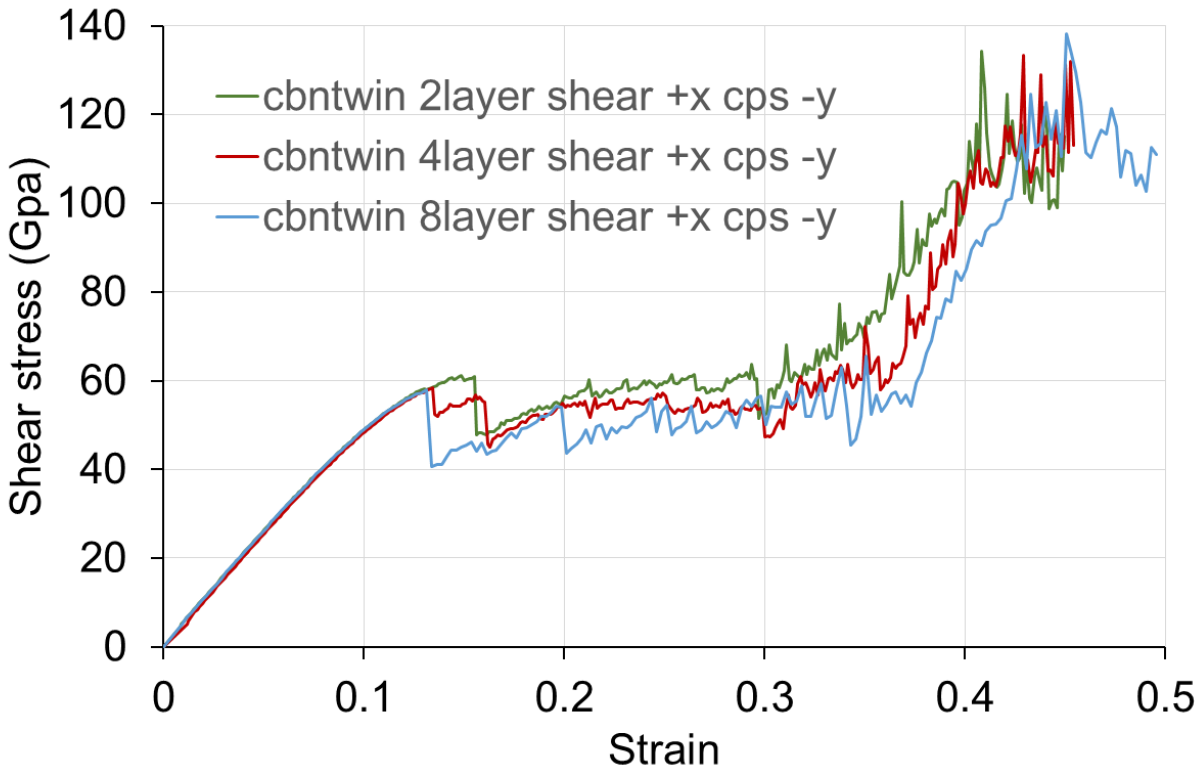

Figure 7.16. *Stress-strain relation for nanotwinned cBN with 2 layers, 4 layers and 8 layers*

Figure 7.17 shows the stress-strain relationship of nanotwinned 2-layer cBN with upper half and lower half calculated separately. The upper half of cBN performs like the weakest crystalline structure in $[11\bar{2}]$ direction, while the lower half follows the strongest behavior in $[\bar{1}\bar{1}2]$ direction. Snapshots of the model are also included in Figure 7.17. Dislocations are first observed in the nanotwinned boundary, and then grow in the upper half where the structure is weaker and easy to slip. Dislocations start to show in the lower half as strain reaches 0.28,

where hardening start to show in the upper half. The overall behavior of the 2-layer structure is the average of the two layers. Similar responses are also observed in the 4-layer and 8-layer structures.

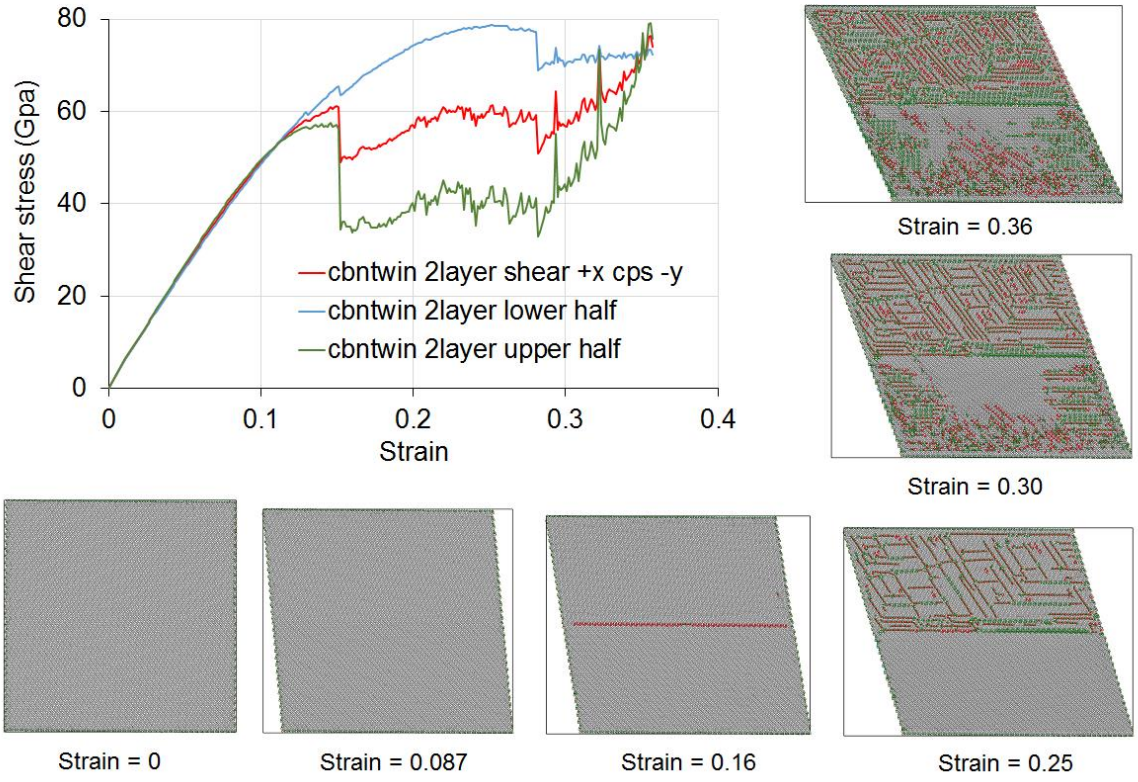

Figure 7.17. *Stress-strain relationship of nonatwinned 2-layer cBN*

7.4.3 Indentation loading on cBN/wBN lamella

Unlike nanotwinned cBN (symmetric), the cBN/wBN lamella behaves differently in different directions due to the anisotropic nature of the structure of cBN. Figure 7.18 shows the indentation shearing of cBN/wBN lamella in -x with 2 layers, 4 layers, and 8 layers. The responses can be regarded as identical for the three models, and no hardening effects are observed.

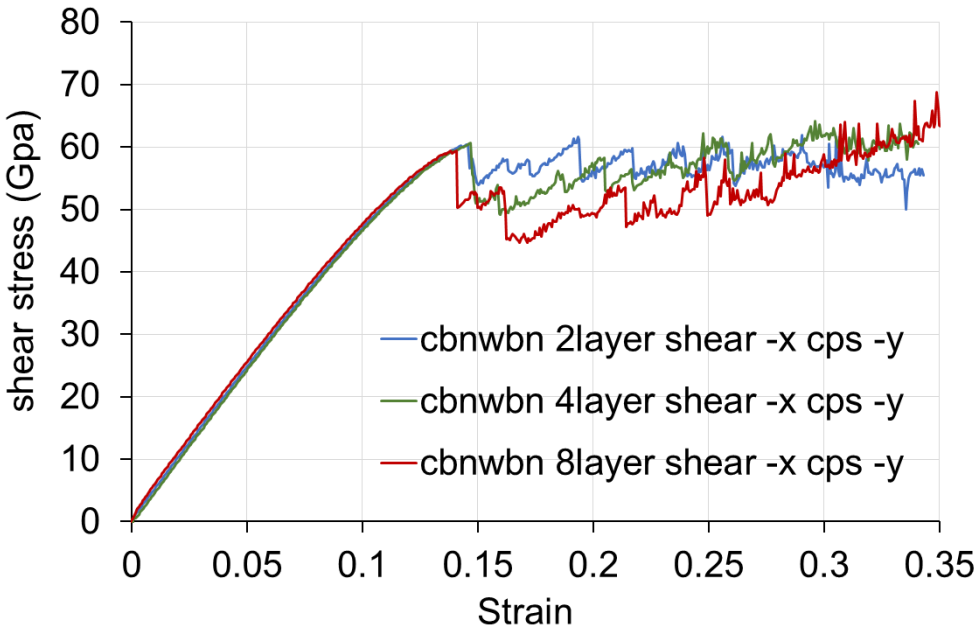

Figure 7.18. *Stress-strain relation for cBN/wBN lamella with 2 layers, 4 layers and 8 layers shearing in –x direction*

Figure 7.19 and 7.20 show detailed stress-strain relations when indentation shearing are performed in +x and –x direction. cBN layer and wBN layer for each model are calculated separately. In the case of shearing in +x direction where cBN is in the weakest direction, dislocations appear in both cBN and wBN layers. Similar phenomena can be observed in the single-crystalline studies: two types of dislocation on both (110) and (111) plane are found in cBN, while wBN displays only one type of dislocation on (0001) plane. Therefore, cBN layer is hardened due to dislocations in (110) plane while wBN layer shows no hardening effect. In the indentation shearing in –x direction, cBN is loaded in the strongest direction abd dislocations are mainly observed in wBN layer. The average strength of the lamella structure of the indentation loading in –x direction is higher than the strength of +x (before strain hardening).

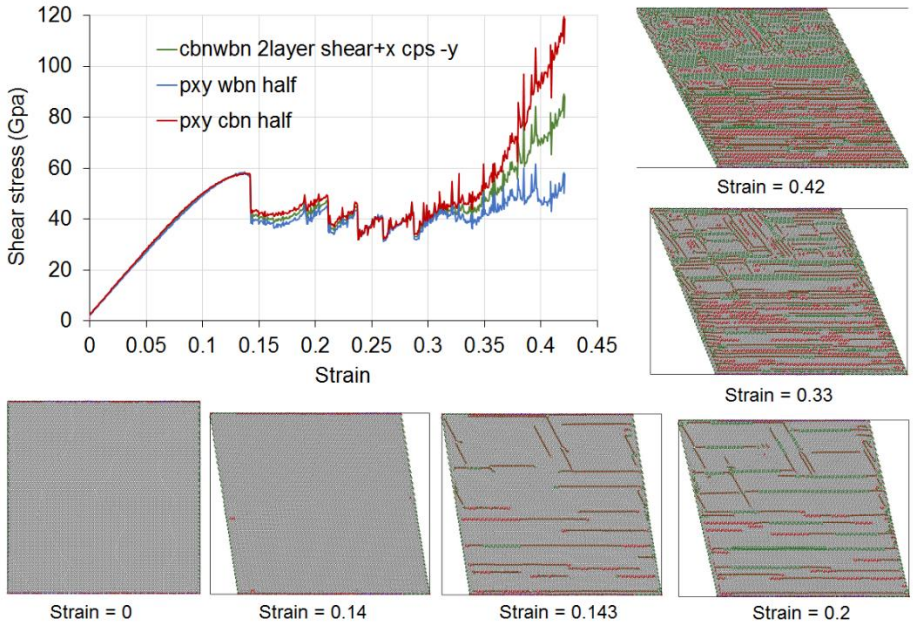

Figure 7.19. *Stress-strain relationship of 2-layer cBN/wBN lamella under indentation shearing in +x direction*

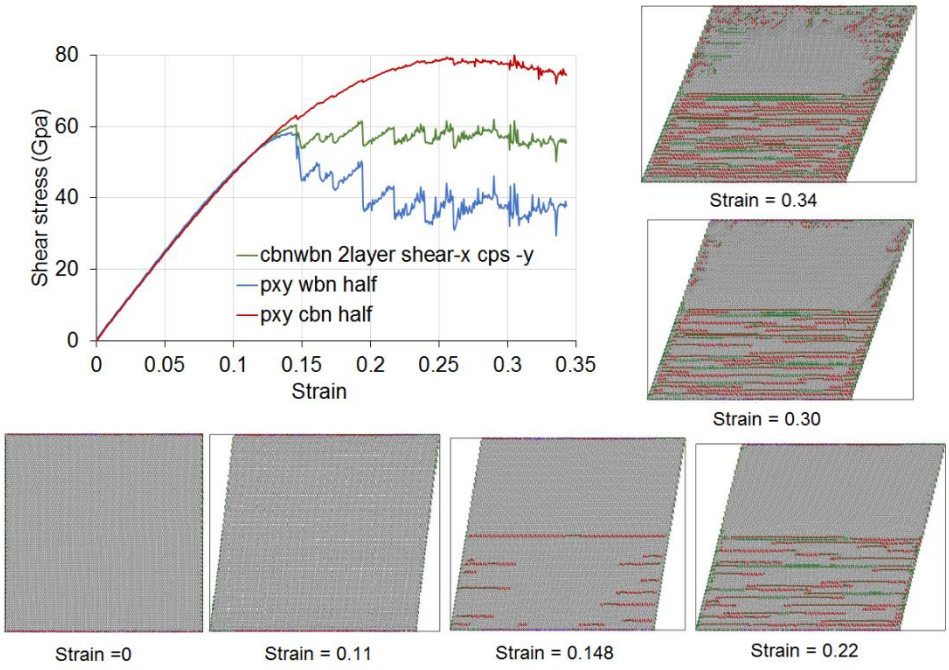

Figure 7.20. *Stress-strain relationship of 2-layer cBN/wBN lamella under indentation shearing in -x direction*

7.4.4 A trial of dynamic simulation of nanotwinned cBN

Molecular dynamics simulations of single-crystalline cBN, 2-layer and 4-layer nanotwinned cBN are performed with the NVT ensemble. A shear velocity of 2.5m/s and compression velocity of 1m/s are added to the top layer of atoms. Temperature is maintained at 300K. Figure 7.21 shows the stress-strain curve where the 2-layer nanotwinned cBN exhibits the highest strength. Shear stress and failure strain are much lower than the molecular static results. Jeng et al. [39] and Chang et al.[40] compared tension tests of carbon or metal microstructures under molecular statics(MS) and molecular dynamics (MD) simulation at 0.01K and 300K and found that the strength of MD simulation at 300K is almost half of the strength of MS and MD at 0.01K, respectively, and failure strains are much smaller. Our results are consistent with their findings.

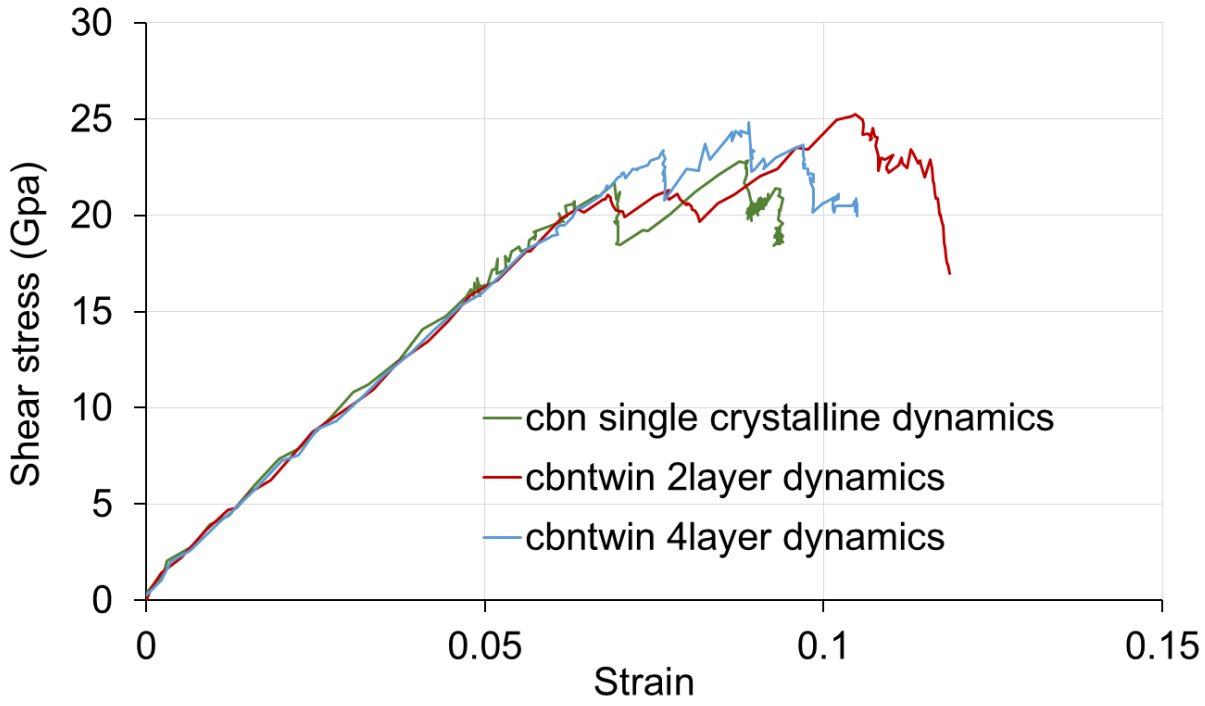

Figure 7.21. *Stress-strain relation of single-crystalline cBN, 2-layer and 4-layer nanotwinned cBN of molecular dynamics simulation*

Figure 7.22 shows the snapshots of dislocation development under dynamic simulation. Dislocations are first observed close to the moving top layer in (111) plane, and then grow into the (110) plane and move along that direction. In the 2-layer and 4 layer model, dislocations on (110) plane are blocked at the twin boundary and are redirected to propagate in the twin boundary. Jin, Z. H[41] reported a similar phenomenon in simulating a screw dislocation movement in Al with a coherent twin boundary.

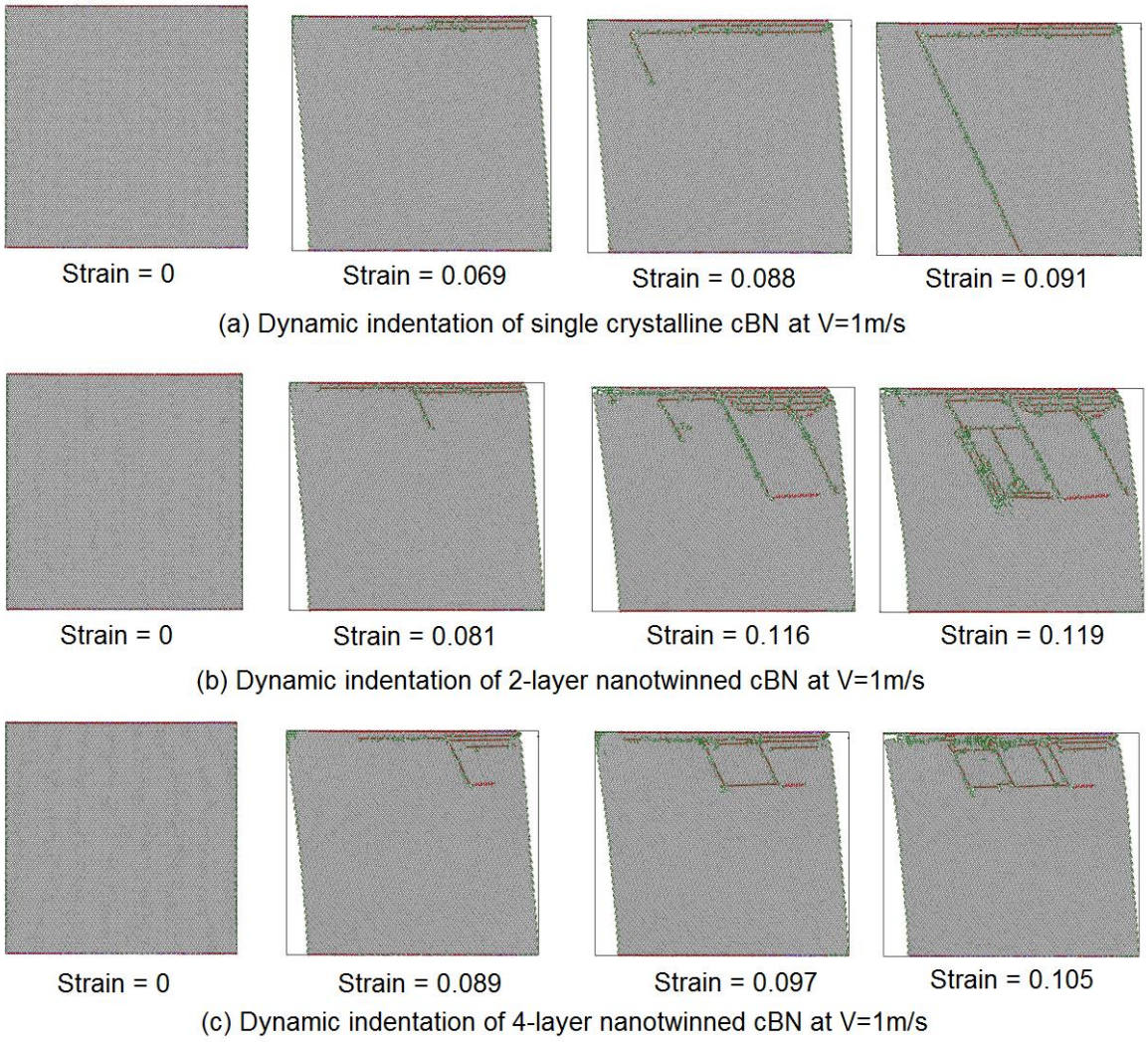

Figure 7.22. *Dislocations of cBN structure with different thicknesses at strain = 0.3*

The shear strength is expected to increase as the layer thickness of nanotwinned cBN and cBN/wBN lamella decreases. Possible reasons that may lead to the unexpected results are: (1) Inappropriate potential. Tersoff potential parameters provided in literature may be not accurate in simulating shearing of cBN. In addition, Tersoff type potential may be not suitable to precisely describe the wBN structure. New potential parameters need to be developed and be fitted to accommodate the mechanical properties of cBN and wBN. (2) Size effect. Molecular statics(MS) is highly dependent on the simulation size of the model [40]. Molecular Dynamics (MD) has no such a limitation. Chang et al.[40] stated that molecular statics, as an energy minimization numerical scheme, is quite insensitive to the instability of atomic structure especially without thermal fluctuation and might not be a suitable tool for studying the behavior of nanomaterials beyond the elastic limit.

7.5 References

[1] A. A. Melaibari, Z. Wu, P. Shrotriya, P. Molian, V. Bushlya, J. Zhou, *et al.*, "Extreme Hardness Achievements in Binderless Cubic Boron Nitride Tools," presented at the NAMRC 41/MSEC 2013, Madison, Wisconsin, 2013.

[2] N. Dubrovinskaia, V. L. Solozhenko, N. Miyajima, V. Dmitriev, O. O. Kurakevych, and L. Dubrovinsky, "Superhard nanocomposite of dense polymorphs of boron nitride: Noncarbon material has reached diamond hardness," *Applied Physics Letters,* vol. 90, Mar 5 2007.

[3] V. L. Solozhenko, O. O. Kurakevych, and Y. Le Godec, "Creation of Nanostuctures by Extreme Conditions: High-Pressure Synthesis of Ultrahard Nanocrystalline Cubic Boron Nitride," *Advanced Materials,* vol. 24, pp. 1540-1544, Mar 22 2012.

[4] R. F. Zhang, S. Veprek, and A. S. Argon, "Anisotropic ideal strengths and chemical bonding of wurtzite BN in comparison to zincblende BN," *Physical Review B*, vol. 77, May 2008.

[5] Z. C. Pan, H. Sun, Y. Zhang, and C. F. Chen, "Harder than Diamond: Superior Indentation Strength of Wurtzite BN and Lonsdaleite," *Physical Review Letters*, vol. 102, Feb 6 2009.

[6] Y. J. Tian, B. Xu, D. L. Yu, Y. M. Ma, Y. B. Wang, Y. B. Jiang, *et al.*, "Ultrahard nanotwinned cubic boron nitride," *Nature*, vol. 493, pp. 385-388, Jan 17 2013.

[7] N. Dubrovinskaia and L. Dubrovinsky, "Controversy about ultrahard nanotwinned cBN," *Nature*, vol. 502, pp. E1-E2, Oct 24 2013.

[8] Y. J. Tian, B. Xu, D. L. Yu, Y. M. Ma, Y. B. Wang, Y. B. Jiang, *et al.*, "Controversy about ultrahard nanotwinned cBN reply," *Nature*, vol. 502, pp. E2-E3, Oct 24 2013.

[9] Q. Huang, D. L. Yu, B. Xu, W. T. Hu, Y. M. Ma, Y. B. Wang, *et al.*, "Nanotwinned diamond with unprecedented hardness and stability," *Nature*, vol. 510, pp. 250-+, Jun 12 2014.

[10] L. Lu, X. Chen, X. Huang, and K. Lu, "Revealing the Maximum Strength in Nanotwinned Copper," *Science*, vol. 323, pp. 607-610, Jan 30 2009.

[11] L. Lu, Y. F. Shen, X. H. Chen, L. H. Qian, and K. Lu, "Ultrahigh strength and high electrical conductivity in copper," *Science*, vol. 304, pp. 422-426, Apr 16 2004.

[12] B. Li, H. Sun, and C. F. Chen, "Large indentation strain stiffening in nanotwinned cubic boron nitride," *Nature Communications*, vol. 5, Sep 2014.

[13] J. Tersoff, "New Empirical-Approach for the Structure and Energy of Covalent Systems," *Physical Review B*, vol. 37, pp. 6991-7000, Apr 15 1988.

[14] J. Tersoff, "Modeling Solid-State Chemistry - Interatomic Potentials for Multicomponent Systems," *Physical Review B*, vol. 39, pp. 5566-5568, Mar 15 1989.

[15] J. Nord, K. Albe, P. Erhart, and K. Nordlund, "Modelling of compound semiconductors: analytical bond-order potential for gallium, nitrogen and gallium nitride," *Journal of Physics-Condensed Matter*, vol. 15, pp. 5649-5662, Aug 20 2003.

[16] W. Sekkal, B. Bouhafs, H. Aourag, and M. Certier, "Molecular-dynamics simulation of structural and thermodynamic properties of boron nitride," *Journal of Physics-Condensed Matter*, vol. 10, pp. 4975-4984, Jun 15 1998.

[17] K. Albe and W. Moller, "Modelling of boron nitride: Atomic scale simulations on thin film growth," *Computational Materials Science*, vol. 10, pp. 111-115, Feb 1998.

[18] D. W. Brenner, "Empirical Potential for Hydrocarbons for Use in Simulating the Chemical Vapor-Deposition of Diamond Films," *Physical Review B*, vol. 42, pp. 9458-9471, Nov 15 1990.

[19] C. Sevik, A. Kinaci, J. B. Haskins, and T. Cagin, "Characterization of thermal transport in low-dimensional boron nitride nanostructures," *Physical Review B*, vol. 84, Aug 22 2011.

[20] C. Sevik, A. Kinaci, J. B. Haskins, and T. Cagin, "Influence of disorder on thermal transport properties of boron nitride nanostructures," *Physical Review B*, vol. 86, Aug 1 2012.

[21] K. Matsunaga, C. Fisher, and H. Matsubara, "Tersoff potential parameters for simulating cubic boron carbonitrides," *Japanese Journal of Applied Physics*, vol. 39, 2000.

[22] W. H. Moon, M. S. Son, and H. J. Hwang, "Molecular-dynamics simulation of structural properties of cubic boron nitride," *Physica B: Condensed Matter,* vol. 336, pp. 329-334, 2003.

[23] F. de Brito Mota, J. F. Justo, and A. Fazzio, "Structural properties of amorphous silicon nitride," *Physical Review B,* vol. 58, pp. 8323-8328, Oct 1 1998.

[24] C. M. Marian, M. Gastreich, and J. D. Gale, "Empirical two-body potential for solid silicon nitride, boron nitride, and borosilazane modifications," *Physical Review B,* vol. 62, pp. 3117-3124, Aug 1 2000.

[25] M. Gastreich, J. D. Gale, and C. M. Marian, "Charged-particle potential for boron nitrides, silicon nitrides, and borosilazane ceramics: Derivation of parameters and probing of capabilities," *Physical Review B,* vol. 68, Sep 1 2003.

[26] H. P. Lei, J. Chen, S. Petit, R. Ruterana, X. Y. Jiang, and G. Nouet, "Stillinger-Weber parameters for In and N atoms," *Superlattices and Microstructures,* vol. 40, pp. 464-469, Oct-Dec 2006.

[27] N. Aichoune, V. Potin, P. Ruterana, A. Hairie, G. Nouet, and E. Paumier, "An empirical potential for the calculation of the atomic structure of extended defects in wurtzite GaN," *Computational Materials Science,* vol. 17, pp. 380-383, Jun 2000.

[28] J. Kioseoglou, P. Komninou, G. P. Dimitrakopulos, T. Kehagias, H. M. Polatoglou, G. Nouet, *et al.*, "Microstructure of planar defects and their interactions in wurtzite GaN films," *Solid-State Electronics,* vol. 47, pp. 553-557, Mar 2003.

[29] M. Tungare, Y. F. Shi, N. Tripathi, P. Suvarna, and F. Shahedipour-Sandvik, "A Tersoff-based interatomic potential for wurtzite AlN," *Physica Status Solidi a-Applications and Materials Science,* vol. 208, pp. 1569-1572, Jul 2011.

[30] A. Nagakubo, H. Ogi, H. Sumiya, K. Kusakabe, and M. Hirao, "Elastic constants of cubic and wurtzite boron nitrides," *Applied Physics Letters,* vol. 102, Jun 17 2013.

[31] P. Humble and R. H. J. Hannink, "Plastic-Deformation of Diamond at Room-Temperature," *Nature,* vol. 273, pp. 37-39, 1978.

[32] A. T. Blumenau, R. Jones, T. Frauenheim, B. Willems, O. I. Lebedev, G. Van Tendeloo, *et al.*, "Dislocations in diamond: Dissociation into partials and their glide motion," *Physical Review B,* vol. 68, Jul 1 2003.

[33] L. C. Nistor, G. Van Tendeloo, and G. Dinca, "HRTEM studies of dislocations in cubic BN," *Physica Status Solidi a-Applied Research,* vol. 201, pp. 2578-2582, Sep 2004.

[34] *https://en.wikipedia.org/wiki/Wurtzite_crystal_structure*.

[35] "https://en.wikipedia.org/wiki/Cubic_crystal_system."

[36] Y. R. Jeng and C. M. Tan, "Theoretical study of dislocation emission around a nanoindentation using a static atomistic model," *Physical Review B,* vol. 69, Mar 2004.

[37] F. Sansoz and V. Dupont, "Atomic mechanism of shear localization during indentation of a nanostructured metal," *Materials Science & Engineering C-Biomimetic and Supramolecular Systems,* vol. 27, pp. 1509-1513, Sep 2007.

[38] Y. R. Jeng and C. M. Tan, "Investigation into the nanoindentation size effect using static atomistic simulations," *Applied Physics Letters,* vol. 89, Dec 18 2006.

[39] Y. R. Jeng, P. C. Tsai, G. Z. Huang, and I. L. Chang, "An Investigation into the Mechanical Behavior of Single-Walled Carbon Nanotubes under Uniaxial Tension

Using Molecular Statics and Molecular Dynamics Simulations," *Cmc-Computers Materials & Continua,* vol. 11, pp. 109-125, Jun 2009.

[40] I. L. Chang and Y. C. Chen, "Is the molecular statics method suitable for the study of nanomaterials? A study case of nanowires," *Nanotechnology,* vol. 18, Aug 8 2007.

[41] Z. H. Jin, P. Gumbsch, E. Ma, K. Albe, K. Lu, H. Hahn, *et al.*, "The interaction mechanism of screw dislocations with coherent twin boundaries in different face-centred cubic metals," *Scripta Materialia,* vol. 54, pp. 1163-1168, Mar 2006.

CHAPTER VIII

CONCLUSIONS AND FUTURE WORKS

8.1 Conclusions

This project involved completion of number of tasks related to hybrid laser/waterjet machining of superhard tool materials including 1.6mm solid PCBN, 1.6mm carbide supported PCBN and 1.6mm carbide supported PCD. Specifics of the work are:

1. Created processing map (merits for material selection) to rank materials in two fracture mechanisms groups: thermal shock induced fracture and transformation induced fracture.
2. Achieved high-quality cutting of PCBN and PCD specimens at a high speed that is more than 10 times faster over the existing machining techniques.
3. Identified the material removal mechanisms for the high thermal conductivity PCBN and PCD as controlled fracture separation due to phase transformation induced stresses.
4. Compared the effects of different assist fluid media on cutting PCBN and determined waterjet to be the best one.
5. Developed FEA models for prediction of temperature and stress fields and related laser machining parameters to the fracture characteristics of the material.

The driving force of fracture can be categorized into two groups: thermal shock induced fracture and phase transformation induced fracture. Laser heating and waterjet quenching induce a precipitous temperature gradient in the low thermal conductivity materials (Alumina, zirconia, glass) and subsequently, thermal stresses are large enough to drive fracture propagation and achieve material separation. For materials with high thermal conductivity (AlN, PCBN, PCD), the heat is dissipated rapidly through conduction and hence the thermal

stresses are negligible and insufficient to propagate the crack. However, material phase transformation during machining often expands the initial volume and leads to the formation of residual tensile stresses within the sample that promotes the crack propagation. Based on the two mechanisms, the material merit indices governing thermal shock induced fracture and transformation induced fracture can be derived for material selection.

In the LWJ cutting of a 1.6mm solid PCBN material, experiments are conducted to study the effect of processing parameters on the fracture behaviors. Three different fracture behavior were observed in this experiment and the threshold line energy for through cutting was identified as 11.8kJ/m. Raman spectroscopy results indicated that laser heated PCBN undergoes chemical phase transformation and material separation took place due to the stress induced by volume expansion of the transformed zone. Another set of experiments was conducted on a 4.8mm solid PCBN specimen to obtain the size of phase transformed zone as well as associated expansion strain after laser heating. Measurement of transformation strain and dimensions of transformation region reveals a linear relationship between cutting line energy and transformation depth. The transformation strain was found to be 0.013 through this method. Transformation stress with the obtained expansion strain and transformation volume was computed in FEM model. Energy release rate for channeling cracks was calculated and compared with experimental result. Good agreement between the analytical result and experimental observation demonstrated the feasibility of proposed mechanism for material separation through controlled crack propagation.

A new method of using multi-passes defocused beam after the scribing of single-pass focused beam was performed on the double-layer sample that successfully achieved specimen separation. The function of the defocused beam was studied though duplicate the cutting effect

of 1, 2, 4, and 8 passes and numerical analysis similar with the solid PCBN cutting was performed. Transformation depth was determined from SEM image of cut interface to be 200 μm for single-pass cutting and 400 μm for multi-passes defocused cutting. Surface profile measurement determined the best fitting expansion strain to be 0.08 in this sample. Energy release rates of crack propagation were calculated and the degradation of fracture toughness of WC for 20% due to repeated thermal shock was introduced to explain the through-cut result. Initiation of spalling crack was also studied in this specimen. Results indicate that a wider and shallower transformation zone will be benefit to reduce the spalling cracks.

The effect of assist media including Argon, Nitrogen and water in LWJ cutting was investigated and compared. Nitrogen and Argon induced oversized amount of phase transitions that did not offer controlled fracture mechanism and produced low surface roughness that do not make these assist gases suitable for the controlled crack separation. Water is an excellent candidate in producing threshold amount of phase transition with very thin layer as well as controlled cracking. Optimization of LWJ process is in order to further improve the process.

LWJ machining has also been applied to cut carbide supported PCD blanks and similar analytical process was performed to determine expansion strain and transformation zone of PCD material. It is found that transformation zone depth increases linearly with laser line energy. Graphitization induced volumetric changes could be modeled using a semi-elliptical zone undergoing uniform volumetric expansion strain of 1.7%. The close agreement between experimental and modeling data for both PCBN and PCD suggests that the expansion model is capable to explain controlled fracture propagation associated with material phase transformation.

8.2 Future works

Modeling of 2D contour cutting

The 2D contour cutting was successfully performed on PCBN specimen with two different angles of 120 and 135 degrees. The numerical analysis need to be conducted to identify the processing parameters required for contour cutting of PCBN. Other inserts forms such as a round shape may be also produced through LWJ cutting. Modeling of the round shape cutting is one of the future scopes of work.

Molecular simulation of PCBN

A clear conclusion cannot be drawn from the simulation in Chapter 7 and further studies need to be conducted. Several directions can be pursued to improve the simulation feasibility. One possibility would be to investigate periodic boundary condition in all of x, y and z axis in the static simulation model. The current model utilized fixed boundary in x and y direction while periodic boundary in z direction. It would be preferable to use all periodic boundaries to simulate a macro-scale behavior. It would also be very valuable to perform a molecular dynamics simulation of the indentation shearing, which is closer to the real physics due to the inclusion of thermal fluctuation. An initial trial was touched upon in Chapter 7 to simulate nanotwinned PCBN, and would certainly deserve further investigation. Another simulation that may worth examining is the model size effect. It has been reported that the movement of atoms in static simulation may not stable as in dynamic simulation and result is highly affected by the size of microstructures. Nanotwinned wBN is another interesting molecular structure that may contribute to the hardness improvement. Thickness of the nanotwinned layer may be a key factor that affects hardness as revealed in the nanotwinned cBN.